Dynamics of Enceladus' Icy Plumes

Investigating the Physics of the Plumes using DSMC

AE5822: Master's Thesis

Deepanshu Kamlesh Punjabi

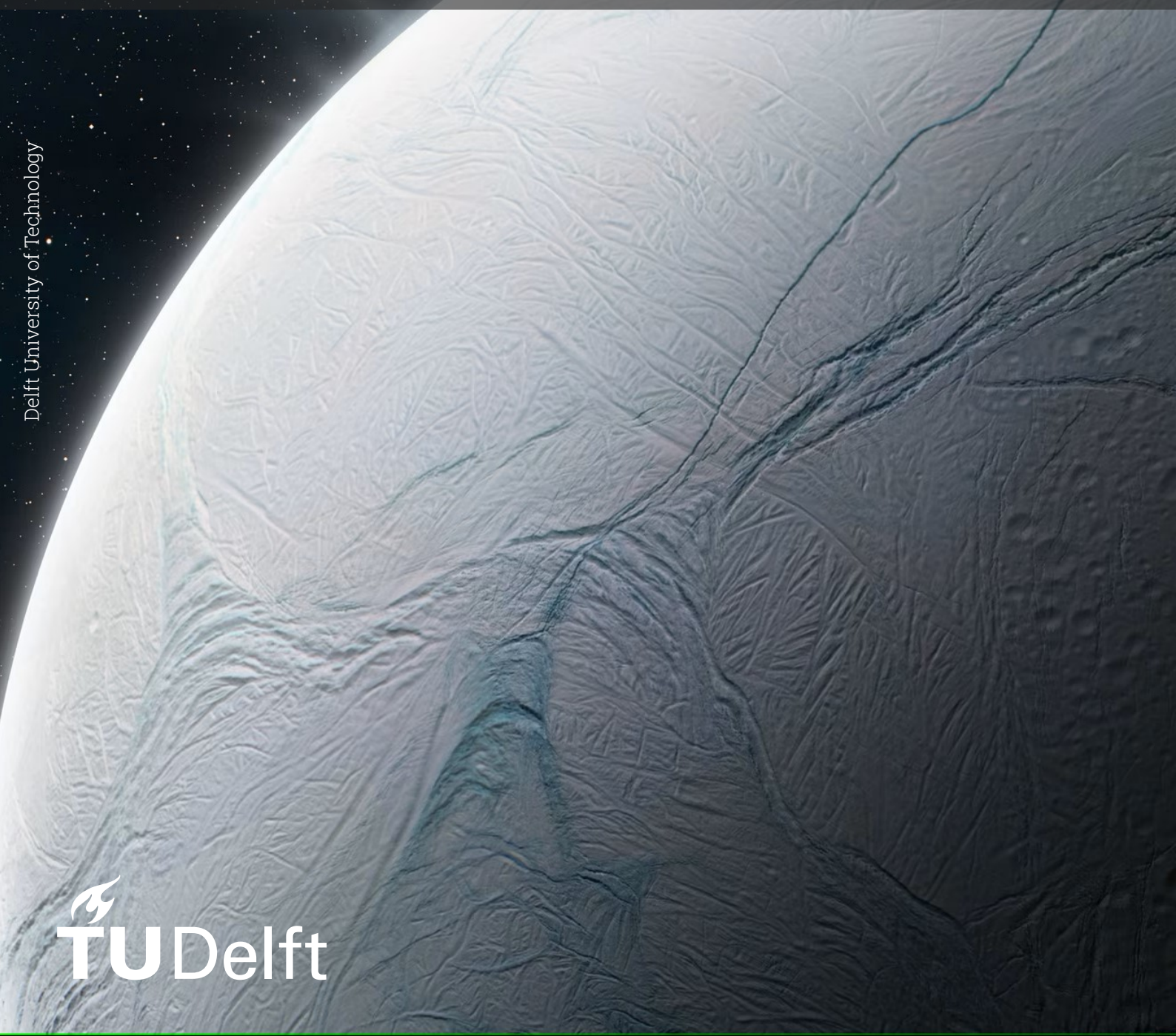

Delft University of Technology

TU Delft

Dynamics of Enceladus' Icy Plumes

Investigating the Physics of the Plumes using DSMC

by

Deepanshu Kamlesh Punjabi

Instructor:	Dr. Stéphanie Cazaux
Project Duration:	November, 2024 - October, 2025
Faculty:	Faculty of Aerospace Engineering, Delft

Cover: Illustration of vapor plumes erupting from the surface of Enceladus, Saturn's sixth largest moon by Tobias Roetsch, Future Publishing/Getty Images

Style: TU Delft Report Style, with modifications by Daan Zwaneveld

TU Delft

Acknowledgments

This thesis, titled ”Dynamics of Enceladus’ Icy Plumes: Investigating the Physics of the Plumes using DSMC” marks the culmination of my time as an Aerospace Engineering master’s student at Delft University of Technology.

This research would not have been possible without the guidance and support of many individuals. First, I would like to express my deepest and sincere gratitude to my supervisor Professor Stéphanie Cazaux. Her expertise, long insightful feedback, and consistent encouragement were invaluable in understanding the complexities of involved in understanding the plumes. Her passion for the subject was something that kept me going throughout the last 11 months along with the lovely energy that she has.

I would like to thank Professor Ferdinand Schrijer, who provided me with a second perspective on my research. His questions on the finer details of the simulations strengthened my understanding and gave me a lot of confidence. During my thesis, I was also a part of the Plumes research group where Stéphanie organized bi-weekly meetings with fellow students and researchers to show our findings and research while having detailed discussions about the same. I would also like to thank Yaël Bourgeois, Tara Bründl, Sebastian Oliver Scholts, Aïcha van Veen and Tim Mosimann for sharing their insights on my work and showing me their exciting research.

Looking back at the past 2 years, starting a new life in a new city and country has been the most challenging yet most memorable years of my life. I would like to sincerely thank my parents and my sister who have supported me throughout this journey and provided me with this opportunity to learn and grow in ways I could have never imagined.

To my friends, thank you for being there for me during the difficult times during my studies, especially my thesis. The countless meals, late night conversations and the memorable trips have made these two years unforgettable. I would also like to thank my girlfriend, who has been a constant source of support during my thesis especially when it felt like every other simulation was falling apart.

Thank you to everyone who helped me reach this milestone. Your support, however big or small, has become a core part of this thesis and my amazing time at TU Delft. This journey has been about more than just research, it’s been a time of profound personal and professional growth. With deep gratitude and a sense of accomplishment, I conclude my thesis and look forward to the next chapter.

Deepanshu Kamlesh Punjabi
Delft, October 2025

Summary

Enceladus, Saturn's sixth-largest moon, is a primary target for astrobiological research due to the discovery of icy plumes erupting from its south polar region. These plumes, originating from fissures known as the "Tiger Stripes," provide an insight into the subsurface liquid ocean lying underneath its icy crust. The observations by the Cassini spacecraft have fueled extensive modeling efforts using methods like Direct Simulation Monte Carlo (DSMC) to understand the plume dynamics. However, a fundamental question remains from the existing literature: do the plumes continuously accelerate as they expand from the moon's surface into the vacuum of space?

To answer this question, this thesis uses the dsmcFOAM solver within the OpenFOAM framework designed for performing DSMC simulations. This methodology is uniquely suited to model the rarefied gas dynamics of the plumes, accurately capturing the flow's transition from a dense, collisional regime near the vents to a free-molecular state at higher altitudes. The simulations model the expansion of both water gas and ice grain particles from the near-field region around the surface of the moon to the far-field region, allowing for a detailed analysis of the physics of the plumes.

The simulation results provide interesting observations about our understanding of the plumes. In the near-field region, the plumes exhibit significant acceleration, with flow characteristics that closely resemble a highly underexpanded nozzle jet. This initial acceleration is driven by the large pressure difference between the plume conditions at the surface and the vacuum of space. However, the introduction of ice grain particles in the flow leads to a significant deceleration of the mean flow velocity due to momentum transfer from the faster water gas particles to the larger ice grain particles. These results can be extended using existing study of underexpanded nozzles at different knudsen number values which indicated that the flow decelerates in the free molecular flow region.

Further analysis of the simulation data reveals that the growth of ice grains is influenced by their residence time within a specific flow region and the sticking coefficient of water molecules. The longer a grain resides in a dense part of the plume, the larger it can grow. However, the rate of growth is expected to decrease at higher altitudes as the plume's density and the relative velocity of particles diminish. The overall structure of the simulated plumes aligns really well with images captured by the Cassini spacecraft. The simulations successfully replicate key features of underexpanded jets, including expansion fans and shock structures like Mach disks, which can be observed in Cassini's high-resolution images of the plumes. This strong relation validates the model's ability to capture the fundamental physics governing the plume's expansion. By generating simulated occultation profiles from the model data, this study provides new insights into the observational data collected by Cassini's UVIS instrument. The comparison suggests that the distinct jets observed by Cassini may represent different stages of plume evolution. Jets with sharper, deeper optical depth profiles are likely decelerating and contain a higher concentration of particles, whereas jets with broader, shallower profiles are likely in a state of acceleration and greater expansion.

In conclusion, this thesis finds that the plumes of Enceladus do not continuously accelerate. Instead, they undergo an initial phase of rapid acceleration in the near-field region close to the surface, followed by which the flow starts to decelerate as they expand into the far-field, free-molecular flow regime at higher altitudes.

Contents

Acknowledgments i

Summary ii

List of Figures iv

List of Tables ix

Nomenclature x

1 Introduction 1
- 1.1 The Saturn System . . . 1
- 1.2 Enceladus . . . 2
- 1.3 Plumes of Enceladus . . . 3
- 1.4 Observations from Cassini . . . 3
  - 1.4.1 Onboard Instruments . . . 4
  - 1.4.2 Observations of the Surface of Enceladus . . . 4
  - 1.4.3 Observations of the Plumes of Enceladus . . . 7
  - 1.4.4 Properties of the Plumes . . . 9

2 Plume Models 10
- 2.1 Physics of the plumes . . . 10
- 2.2 The tiger stripe fractures . . . 11
- 2.3 Existing Models . . . 13
  - 2.3.1 DSMC Model . . . 13
  - 2.3.2 eDSMC Model . . . 14
  - 2.3.3 Collision Limiter Model . . . 14
- 2.4 Subsurface channel modeling . . . 14
- 2.5 Near-field flow dynamics modeling . . . 19
- 2.6 Far-field flow dynamics modeling . . . 20
- 2.7 Ice grain modeling . . . 22

3 Methodology 24

4 My Thesis 30
- 4.1 Modeling Framework . . . 31
  - 4.1.1 DSMC . . . 31
  - 4.1.2 OpenFOAM . . . 31
- 4.2 Simulation Setup . . . 31
  - 4.2.1 Functionality . . . 32
  - 4.2.2 dsmcFOAM Workflow . . . 32

5 OpenFOAM Set-Up 33
- 5.1 OpenFOAM Architecture . . . 33
  - 5.1.1 Time ’0’ directory . . . 33
  - 5.1.2 ’constant’ directory . . . 34
  - 5.1.3 ’system’ directory . . . 35
- 5.2 Simulation Set-up Process . . . 35
  - 5.2.1 Running the Simulation . . . 36

6 Validation and Verification 39
- 6.1 OpenFOAM test case . . . 39
- 6.2 Expansion of the test case . . . 42

6.2.1 Case 1 - Small Domain, Coarse Mesh . . . 42
6.2.2 Case 2 - Large Domain, Coarse Mesh . . . 46
6.2.3 Case 3 - Large Domain, Fine Mesh . . . 49
6.2.4 Case 4 - Icy Grains . . . 53
6.3 Discussion . . . 56

7 Results **60**
7.1 Case 5 . . . 60
7.2 Case 6 . . . 62

8 Post-Processing **66**
8.1 Grain growth . . . 66
8.2 Analysis . . . 68
8.3 The Occultation method . . . 74
8.4 Occultation results of the DSMC simulations . . . 75

9 Conclusions and Recommendations **78**
9.1 Conclusions . . . 78
9.2 Recommendations . . . 79

A Results for Cases 3a, 3b and 3c **85**
A.1 Case 3a . . . 85
A.2 Case 3b . . . 87
A.3 Case 3c . . . 89

B Far-Field Region Results (Case 7) **92**

C Growth of Ice Grain Particles **95**

List of Figures

1.1 The Saturn System [NASA/JPL, 2005] . . . 2
1.2 Enceladus (Image courtesy: NASA) . . . 2
1.3 Plumes of Enceladus captured by the Cassini spacecraft [Porco et al., 2014] . . . 3
1.4 Tiger Stripe fractures of Enceladus Schenk et al. [2018] . . . 4
1.5 CIRS temperature map of Enceladus from the July 14, 2005 en- counter showing an unexpected hot spot at the south pole [Newman et al., 2008] . . . 5
1.6 Impact crater density map showing the number of craters ≥ 2 km per unit area of Enceladus with the tiger strips outlined in black [Kirchoff and Schenk, 2009] . . . 5
1.7 Mass deposition rate of plume particles with grain sizes between $0.5\mu m$ and $5\mu m$ [Kempf et al., 2010] . . . 6
1.8 Map of the crystallinity factor on the surface of Enceladus [Newman et al., 2008] . . . 7
1.9 Volume mixing ratios based on the analysis of E5 flyby data presented in Waite Jr et al. [2009] . . . 8
1.10 Comparison of volatile abundances observed in Enceladus' plume with those seen in cometary comae [Waite Jr et al., 2009] . . . 8
1.11 Profiles of gas speed and temperature according to Schmidt et al. [2008] . . . 9

2.1 Artist's impression showing the physical processes that may occur to generate the plumes on Enceladus [Spencer and Nimmo, 2013] . . . 11
2.2 Cassini images of the south pole of Enceladus showing the tiger stripe fractures. (a) A red dot marks the south pole, and the yellow rectangle marks the location of panel (b). (b) The prominent fractures are the tiger stripes Damascus Sulcus, Baghdad Sulcus, and Cairo sulcus, and the yellow rectangle marks the location of panel (c). (c) Close-up of part of Cairo Sulcus and surrounding terrain. [Spencer and Nimmo, 2013] . . . 12
2.3 Subsurface configuration of the tiger stripe fractures [Spencer et al., 2018] . . . 13
2.4 Schematic view of the model used in Nakajima and Ingersoll [2016] with a uniform crack width. . . . 15
2.5 Pressure vs. depth relationships for ocean water returning to the ocean from the surface. Curve AD is the pressure for water with a mole fraction CO_2 of 0.0003. AE is the pressure vs. depth plot for water returning from plume chambers. Line AB is the lithostatic pressure in the ice [Matson et al., 2012]. . . . 15
2.6 Supply pressure vs. mole fraction CO_2. The vertical axis is drawn at the position of zero supply pressure [Matson et al., 2012]. . . . 16
2.7 Vertical profiles of the flow and ice walls. The black and gray lines correspond to Case 1 and the blue and sky-blue lines correspond to Case 11. The details of each case can be found in Nakajima and Ingersoll [2016]. The black and blue lines represent the physical parameters of the flow and the gray and sky-blue lines represent those of the ice walls. The green chain line in D represents an analytic solution for the mass flux into the ice walls. E at the surface of Enceladus is insensitive to the initial conditions [Nakajima and Ingersoll, 2016]. . . . 17
2.8 Heat flux to space as a function of the distance from the crack. The heat flux is most intense near the center of the crack and decreases sharply within several tens of meters away from the crack [Nakajima and Ingersoll, 2016]. . . . 17
2.9 Compositional and size profile of the ice plume discussed in detail in Postberg et al. [2011] 18
2.10 Simulation performed by Dhariwal et al. [2012] and Li et al. [2013] . . . 18
2.11 Contours of local Knudsen number, Kn,from (a) vent to 25 m and (b) vent to 10 km.(c)Contours of gas number density, n,from vent to 25 m.These are for Mach-5 vent conditions [Yeoh et al., 2015] . . . 21

2.12 H_2O density profiles in comparison to E3 INMS profile for the different fit cases taken from Yeoh et al. [2017] . . . 21
2.13 Grain results for an axisymmetric nozzle vent with an exit radius of 20m (a-c). (a and d) Terminal grain speeds (colored shapes) versus inlet position. Grain trajectories (b and e) and vertical speed (c and f) of grains versus vent height [Tucker et al., 2015] . . . 22

4.1 General workflow of dsmcFOAM [Scanlon et al., 2010] . . . 32

5.1 OpenFOAM Case Architecture ('Yellow' color box represents a directory and 'white' color box represents a file) . . . 34
5.2 *dsmcFoam* simulation set-up process . . . 35
5.3 Output after executing the *dsmcInitialise* command . . . 37
5.4 *dsmcFoam* initial process . . . 37
5.5 *dsmcFoam* output on the terminal window . . . 37

6.1 Geometry of the wedge case . . . 39
6.2 Boundary conditions and mesh of the wedge geometry . . . 40
6.3 Contour plots for various parameters from the OpenFOAM test case . . . 41
6.4 Individual particle velocities contour for the OpenFOAM test case . . . 41
6.5 Boundary conditions and mesh for Case 1 . . . 43
6.6 Mean velocity details for Case 1 . . . 44
6.7 Pressure details for Case 1 . . . 44
6.8 Translational Temperature details for Case 1 . . . 45
6.9 Mean Number density details for Case 1 . . . 45
6.10 Particle velocities contour for Case 1 . . . 46
6.11 Boundary conditions and mesh for Case 2 . . . 47
6.12 Mean velocity details for Case 2 . . . 47
6.13 Pressure details for Case 2 . . . 47
6.14 Mean number density details for Case 2 . . . 48
6.15 Translational temperature details for Case 2 . . . 48
6.16 Particle velocities contour for Case 2 . . . 48
6.17 Boundary conditions and mesh for Case 3 . . . 50
6.18 Number of equivalent particles in a mesh . . . 50
6.19 Mean velocity details for Case 3 . . . 51
6.20 Pressure details for Case 3 . . . 51
6.21 Mean number density details for Case 3 . . . 51
6.22 Translational temperature details for Case 3 . . . 52
6.23 Particle velocities contour for Case 3 . . . 52
6.24 Comparison of the normalized results obtained by Case 3 results and Yeoh et al. [2015] 52
6.25 Mesh and Boundary Conditions of Case 4 . . . 53
6.26 Mean velocity details of Case 4 . . . 54
6.27 Particles in the flow . . . 55
6.28 Pressure details of Case 4 . . . 55
6.29 Mean number density details of Case 4 . . . 55
6.30 Translational temperature details of Case 4 . . . 56
6.31 Mean velocity comparison of Cases 1, 2, 3, 3a, 3b and 3c . . . 57
6.32 Pressure comparison of Cases 1, 2, 3, 3a, 3b and 3c . . . 58
6.33 Mean Number Density comparison of Cases 1, 2, 3, 3a, 3b and 3c . . . 59
6.34 Translational temperature comparison of Cases 1, 2, 3, 3a, 3b and 3c . . . 59

7.1 Mean Velocity for Case 5 . . . 61
7.2 Pressure for Case 5 . . . 61
7.3 Mean number density for Case 5 . . . 62
7.4 Translational temperature for Case 5 . . . 62
7.5 Mean velocity details of Case 6 . . . 63
7.6 Particles in the flow . . . 63
7.7 Translational temperature details of Case 6 . . . 64

7.8 Pressure details of Case 6 . . . 64
7.9 Mean number density details of Case 6 . . . 64

8.1 Growth of ice grain particles in Case 4 for q = 0.2 for different residence times . . . 67
8.2 Growth of ice grain particles in Case 6 for q = 0.2 for different residence times . . . 68
8.3 Comparison of Cases 2 and 4 . . . 69
8.4 Comparison of Cases 5 and 6 . . . 69
8.5 Jet structure of a moderately underexpanded nozzle [Franquet et al., 2015] . . . 70
8.6 Jet structure of an highly underexpanded nozzle [Franquet et al., 2015] . . . 71
8.7 Jet structure of an highly underexpanded nozzle [Franquet et al., 2015]. The red dot on the contour on the left is the location at which the expansion fan ends as seen in the figure of the highly undereexpanded nozzle on the right. . . . 71
8.8 Jet structure of a very highly underexpanded nozzle [Franquet et al., 2015] . . . 72
8.9 Shockwave structure of an underexpanded nozzle jet for various Knudsen numbers: 0.0005 (a), 0.001 (b), 0.002 (c), 0.004 (d), and 0.008 (e) [Kashkovsky et al., 2023] . . . 72
8.10 Image captured by the ISS instrument onboard the Cassini spacecraft on 21st November 2009 at approximately 11000km . . . 73
8.11 Image captured by the ISS instrument onboard the Cassini spacecraft captured on 6th May 2015 (Image Courtesy: NASA) . . . 73
8.12 UVIS and INMS measurements are plotted versus angle about the center of Enceladus as viewed from Cassini's position during the 2010 UVIS observation. Time is relative to the closest approach for the E7 2009 flyby and relative to minimum ray height for the 2010 solar occultation . . . 75
8.13 Optical Depth variation of the plumes of Enceladus during the 2010 solar occultation showing distinct absorption features from gas jets labeled a-f [Hansen et al., 2011] . . . 75
8.14 Optical Depth results at 25m altitude for (0 902 0) m/s inlet . . . 77
8.15 Optical Depth results at 25m altitude for (0 4000 0) m/s inlet . . . 77

A.1 Mesh and particle velocity details for Case 3a . . . 85
A.2 Mean velocity details for Case 3a . . . 86
A.3 Pressure details for Case 3a . . . 86
A.4 Mean number density details for Case 3a . . . 86
A.5 Translational temperature details for Case 3a . . . 87
A.6 Mesh and particle velocity details for Case 3b . . . 87
A.7 Mean velocity details for Case 3 . . . 88
A.8 Pressure details for Case 3b . . . 88
A.9 Mean number density details for Case 3b . . . 88
A.10 Translational temperature details for Case 3b . . . 89
A.11 Mesh and particle velocity details for Case 3c . . . 89
A.12 Mean velocity details for Case 3c . . . 90
A.13 Pressure details for Case 3c . . . 90
A.14 Mean number density details for Case 3c . . . 90
A.15 Translational temperature details for Case 3c . . . 91

B.1 Boundary conditions and mesh for Case 7 . . . 92
B.2 Mean velocity details of Case 7 . . . 93
B.3 Pressure details of Case 7 . . . 93
B.4 Mean number density details of Case 7 . . . 94
B.5 Translational temperature details of Case 7 . . . 94

C.1 Growth of ice grain particles in Case 4 for q = 0.35 for different residence times . . . 95
C.2 Growth of ice grain particles in Case 4 for q = 0.50 for different residence times . . . 95
C.3 Growth of ice grain particles in Case 4 for q = 0.75 for different residence times . . . 96
C.4 Growth of ice grain particles in Case 4 for q = 1.00 for different residence times . . . 96
C.5 Growth of ice grain particles in Case 6 for q = 0.35 for different residence times . . . 97
C.6 Growth of ice grain particles in Case 6 for q = 0.5 for different residence times . . . 97
C.7 Growth of ice grain particles in Case 6 for q = 0.75 for different residence times . . . 98

C.8 Growth of ice grain particles in Case 6 for q = 1.00 for different residence times 98

List of Tables

1.1 Instruments onboard the Cassini Spacecraft . . . 4

3.1 Summary of the models with their observations and results . . . 26
3.2 Summary of the Initial Conditions for Numerical Simulations of Enceladus' Plumes . . . 28

5.1 Parameters defined in *dsmcProperties* . . . 34
5.2 Files listed in *system* directory . . . 35
5.3 Parameters defined in *blockMeshDict* file . . . 36
5.4 Parameters defined in *decomposeParDict* file . . . 36
5.5 Parameters defined in *dsmcInitialiseDict* file . . . 37
5.6 Parameters defined in *controlDict* file . . . 38

6.1 Initial conditions of the wedge case . . . 40
6.2 Validation of the wedge case . . . 41
6.3 Summary of the *dsmcFoam* cases . . . 42
6.4 Initial conditions for Case 1 . . . 43
6.5 Results summary after Case 1 . . . 46
6.6 Initial conditions for Case 2 . . . 46
6.7 Results summary after Case 2 . . . 49
6.8 Initial conditions for Case 3 . . . 49
6.9 Results summary after Case 3 . . . 53
6.10 Initial conditions for Case 4 . . . 54
6.11 Results summary after Case 4 . . . 56

7.1 Summary of cases for the far-field region . . . 60
7.2 Initial conditions for Case 5 . . . 60
7.3 Initial conditions for Case 6 . . . 63

8.1 Comparison of plume behavior at different inlet velocities . . . 70
8.2 Summary of UVIS occultation observations with water vapor detections [Hansen et al., 2011] . . . 74
8.3 Summary of the properties of the jets identified in Figure 8.13 [Hansen et al., 2011] . . . 76

A.1 Initial conditions for Case 3a . . . 85
A.2 Initial conditions for Case 3b . . . 87
A.3 Initial conditions for Case 3c . . . 89

B.1 Initial conditions for Case 7 . . . 92

Nomenclature

Abbreviations

Abbreviation	Definition
AU	Astronomical Units
CDA	Cosmic Dust Analyser
CFD	Computational Fluid Dynamics
CIRS	Composite Infrared Spectrometer
DSMC	Direct Simulation Monte Carlo
eDSMC	Equilibrium Direct Simulation Monte Carlo
ESA	European Space Agency
HS	Hard Sphere
INMS	Ion and Neutral Mass Spectrometer
ISA	International Standard Atmosphere
ISS	Imaging Science Subsystem
JPL	Jet Propulsion Laboratory
MAG	Magentometer
NASA	National Aeronautics and Space Administration
OpenFOAM	Open Source Field Operation And Manipulation
SPT	South Polar Terrain
UVIS	UltraViolet Iamging Spectrograph
VHS	Variable Hard Sphere
VIMS	Visible and Infrared Mapping Spectrometer
VSS	Variable Soft Sphere

1 Introduction

The Saturnian system with its diverse collection of moons always captured the fascination of scientists and public. Among these diverse set of moons, Enceladus, an icy moon, is one of the most intriguing planetary body in the solar system. One of the main reason of this fascination is the presence of a plumes erupting from its south pole. This chapter will provide an overview of the Saturnian system and then provide a brief introduction about Enceladus and its plumes. This chapter also discusses the observation made by the Cassini mission during its various flybys of the plumes of Enceladus.

1.1. The Saturn System

Saturn, the sixth planet in the solar system, best known for its system of planetary rings which makes it visually unique, has a small system of its own. This intricate system, with its vast structures and interplay of forces, has captured the imagination of scientists and the public alike.
Figure 1.1 is an artist's impression of the Saturnian system with its rings and some of the major icy moons. Saturn has 7 main rings, labeled in the order that they were discovered D, C, B, A, F, G and E with each having their own subdivisions, gaps, structures and moonlets within [NASA/JPL, 2005]. The D ring is faint and the closest to Saturn while rings A, B and C are the main rings. Just outside the A ring is the narrow F ring, shepherded by tiny moons, Pandora and Prometheus. Two much fainter rings, G and E, are located beyond that. The largest planetary ring in our solar system is Saturn's diffuse E ring, which stretches over 1 million km from Mimas' orbit to Titan's orbit. With sizes ranging from microns to tens of meters, the particles in Saturn's rings are mostly made of water ice. A great deal of structure can be seen in the rings at all scales; part of this complexity can be explained by gravitational interactions with Saturn's numerous moons, but much of it is still unknown. While the radial span of the main rings (A, B, and C) is 62,120 km, they are typically less than 100 m thick. With a potential age of only a few hundred million years, the major rings are far younger than the solar system [NASA/JPL, 2005].

Saturn is also known to have 146 moons, 64 of which have been provided formal names. Titan, the second-largest moon in the solar system, is the biggest and most prominent of Saturn's moons. Titan has a dense atmosphere that is mostly made up of nitrogen, along with clouds and lakes of liquid ethane and methane on the surface. Titan is a top candidate in the hunt for extraterrestrial life because of its dynamic hydrological cycle, which is powered by hydrocarbons, and the potential for a subterranean ocean.

The surface features of several mid-sized moons, including Tethys, Iapetus, Rhea, Dione, and Mimas, range from highly cratered terrains to indications of previous geological activity. While Dione and Rhea show signs of past tectonic processes and possible subsurface activity, Mimas, which is frequently compared to the Death Star because of its prominent Herschel Crater, is a rather inert body. The two-tone coloring of Iapetus, with one hemisphere coated in ice and the other in dark substance, makes it unusual. The smaller moons, sometimes known as moonlets, are encased in Saturn's recognizable rings. Through gravitational interactions, they include Pan, Atlas, and Daphnis, which shape and pre-

serve voids in the rings. The Saturnian system is made more diverse by irregularly shaped moons like Phoebe, which is believed to be a captured object from the Kuiper Belt, and Hyperion, which is notable for its erratic spin [NASA/JPL, 2005].

Figure 1.1: The Saturn System [NASA/JPL, 2005]

The sixth largest moon of Saturn, Enceladus, has drawn attention from planetary scientists because of its striking south polar plumes. A subsurface ocean in contact with a rocky core is suggested by these jets of water vapor, ice particles, and organic compounds that are emerging from tiger stripe fractures. Enceladus is one of the system's most dynamic moons due to its geological activity and the contributions its plumes make to Saturn's E-ring [Kempf et al., 2010].

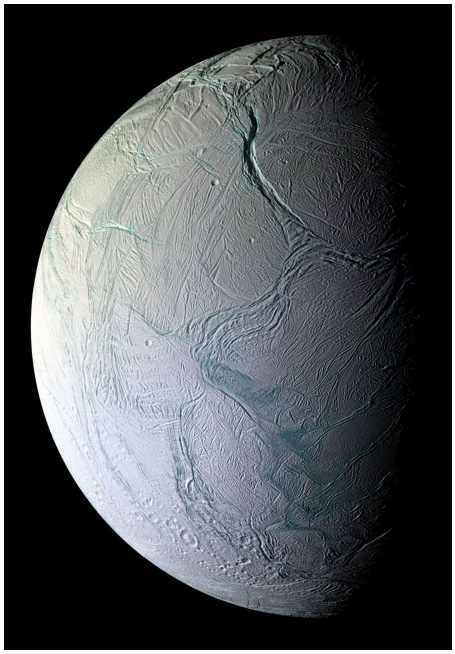

Figure 1.2: Enceladus (Image courtesy: NASA)

1.2. Enceladus

Enceladus, shown in Figure 1.2, named after a giant in Greek mythology, has the whitest, most reflective surface in the solar system. It has a diameter of approximately 504 km while orbiting Saturn between the moons Mimas and Tethys as seen in Figure 1.1. Enceladus' orbit has an eccentricity of 0.0047 orbiting Saturn at a distance of 238,000 km and completing an orbit once every 32.9 hours. It is at a

distance of approximately 9.5 AU from the Sun with gravity of about 0.113 m/s^2. The moon is also tidally locked with Saturn, thus keeping the same face towards the planet. Despite being tidally locked, the high reflectiveness of Enceladus keeps its surface temperature quite low at -201 °C [Schenk et al., 2018]. Enceladus is in orbital resonance with Dione, i.e., Enceladus orbits Saturn twice every time Dione orbits Saturn once. Tidal heating occurs within the moon as a result of Enceladus' orbit being stretched into an oval form by Dione's gravity, making it occasionally closer to Saturn and other times farther away [Nimmo et al., 2007]. In 2015, NASA's Cassini spacecraft discovered icy water particles and gas gushing at approximately 400 m/s from the south pole of Enceladus. These eruptions appear to be continuous and generates a very high amount of fine ice dust around Enceladus. These icy jets come from relatively warm fractures in the crust of Enceladus, now famously called the "Tiger Stripes" [Schenk et al., 2018].

1.3. Plumes of Enceladus

The sighting of the plumes in the south polar region of Enceladus changed the understanding of icy moons and their potential to be habitable. These plumes erupt from the tiger stripes, as mentioned earlier, contain a mixture of compounds that could offer information into the subsurface ocean that lies underneath the icy crust of Enceladus [Schenk et al., 2018].

Figure 1.3: Plumes of Enceladus captured by the Cassini spacecraft [Porco et al., 2014]

The fractures visible in the figure - four parallel prominent features named Alexandria, Baghdad, Cairo and Damascus - are tectonic faults that act as channels for the plumes to eject water vapor, ice particles and other materials from the subsurface ocean [Spencer et al., 2006]. Based on the observations made by the Cassini spacecraft (will be elaborated in detail in the subsequent sections) it was discovered that these eruptions are hotspots of thermal activity as the temperatures are significantly higher than the surrounding icy crust [Nimmo et al., 2007]. According to Nimmo et al. [2007], the plumes are believed to be driven by a combination of internal heating and surface processes. Enceladus' eccentric orbit around Saturn causes tidal heating which generates frictional heat within the icy crust helping it maintain a liquid subsurface ocean while also pressurizing the water near the tiger stripe fractures.

1.4. Observations from Cassini

The Cassini-Huygens mission, an ambitious collaboration between NASA, the European Space Agency (ESA), and the Italian Space Agency (ASI), fundamentally reshaped our understanding of Saturn, its rings, and its moons, especially Enceladus. As one of the most scientifically productive missions in planetary exploration, Cassini spent 13 years orbiting Saturn after its arrival in 2004. During its mission, it conducted numerous flybys of Enceladus, which revealed one of the most surprising and significant discoveries in planetary science: the active plumes of water vapor and ice particles erupting from Enceladus' south polar region. These observations highlighted Enceladus as a prime candidate for the harboring of extraterrestrial life and provided unparalleled insights into its subsurface ocean and geological activity.

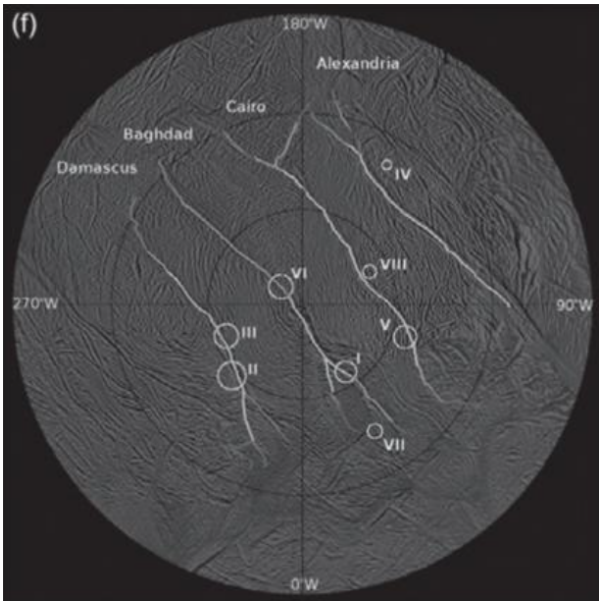

Figure 1.4: Tiger Stripe fractures of Enceladus Schenk et al. [2018]

1.4.1. Onboard Instruments

The Cassini spacecraft had many instruments onboard which were used to study various aspects of the Saturnian System. Some of the instruments which provided valuable information for Enceladus and the details of these instruments are discussed in Table 1.1.

Table 1.1: Instruments onboard the Cassini Spacecraft

Instrument	**Function**
Imaging Science Subsystem (ISS)	High-resolution imaging in visible and infrared wavelengths.
Ultraviolet Imaging Spectrograph (UVIS)	Detected ultraviolet light for composition analysis of gases and ices.
Composite Infrared Spectrometer (CIRS)	Measured thermal emissions to study temperature variations.
Visible and Infrared Mapping Spectrometer (VIMS)	Analyzed reflected light to determine surface composition.
Ion and Neutral Mass Spectrometer (INMS)	Measured the composition and density of gases in the plume and atmosphere.
Cosmic Dust Analyzer (CDA)	Analyzed the size, composition, and velocity of dust particles in the plumes.
Magnetometer (MAG)	Studied magnetic fields and interactions between the plume and Saturn's magnetosphere.

1.4.2. Observations of the Surface of Enceladus

The observations made by the Cassini spacecraft was instrumental in revealing the unique and dynamic nature of Enceladus. Cassini's observations of the moon's icy, reflective surface transformed our understanding of the geological processes, surface features and composition of Enceladus.

The discovery of the tiger stripes, a series of parallel fractures in the south polar region, was one of the most notable discoveries that was made by the Cassini spacecraft. These stripes are several kilometers in length and are the origin of the plumes of Enceladus [Schenk et al., 2018]. The CIRS measured relatively high temperatures in this region which characterized these fractures [Postberg et al., 2018]. The average temperature of the region surrounding the fractures is 70K while the temperatures along

the fractures can go upto 200K. Cassini's data also showed the presence of recurring geological activity with materials from the subsurface reservoirs periodically expelled through these fractures which resurface the area with fresh ice [Spencer and Nimmo, 2013]. According to Spencer and Nimmo [2013], tidal forces also play a crucial role in maintaining the fractures and driving the eruption of the plumes. Figure 1.5 reveals the Enceladus temperature map when comparing the predicted temperatures and the observed temperatures from the Cassini spacecraft [Newman et al., 2008].

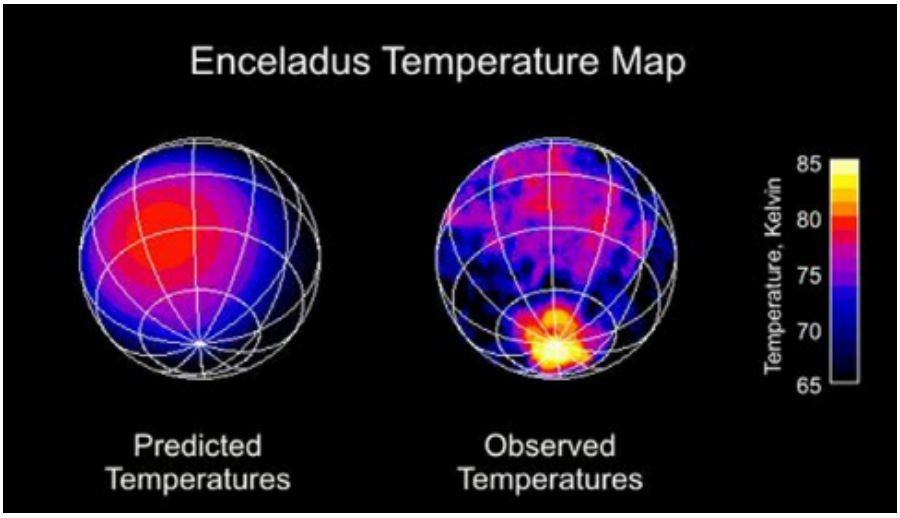

Figure 1.5: CIRS temperature map of Enceladus from the July 14, 2005 en- counter showing an unexpected hot spot at the south pole [Newman et al., 2008]

Cassini's data also revealed extensive tectonic deformation through ridges, troughs and fault systems criss-crossing across the surface of the moon. This evidence likely suggests the presence of internal stresses mostly driven by tidal interactions with Saturn [Schenk et al., 2018]. Blocks of ice are also visible on the surface, especially in the tectonically active areas, according to Cassini's high-resolution photography. These blocks, which range in size from 10 to 100 meters, most likely result from tectonic uplift [Spencer et al., 2006]. Enceladus's impact crater density and distribution offer important clues about the moon's geological past. A few or no craters indicate current resurfacing processes, while other areas, like the northern hemisphere, are severely cratered and seem ancient. For example, the south polar region has virtually no impact craters, which is compatible with tectonic activity and the ongoing deposition of plume material. The surface variation in crater density demonstrates Enceladus' dynamic past and sporadic geological renewal [Kirchoff and Schenk, 2009]. Figure 1.6 shows the Impact crater density map showing the number of craters ≥ 2 km per unit area of Enceladus [Kirchoff and Schenk, 2009].

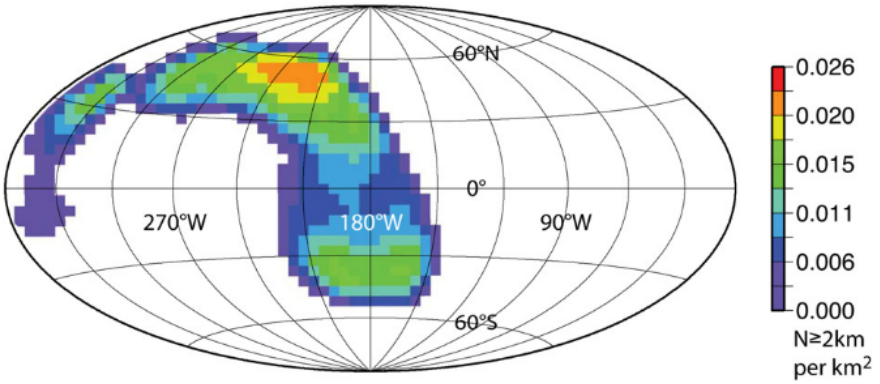

Figure 1.6: Impact crater density map showing the number of craters ≥ 2 km per unit area of Enceladus with the tiger strips outlined in black [Kirchoff and Schenk, 2009]

Enceladus has one of the brightest surfaces in the solar system reflecting over 80% of the sunlight which is due to its exceptionally high albedo [Spencer and Nimmo, 2013]. This brightness is attributed to its predominantly icy surface which is continually replenished by the plumes and its fallout depositing fine, fresh, water-ice onto the surface [Kempf et al., 2010]. Unsurprisingly, the surface composition as determined by near-infrared spectroscopy is almost pure water ice [Newman et al., 2008]. According to Brown et al. [2006], there are small amounts of CO_2, H_20_2 and maybe even NH_3. Apart from peroxide, which could be produced by oxidation of water, the composition of the surface stays consistent with the observed plume composition which will be discussed in the next section.

The spectral data from the VIMS revealed the variations in grain size and purity correlating with the geological activity. The grain size varies across the surface of the moon with the larger grains getting deposited near the tiger stripes according to Jaumann et al. [2008] through infrared spectroscopy. The research also concludes that the particle size decreases, the deposition of the particles starts moving outwards from the fractures. In a model by Kempf et al. [2010], Figure 1.7 shows the extent of the deposition till the plume particles are deposited on the surface of Enceladus. The deposition rates range from $0.5mm/year$ in the immediate vicinity of the fractures to about $10^{-4}mm/year$ at the equator.

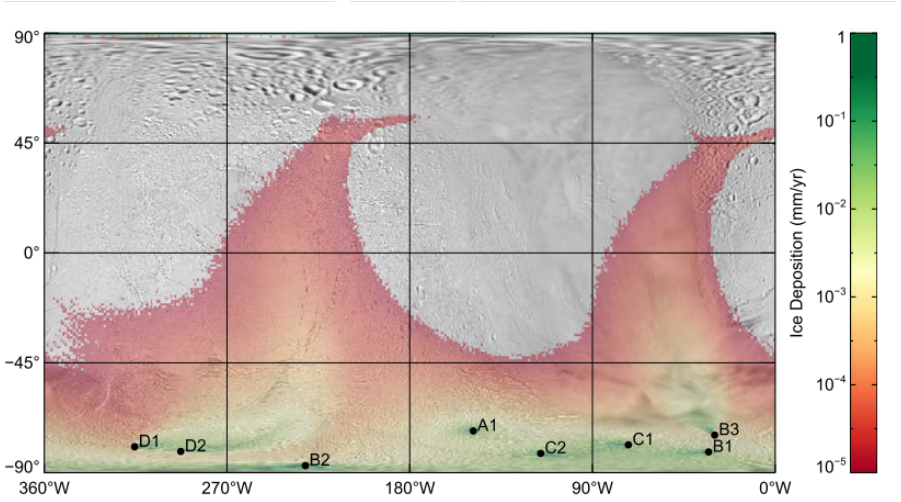

Figure 1.7: Mass deposition rate of plume particles with grain sizes between $0.5\mu m$ and $5\mu m$ [Kempf et al., 2010]

The findings from Newman et al. [2008] from indicate a major presence of crystalline particles on the surface of Enceladus. Figure 1.8 shows the crystallinity factor map of Enceladus showing the presence of crystalline and amorphous using observations made by the VIMS. The tiger stripes have been denoted using black outlines in the figure. It was created using the end-member amorphous spectrum from the region adjacent to tiger stripes and the end-member crystalline spectrum from the equatorial region. In this map, crystalline ice appears whiter/redder and amorphous ice as darker/bluer [Newman et al., 2008]. From Figure 1.8, it is evident that the tiger stripes are much more crystalline than the surrounding regions.

Cassini established a clear connection between Enceladus' surface processes and its contribution to Saturn's broader environment. The continuous ejection of plume material from the tiger stripes not only coats the surface with fresh ice but also replenishes Saturn's E-ring. The fallout from Enceladus' plumes serves as a primary source of resurfacing for the moon. Fine particles settle back onto the surface, especially in the south polar region, creating a smooth and reflective terrain. This process explains the striking albedo differences across Enceladus. Cassini's observations confirmed that material from the plumes contributes significantly to Saturn's diffuse E-ring. The icy grains ejected into space become entrained in the ring, maintaining its structure and composition. This interaction underscores Enceladus' importance in the dynamics of the Saturnian system [Hedman et al., 2009].

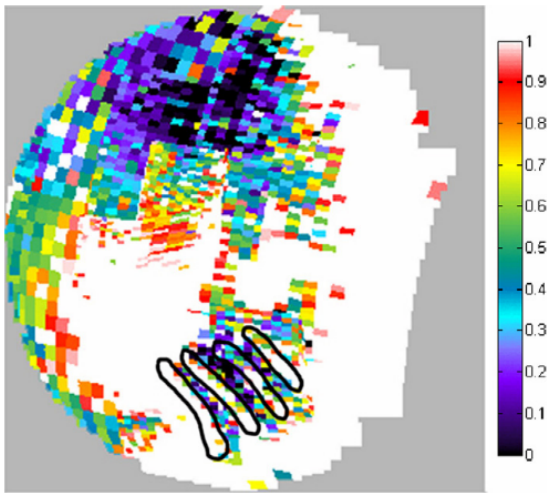

Figure 1.8: Map of the crystallinity factor on the surface of Enceladus [Newman et al., 2008]

1.4.3. Observations of the Plumes of Enceladus

The discovery of Enceladus' plumes in 2005 was initially unexpected. During a close flyby, the MAG detected anomalies in Saturn's magnetic field near Enceladus. These disturbances suggested the presence of an atmosphere or ionized gas cloud around the moon [Dougherty et al., 2006], which was unusual for a small, icy body with weak gravity. The magnetometer's findings were quickly followed by visual confirmation from Cassini's ISS, which captured high-resolution images of geyser-like jets emanating from the moon's south pole. These jets appeared to originate from long fractures in the surface which are now informally known as the "tiger stripes". The plumes were observed to extend hundreds of kilometers into space, creating a visible column of water vapor and icy particles. This discovery marked the first detection of active plumes on Enceladus and redefined its role in the Saturnian system [Porco et al., 2006].

The plumes of Enceladus are composed of a complex mixture of gases, icy particles, salts and organic compounds. The tiger stripes provide a direct window into the subsurface ocean of Enceladus which allowed for the creation of the plumes. Cassini's observations of these plumes and their composition are vital in revealing the internal dynamics and its potential habitability. Water vapor constitutes to approximately 92% of the gaseous emissions of the moon and this presence was confirmed by the INMS instruments of the Cassini during its E2 flyby during July 2015 [Postberg et al., 2018]. This observation also supports the hypothesis that the source of these plumes is a subsurface ocean underneath Enceladus' icy crust [Waite Jr et al., 2009]. The abundance of water vapor indicates that the ocean is in a liquid state, maintained by tidal heating resulting from Enceladus' orbital interactions with Saturn [Schenk et al., 2018]. The ejection of water vapor into space suggests a dynamic connection between the subsurface ocean and the surface through the crevasses in the ice shell.

In addition to water vapor, Cassini detected several volatile compounds within the plumes, each providing critical insights into the composition of the plumes of Enceladus'.

The presence of carbon dioxide (CO_2) in the plumes, identified by the INMS, suggests active chemical interactions between the ocean and Enceladus' rocky core. CO_2 could be dissolved in the ocean and released during hydrothermal activity or through other geochemical processes. Methane was also detected in small quantities and this molecule is of particular interest due to its potential biological and abiotic origins. According to Waite Jr et al. [2006], methane could be a byproduct of certain biological activities such as methano-genesis by hypothetical microbes in the subsurface ocean. Ammonia (NH_3) plays a vital role in the chemistry and physical properties of Enceladus' subsurface ocean. It acts as an antifreeze, lowering the freezing point of water and allowing the ocean to remain liquid at lower temperatures.One of the most significant findings was the detection of molecular hydrogen (H_2) in the plumes. This discovery, made during a close flyby in 2015, is a key indicator of ongoing hydrothermal processes. Hydrogen gas is likely produced by serpentinization reactions between water and silicate minerals in Enceladus' rocky core [Waite et al., 2017].

Cassini detected a variety of organic molecules in the plume material, ranging from simple hydrocarbons to more complex compounds. These findings are critical for understanding the astrobiological potential of Enceladus. The INMS identified simple hydrocarbons, such as methane, ethane, and formaldehyde, within the plume gases. These compounds can form naturally in hydrothermal systems or through interactions between organic precursors in the ocean and energy sources like tidal heating [Postberg et al., 2018].

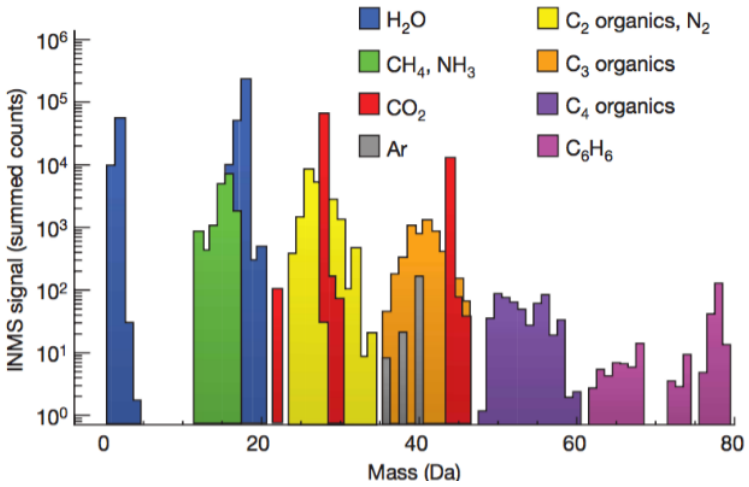

Figure 1.9: Volume mixing ratios based on the analysis of E5 flyby data presented in Waite Jr et al. [2009]

Cassini's analysis of the icy grains within the plumes revealed the presence of dissolved salts and minerals, which provide direct evidence of interactions between the ocean and the moon's rocky core. The CDA detected sodium chloride (NaCl) and other salts in the plume particles [Postberg et al., 2009]. The high salinity of these particles indicates that the plumes originate from a briny ocean. The presence of salts also confirms that the ocean is in direct contact with Enceladus' rocky core, where water can leach minerals from the rocks and carry them to the surface. The solid particles in the plumes are primarily composed of water ice, but they vary in size, composition, and structure. The majority of the icy grains in the plumes are micron-sized particles, which form as water vapor condenses and freezes upon reaching the frigid vacuum of space. These particles contribute to the deposition of fresh ice on Enceladus' surface, maintaining its high albedo.

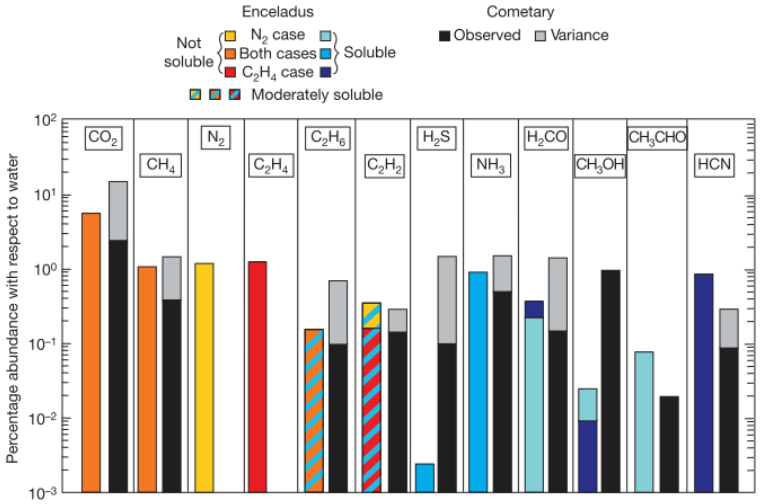

Figure 1.10: Comparison of volatile abundances observed in Enceladus' plume with those seen in cometary comae [Waite Jr et al., 2009]

The CDA also detected larger, aggregate particles, which are clusters of smaller ice grains bound together. These aggregates likely form within the crevasses before being ejected, and their presence suggests complex processes occurring within the fractures [Postberg et al., 2009]. The analysis of isotopic ratios in the plume material provided further insights into Enceladus' history and the origin of its subsurface ocean.

The D/H ratio in the water vapor of the plumes is similar to that observed in comets, suggesting a primordial origin for the water. This finding indicates that Enceladus' ocean may have been derived from the same reservoirs of water that formed comets in the early solar system [Waite Jr et al., 2009]. Figure 1.10 shows the abundances of CO_2, CH_4, C_2H_2, NH_3 and H_2CO (relative to H_2O) in the plume resemble those in comets, suggesting that these abundances are typical of well-mixed outer Solar System material. The plume may contain proportions of CH_3CHO and HCN that are somewhat elevated compared to comets. In contrast, the plume H_2S and CH_3OH abundances are significantly lower than those in comets [Waite Jr et al., 2009].

1.4.4. Properties of the Plumes

With all the observations discussed the earlier few sections, this section will summarize the properties of the plumes that are known. Ingersoll and Ewald [2011] discuss that the particles exiting the plumes have a wide range of speeds with approximately 10% of the particles exceeding the speed of $240m/s$. According to Schmidt et al. [2008], the gas part of the plume appears to be faster than the speed of the particles, however, it is difficult to constrain it. Hansen et al. [2011] estimates the speed of the gaseous phase to be around $450m/s$ with a few jets reaching speed of upto $1km/s$. Hansen et al. [2011] also provides estimates of the vent production rates from Enceladus at approximately $200kg/s$ for the gaseous phase and according to Ingersoll and Ewald [2011] its upto $50kg/s$ for the particles. Figure 1.11 shows the profiles of gas speed and temperature against the channel height for a channel geometry discussed in Schmidt et al. [2008].

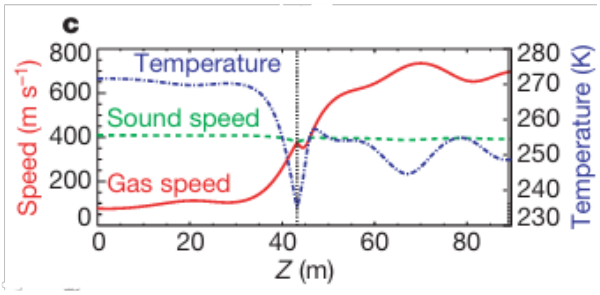

Figure 1.11: Profiles of gas speed and temperature according to Schmidt et al. [2008]

Ejection velocities have been measured in the range of 350-950 m/s by fitting the UVIS and INMS data [Dong et al., 2011, Schmidt et al., 2008]. Measured droplet sizes are mostly in the range of 0.1-1 µm [Hedman et al., 2009, Schmidt et al., 2008]. On the other hand Kempf et al. [2010] suggests that there are possibilities for particles with significantly larger sizes to occur (up to 75 µm), which fall back on to the planet's surface near the vents and are therefore not captured by Cassini's Visual and Infrared Mapping Spectrometer (VIMS). Also, wall interactions such as accretion and sublimation or tidal phenomena like frictional cracking can change the channel shape over time and thus allow for a wide variety of particle sizes to occur. Another possible explanation for the larger than expected particle sizes is the occurrence of boiling in the reservoir [Nakajima and Ingersoll, 2016]. The resulting bubbles burst to form a mix of vapour and tiny grains once they reach the reservoir surface. These droplets then have a much longer distance to travel until they reach the vent compared to particles formed in the main nucleation region close to the channel throat. As a result, the particles formed in the reservoir will grow significantly bigger. Regarding solid fraction, values in the range 0.07-0.2 have been measured for the plumes of Enceladus [Gao et al., 2016, Kieffer et al., 2009].

2

Plume Models

The observations from the Cassini mission revealed the dynamic nature of Enceladus' plumes and their connection to subsurface processes, such as tidal heating and pressure-driven ejections. To deepen understanding of these phenomena, this chapter focuses on models that simulate the physical and dynamic processes underlying plume formation, vent dynamics, and ice grain behavior. These models bridge observational data with theoretical insights, providing a framework to analyze the mechanisms driving the plumes.

2.1. Physics of the plumes

As discussed in the earlier sections, there is evidence of a liquid water ocean under the icy crust of Enceladus which plays a role in the production of the plumes. The assumption that the masses of gas and ice grains were similar—a significant amount of ice grains could result from severe boiling of a liquid source directly into space—was the foundation of the first arguments for a liquid-water source [Porco et al., 2006]. However, a few problems arise when trying to supply heat to liquid directly exposed to space fast enough to prevent it from freezing [Postberg et al., 2009]. Although the salty composition of the ice grains have a similar composition to that expected for water which has equilibrated with the presumed silicate core of Enceladus, thus providing strong evidence for the presence of subsurface liquid ocean. Postberg et al. [2009] avoids the problems of liquid water as it boils into a vacuum by proposing that water evaporates slowly over a larger area moving into pressurized chambers which then exit the through the narrow fractures on the surface. This process is illustrated in Figure 2.1.

The flash-frozen salty water droplets must subsequently be introduced into the plume using a method other than vigorous boiling. According to Postberg et al. [2009], gas bubbles may burst near the water's surface. Since the abundance of some plume gases, particularly CO_2 and CH_4, is significantly greater than what can be explained by their solubility in water, the presence of gas bubbles in the water seems conceivable [Waite Jr et al., 2009]. Therefore, unless a large portion of the water releases its dissolved gases and is subsequently recycled back to the ocean, these gases must be injected into the plume from a non-aqueous source.

Another concern is how heat is transferred to the plume source and to the surface, where Cassini measures it. According to Abramov and Spencer [2009], the thermal signature is in line with conductive heating of the surface caused by fractures at temperatures higher than 200 K. Movement of the plume gases up the fissures may supply the heat [Nimmo et al., 2007, Spencer et al., 2006] through convection, which is subsequently transferred to the near-surface ice by condensation of H_2O vapor on the fracture walls. Such condensation may shorten the lifespan of individual active fractures by closing the fissures at a rate of up to ~1 m per year. Shear heating caused by diurnal tides may produce the heat at shallow depths [Nimmo et al., 2007], , but its effectiveness depends on heat transfer to the surface. Higher temperatures reduce ice viscosity and heating rate, making the process self-limiting without efficient heat removal.

Gas bubbles in the water may lower its density sufficiently to enable it to rise buoyantly through the ice

crust [Crawford and Stevenson, 1988, Matson et al., 2012], and water rising through oceanic fissures can also carry heat to the top [Matson et al., 2012, Porco et al., 2014]. Fractures can be kept open by water pressure [Crawford and Stevenson, 1988]. Plume activity may be modulated by shifting diurnal tidal stresses [Hurford et al., 2007], and there is some observable support for this theory [Hedman et al., 2013]. It is possible to accelerate plume gases and particles to the supersonic speeds obtained from the observations made by the Cassini spacecraft when they ascend through the crevasses and enter the vacuum of space [Schmidt et al., 2008]. The considerably slower speeds of many of the bigger expelled particles could be explained by collisions with the creavasse walls.

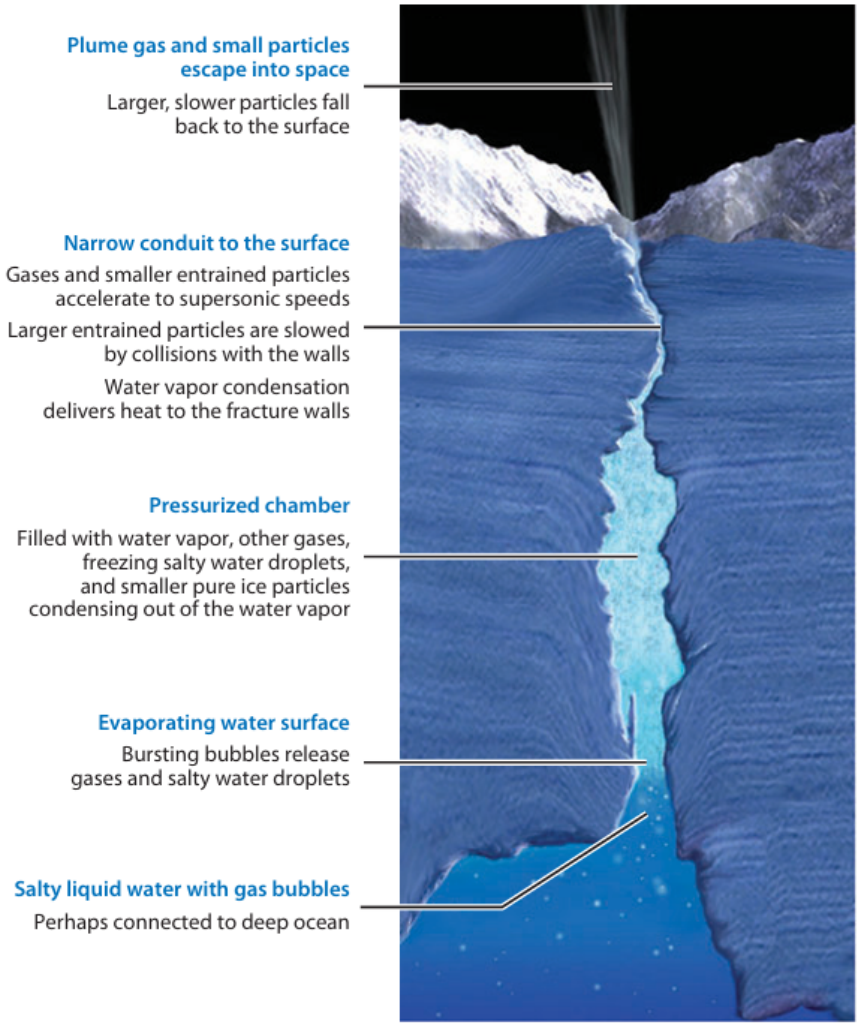

Figure 2.1: Artist's impression showing the physical processes that may occur to generate the plumes on Enceladus [Spencer and Nimmo, 2013]

2.2. The tiger stripe fractures

The tiger stripe fractures of Enceladus, located in the moon's south polar terrain, represent one of the most geologically dynamic regions in the Solar System. The tiger stripes — formally named Alexandria, Baghdad, Cairo, and Damascus sulci — are linear features approximately 130 kilometers in length and spaced 35 kilometers apart [Spencer et al., 2018]. Figure 2.2 shows images captured by the ISS instrument onboard the Cassini spacecraft of the South Polar Terrain (SPT) of Enceladus where the tiger stripes are located. Each stripe consists of a central trough flanked with a width of about 2km and depths of upto 500 meters. Observations suggest that the fractures are not simple linear features but complex systems containing multiple trenches and medial ridges [Spencer et al., 2018]. The thermal

emissions from these fractures are among the strongest and most intense on Enceladus with localized temperatures reaching as high as 200K (as discussed in section 1.4) and the surrounding icy terrain measuring typically around 70K.

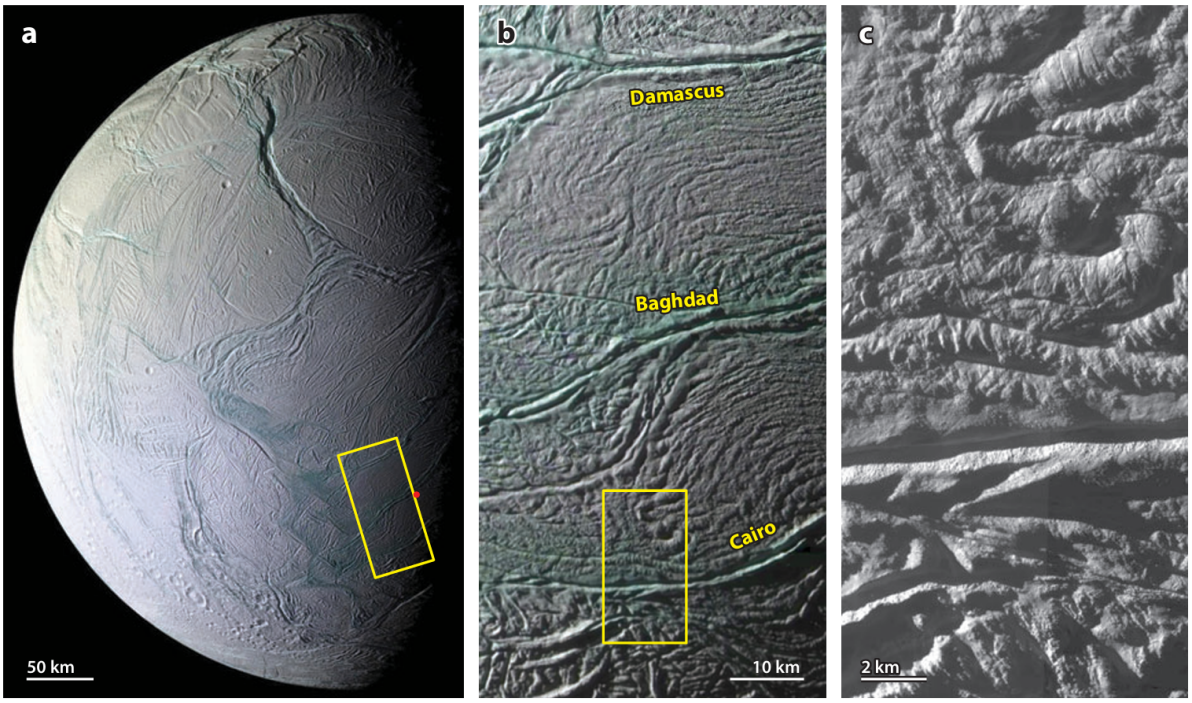

Figure 2.2: Cassini images of the south pole of Enceladus showing the tiger stripe fractures. (a) A red dot marks the south pole, and the yellow rectangle marks the location of panel (b). (b) The prominent fractures are the tiger stripes Damascus Sulcus, Baghdad Sulcus, and Cairo sulcus, and the yellow rectangle marks the location of panel (c). (c) Close-up of part of Cairo Sulcus and surrounding terrain. [Spencer and Nimmo, 2013]

Spencer et al. [2018] summarizes the current picture of the subsurface configuration of the tiger stripe fractures in Figure 2.3. It also represents the different principle processes that occur. The tiger stripe fractures are maintained by a delicate balance of physical processes, primarily driven by tidal flexing caused by Enceladus' orbital resonance with Dione. This flexing generates mechanical stresses that open and close the fractures, modulating plume activity. The periodicity of tidal stresses results in variations in plume intensity, with maximum ejections occurring when the moon is at its closest point to Saturn (periapse). The repeated opening and closing of the fractures dissipates mechanical energy, which is converted into heat. This heat further softens the ice near the fractures, preventing their complete closure and sustaining subsurface liquid pathways.

The fractures serve as direct paths connecting Enceladus's subsurface ocean to the vacuum of space. Water from the ocean is forced upward through these fractures due to pressure gradients and tidal pumping. The subsurface ocean is maintained under pressure by the overlying ice shell. When fractures form or widen due to tidal flexing, this pressure is partially relieved by the ejection of water and volatiles. Hydrothermal activity at the rocky core-ocean boundary introduces volatiles like methane, ammonia, and hydrogen into the ocean, enhancing the plume composition observed at the surface. Tidal flexing creates oscillatory pressure changes within the ice shell, driving water and vapor movement through the fractures. This "pumping" effect not only sustains the plumes but also helps to maintain open pathways by flushing out any ice or vapor that might seal the crevasses.

Heat is crucial for maintaining the fractures in an active state. The processes involved include tidal heating, latent heat from phase changes, and conduction of heat from below. As tidal stresses deform the ice shell, frictional dissipation generates heat, particularly in the warmer, more ductile ice near the base of the shell. This heat weakens the ice, making it more susceptible to cracking and allowing the fractures to remain active over long periods. When subsurface water ascends through the fractures and enters the vacuum of space, it undergoes rapid phase changes [Spencer et al., 2018]. The transition

from liquid water to vapor requires energy, which is drawn from the surrounding environment, cooling the immediate vicinity but preventing freezing deeper below. Ice near the fracture walls sublimates into water vapor due to the low pressure at the surface, further contributing to the observed plumes. Heat conducted upward from the subsurface ocean is radiated to space, particularly at the fracture margins. This process creates localized hotspots where temperatures can reach 200 K, significantly warmer than the surrounding terrain [Spencer et al., 2018].

The process of ejection involves the rapid ascent of water and vapor from the subsurface, driven by the pressure differential between the ocean and the vacuum of space. Observations suggest that the plumes are composed of discrete jets and continuous curtains of emission. These jets originate from specific locations within the fractures, likely where pressure and heat conditions favor strong ejections [Postberg et al., 2018]. The curtain-like emissions are thought to result from vapor escaping along the length of open fractures. Ice particles in the plumes form when vapor condenses during ascent. These particles are then ejected at high velocities, following ballistic trajectories influenced by Enceladus' low gravity. Larger particles tend to fall back to the surface, while smaller ones escape into Saturn's E-ring, continuously replenishing it [Postberg et al., 2009].

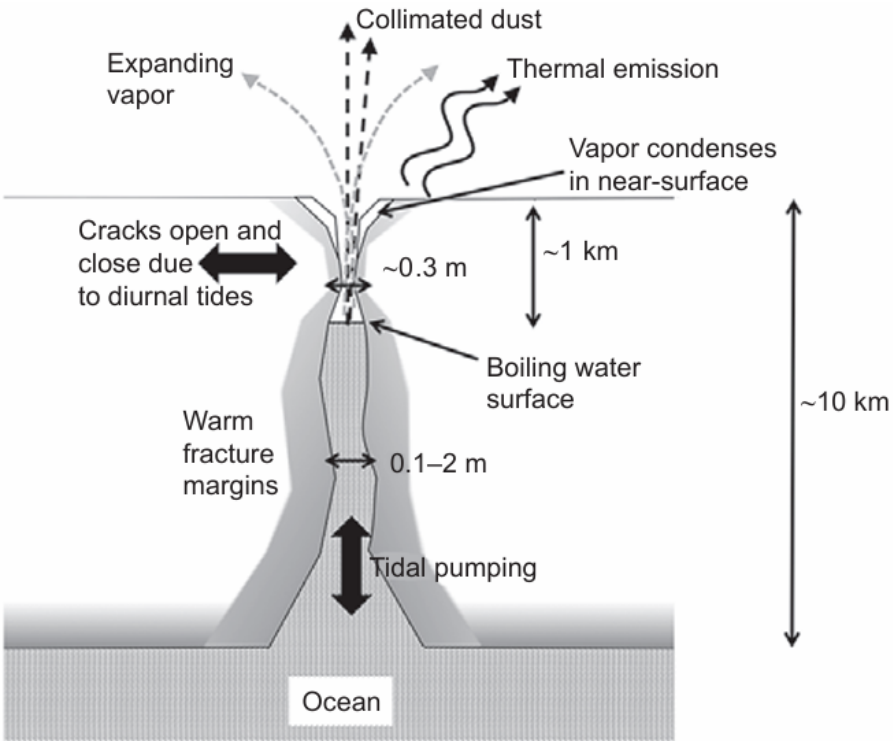

Figure 2.3: Subsurface configuration of the tiger stripe fractures [Spencer et al., 2018]

2.3. Existing Models

The tiger stripe fractures serve as pathways connecting Enceladus' subsurface ocean to space, driving the plumes' dynamic behavior. These plumes have been studied and modeled using various approaches like simple Discrete Series Monte Carlo (DSMC) models [Yeoh et al., 2015, 2017, Mahieux et al., 2019], equilibrium DSMC (eDSMC) models [Dhariwal et al., 2012, Li et al., 2013], collision limiter models [Dhariwal et al., 2012, Tucker et al., 2015] and various other approaches [Nakajima and Ingersoll, 2016, Teolis et al., 2017]. This section discusses the DSMC, eDSMC and the collision limiter models, which will be used to study the plume models extensively.

2.3.1. DSMC Model

The DSMC method models gas flows using a representative number of computational particles which mimic the motion and collisions of real gas molecules [Carlson and Bird, 1994]. Each computational

particle represents a very large number of real gas molecules. A DSMC domain is decomposed into cells in which particles move and collide. In DSMC, the particle movement and collision phases are decoupled and executed in sequence over a timestep, Δt, chosen to be much smaller than the mean collision time. Particles within the same cells are collided in a probabilistic manner. Between collisions, particles are translated under the influence of any force field present.

Macroscopic flow properties are computed by averaging over the appropriate molecular properties in each cell. Commonly, DSMC is employed to simulate the rarefied gas flows where the continuum assumption is not applicable, but it is always accurate physically because it solves the Boltzmann equation [Wagner, 1992]. However, for high-density flows this methodology becomes computationally expensive, continuum regime. As the plume flow expands from the surface vents into space, it spans several flow regimes, ranging from almost continuum at the vents to free-molecular at higher altitudes (with transitional flow in between). Because of its adaptability, DSMC is a good fit for modeling this flow. Furthermore, because DSMC takes into consideration the various internal molecular energy modes, it may capture the non-equilibrium effects found in such flows.

2.3.2. eDSMC Model

Expanding on the DSMC model is the equilibrium DSMC (eDSMC) model to the high pressure flows discussed in Titov and Levin [2007]. With this technique, a Maxwellian distribution of velocities in each cell is achieved by specifying an adequate number of collisions per particle every time step [Li et al., 2013]. The eDSMC approach requires specular boundary conditions for the gas-conduit surface interaction in order to provide an inviscid solution. The primary benefit of the eDSMC approach over DSMC is its ability to employ larger cell sizes and time steps, which the conventional DSMC method was unable to exploit under these circumstances. While the eDSMC technique allows us to select cell sizes of the order of flow gradients, the fundamental criterion for selecting cell sizes in the DSMC method is that they should be of the order of mean free path [Titov and Levin, 2007].

2.3.3. Collision Limiter Model

The gas distribution and trajectories of ice grains in the vents were simulated separately using a forward-modeling approach. This 2-step approach is commonly used for weak-comet dust studies [Rubin et al., 2011, Tenishev et al., 2011]. First the DSMC technique was used to model the gas flow, and secondly the results for the gas distribution were used in a test particle model to integrate the trajectories of ice grains due to the gas drag and gravitational force. Tucker et al. [2015] discusses that its 2D gas flow model is based in the principles of kinetic theory, but they use a continuum approach to integrate the grain trajectories. Bulk gas properties like viscosity and heat flux depend on the description of the interactions between individual molecules. The molecular collisions uses the variable hard sphere model for translational energy exchange and the Larsen Borgnakke model to describe internal energy exchange as discussed in Carlson and Bird [1994].

Based on the understanding of the models discussed above this section explores the implementation of the models in by categorizing them into subsurface channel dynamics, near-field flow behavior, far-field expansion, and ice grain modeling, to provide a comprehensive framework for analyzing plume phenomena.

2.4. Subsurface channel modeling

The architecture of subsurface channels critically influences their functionality in material transport. Nakajima and Ingersoll [2016] developed advanced models characterizing these channels as vertically elongated crevasses as shown in Figure 2.4, tapering from wide bases to narrow apertures near the surface. Their simulations identified an optimal configuration wherein crack widths narrow from approximately 1 meter at depth to as little as 0.05 meters near the surface (explained in detail in Nakajima and Ingersoll [2016]), effectively balancing material throughput with sustained vapor flow rates and heat flux. Excessively wide crevasses would result in diminished material control, whereas overly narrow channels would decrease flow efficiency. This tapering geometry provides a plausible explanation for localized thermal anomalies observed by instruments such as Cassini's Composite Infrared Spectrometer (CIRS). As ascending water vapor condenses along channel walls, the latent heat released

generates measurable thermal emissions. These emissions align spatially with the tiger stripe fractures, corroborating the models' geometric predictions [Nakajima and Ingersoll, 2016].

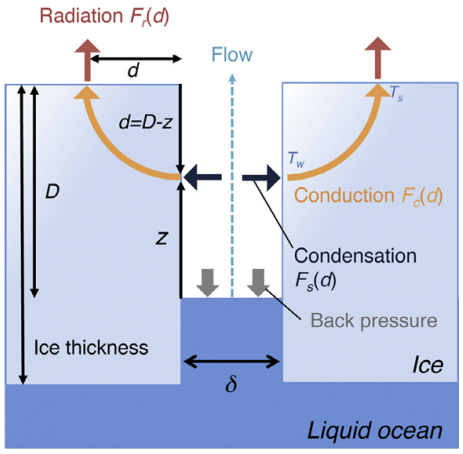

Figure 2.4: Schematic view of the model used in Nakajima and Ingersoll [2016] with a uniform crack width.

Studies using Direct Simulation Monte Carlo (DSMC) and equilibrium DSMC (eDSMC) techniques further validate these findings. These models simulate gas flow transitions from high-pressure regions near the ocean interface to supersonic flow conditions near the channel exits, aligning well with observed plume velocities [Yeoh et al., 2017, Li et al., 2013]. The vertical extent of these channels is equally critical. Matson et al. [2012] hypothesizes that subsurface pressure from the ocean drives water upward through channels extending several kilometers beneath the surface. This depth allows sufficient interaction between ascending water and volatile-rich layers, contributing to the composition and intensity of the ejected material [Matson et al., 2012]. The interaction of volatile materials with varying thermal zones within the channels may also contribute to their dynamic nature, enhancing transient phenomena such as plume pulsation.

Material transport within subsurface channels is orchestrated by complex interactions among pressure gradients, thermodynamic phase changes, and fluid dynamics. Matson et al. [2012] emphasized the pivotal role of gas exsolution in initiating buoyancy-driven ascent. The relation between pressure and depth relationships for ocean water returning to the ocean from the surface has been shown Figure 2.5. Dissolved gases such as CO_2 exsolve from the rising water as pressure decreases, reducing the density of the water column and facilitating upward transport [Matson et al., 2012]. The variation of CO_2 mole fraction along supply pressure obtained by Matson et al. [2012] has been shown in Figure 2.6.

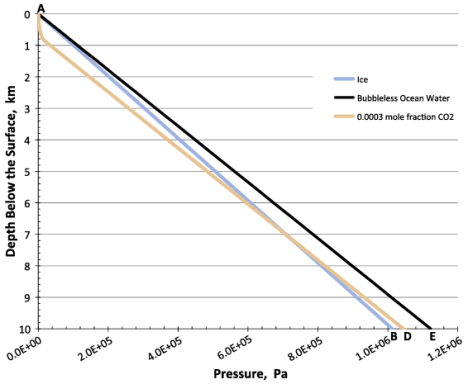

Figure 2.5: Pressure vs. depth relationships for ocean water returning to the ocean from the surface. Curve AD is the pressure for water with a mole fraction CO_2 of 0.0003. AE is the pressure vs. depth plot for water returning from plume chambers. Line AB is the lithostatic pressure in the ice [Matson et al., 2012].

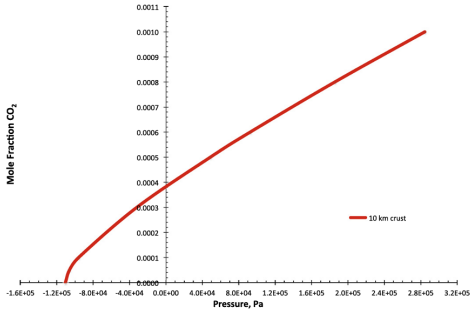

Figure 2.6: Supply pressure vs. mole fraction CO_2. The vertical axis is drawn at the position of zero supply pressure [Matson et al., 2012].

Nakajima and Ingersoll [2016] incorporated sophisticated fluid dynamics equations to model the forces at play within these crevasses which are disucssed in great detail in the paper. The key factors include:

- Frictional resistance imposed by the icy channel walls.
- Momentum conservation governing the fluid's vertical motion.
- Thermal gradients influencing condensation rates and material phase transitions.

Their findings demonstrate that vapor flow rates are acutely sensitive to channel geometry and depth. Figure 2.7 shows the variations of various parameters like pressure, temperature and velocity with the depth of the channel. It shows the vertical profiles of water vapor and ice particles for different channel widths and depths which are discussed in detail in Nakajima and Ingersoll [2016]. The models indicate that optimal channel design sustains sufficient basal pressure to propel material while ensuring a constricted surface exit for high-velocity plume ejection [Nakajima and Ingersoll, 2016]. Additionally, multi-phase flow interactions, encompassing liquid water, water vapor, and entrained particles, introduce further complexities. Phase transitions triggered by temperature and pressure fluctuations along the channel influence plume composition and variability observed during Cassini's flybys [Nakajima and Ingersoll, 2016, Matson et al., 2012]. Variability in plume intensity and ejection velocity underscores the non-linear interplay of fluid and thermal dynamics, which remain subjects of ongoing research.

Heat transfer processes within subsurface channels are critical for sustaining material transport and generating surface thermal anomalies. Matson et al. [2012], Nakajima and Ingersoll [2016] concur that latent heat released during water vapor condensation is the dominant thermal mechanism along channel walls. This heat is efficiently conducted through the surrounding ice, producing the localized warming observed near the tiger stripes [Nakajima and Ingersoll, 2016, Matson et al., 2012]. Thermal conduction models reveal that heat transfer efficacy is modulated by channel width and depth. Narrower channels near the surface enhance localized heat release, thereby amplifying surface heat flux density. Concurrently, the subsurface ocean supplies thermal energy via convective processes, sustaining the overall heat budget necessary for plume activity [Matson et al., 2012]. Figure 2.8 shows the results heat flux distribution to space as a function of the distance from the crack obtained by Nakajima and Ingersoll [2016].

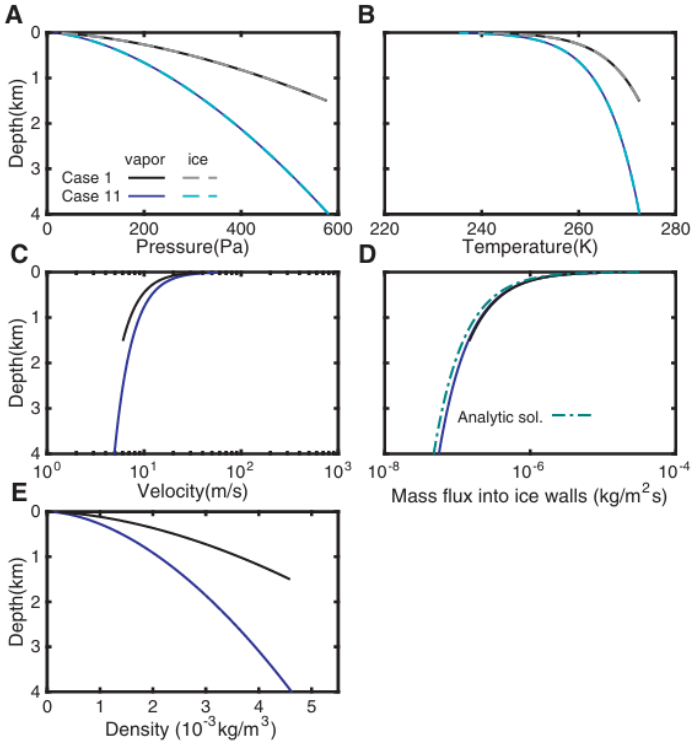

Figure 2.7: Vertical profiles of the flow and ice walls. The black and gray lines correspond to Case 1 and the blue and sky-blue lines correspond to Case 11. The details of each case can be found in Nakajima and Ingersoll [2016]. The black and blue lines represent the physical parameters of the flow and the gray and sky-blue lines represent those of the ice walls. The green chain line in D represents an analytic solution for the mass flux into the ice walls. E at the surface of Enceladus is insensitive to the initial conditions [Nakajima and Ingersoll, 2016].

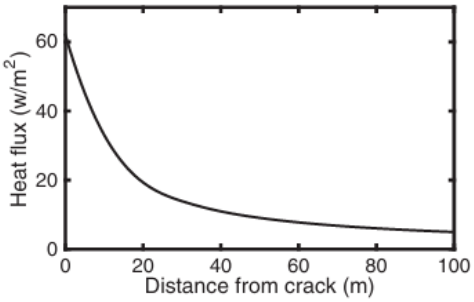

Figure 2.8: Heat flux to space as a function of the distance from the crack. The heat flux is most intense near the center of the crack and decreases sharply within several tens of meters away from the crack [Nakajima and Ingersoll, 2016].

Turbulent dissipation within the channels also contributes to heat transfer. Studies indicate that turbulence generated by tidal forces helps maintain liquid water near the channel interfaces, ensuring a steady supply of energy for plume activity [Porco et al., 2014, Kite and Rubin, 2016]. Convective heat flux within the subsurface ocean further contributes to thermal dynamics. Rising plumes of warmer water within the ocean's interior deliver additional thermal energy to the channel bases, ensuring a consistent energy supply to support prolonged activity [Matson et al., 2012]. Furthermore, the interaction of salt gradients within the ocean may influence thermal circulation patterns, indirectly affecting channel heat flux and plume output.

Gas-ice interactions within subsurface channels are pivotal in shaping the composition of ejected plumes. Postberg et al. [2011] explored the mechanisms underlying the formation of salt-rich ice grains, emphasizing processes such as condensation and accretion within these crevasses. The findings include [Postberg et al., 2011]:

- Salt-rich grains originate directly from the saline subsurface ocean, preserving its chemical signatures.
- Grains grow as ascending water vapor condenses onto existing particles, influenced by temperature and vapor saturation levels.

Nakajima and Ingersoll [2016] models provide further insights into the entrainment of ice grains by high-velocity vapor flows. The drag forces exerted by the gas ensure efficient ejection of grains into space, consistent with observed particle distributions in the plumes [Nakajima and Ingersoll, 2016]. Additional interactions, such as sublimation and particle collisions during ascent, further refine grain size and composition. These processes critically determine the characteristics of the material ultimately deposited on Enceladus' surface or ejected into its exosphere and Figure 2.9 shows how the compositional and size profile of the ice plume changes after it exits the vents [Postberg et al., 2011].

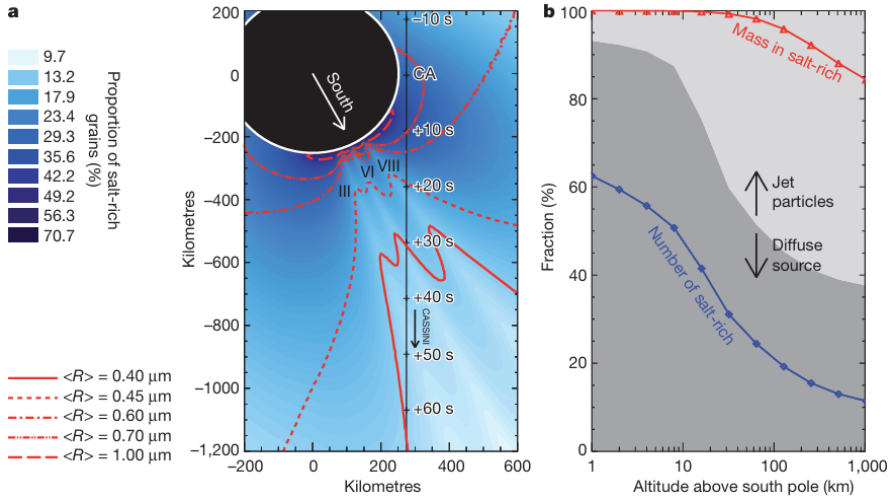

Figure 2.9: Compositional and size profile of the ice plume discussed in detail in Postberg et al. [2011]

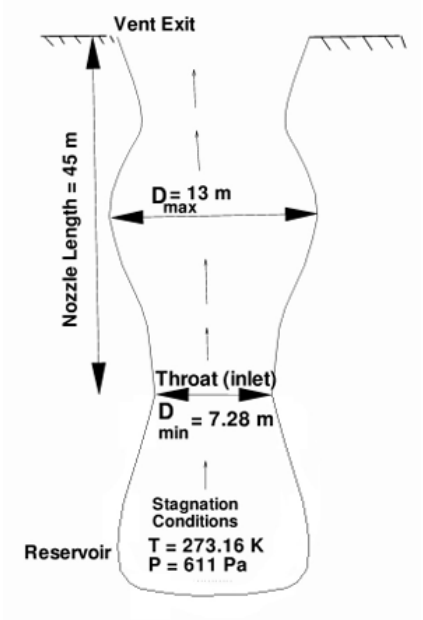

(a) Nozzle geometry used in Dhariwal et al. [2012] and Li et al. [2013]

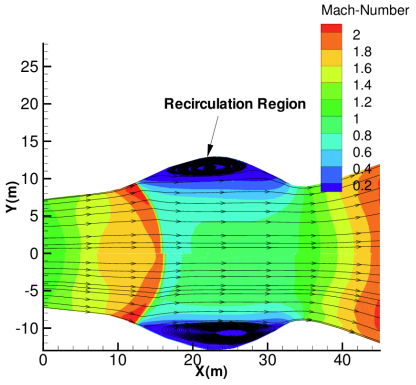

(b) Mach number and streamlines plot for eDSMC (top) and Euler (bottom) cases [Dhariwal et al., 2012]

Figure 2.10: Simulation performed by Dhariwal et al. [2012] and Li et al. [2013]

The geometry of Enceladus' vents plays a pivotal role in determining the flow structure and dynamics of the plumes. Commonly modeled as converging-diverging nozzles, these vents accelerate gas and entrained particles to supersonic velocities. Variations in vent dimensions, wall surface roughness, and thermal properties significantly influence the flow regime, particle trajectories, and condensation dynamics. Recent studies have explored how modifications in vent shape and surface properties alter the stability and coherence of the ejected plumes. Narrow vents with high-pressure throat conditions generate supersonic flows, reaching gas velocities of approximately 374 m/s, while entrained ice grains achieve lower velocities due to differential drag forces [Dhariwal et al., 2012]. These supersonic flows define the initial plume structure and collimation, providing a framework for interpreting the spatial and spectral properties of observed plumes [Nakajima and Ingersoll, 2016]. Complex vent geometries, such as double-throat nozzles, induce recirculation zones that affect ice grain growth and sublimation, leading to stratified velocity and size distributions. The vent geometry used Dhariwal et al. [2012] shown in Figure 2.10, shows recirculation zones in certain regions of the geometry and this can be seen in the Mach number contour plot with streamlines in Figure 2.10. These phenomena have been linked to the observed variability in plume density and composition, particularly in regions of localized particle clustering [Dhariwal et al., 2012]. Thermal interactions between the vent walls and the gas flow significantly influence condensation rates, particularly near the vent exit. Wall cooling enhances local supersaturation, promoting the growth of ice grains and the clustering of particles within the plume core. Such interactions are critical for explaining the fine-scale heterogeneities observed in plume imagery [Yeoh et al., 2015, Mahieux et al., 2019].

2.5. Near-field flow dynamics modeling

The investigation of near-field plume flow dynamics on Enceladus reveals intricate processes governing plume ejection, the interactions between gas and ice grains, and the transition from dense, collisional flow regimes within subsurface vents to the free-molecular flow conditions observed at higher altitudes. This critical transition zone, spanning from the vent exit to several kilometers above the surface, serves as a nexus for understanding the interplay of subsurface thermodynamics, vent geometry, and physical plume characteristics. These dynamics not only influence the observable properties of Enceladus' plumes but also provide indirect evidence for subsurface conditions, including the nature of its hypothesized ocean and potential habitability. The following section discusses the primary modeling techniques and findings from the studies performed in this domain.

Near-field plume dynamics are most effectively explored using the Direct Simulation Monte Carlo (DSMC) method. DSMC is particularly suited to simulating transitional and rarefied flow regimes, capturing molecular collisions, energy exchanges, and complex particle behaviors that are characteristic of Enceladus' environment. Enhancements to the method, such as equilibrium DSMC (eDSMC) for dense regions and collision-limiter adaptations for varying Knudsen numbers, have further refined its applicability [Li et al., 2013, Dhariwal et al., 2012]. Additionally, hybrid approaches integrating computational fluid dynamics (CFD) for high-density regions and DSMC for rarefied flows could emerge as valuable tools for addressing challenges posed by multiscale dynamics. Furthermore, parametric studies of plume behaviors under varying vent geometries and subsurface conditions have expanded the applicability of these methods to a range of celestial bodies, from icy moons to comets [Mahieux et al., 2019].

Li et al. [2013] utilized eDSMC to model the dynamics of gas and ice grains in subsurface channels and vent exits. The simulations demonstrated that the gas flow transitions from a continuum regime within the channels to a free-molecular regime upon exiting the vents. The findings underscored the sensitivity of plume dynamics to parameters such as vent geometry, subsurface pressure, and gas temperature [Li et al., 2013, Dhariwal et al., 2012]. Dhariwal et al. [2012] developed an overlay technique to simulate ice grain trajectories superimposed on a background gas flow field. By incorporating grain acceleration and gas-grain interactions, their work illuminated the influence of grain size distributions on plume opacity, velocity profiles, and spatial dispersion. These results provided key insights into the variability of observable plume properties [Dhariwal et al., 2012].

Yeoh et al. [2015] applied two-phase flow DSMC models to capture the coupled dynamics of water vapor and ice grains. Their study highlighted the role of condensation and evaporation in shaping grain distributions, as well as the implications of heterogeneous nucleation for observational signatures.

They further investigated the feedback mechanisms between gas dynamics and grain growth, offering a comprehensive view of the plume's evolution [Mahieux et al., 2019].

The near-field plume dynamics involve intricate interactions between water vapor and entrained ice grains. These interactions are governed by momentum transfer, phase changes, and differential acceleration mechanisms, which collectively shape the plume's observable properties. Furthermore, the chemical composition and structural dynamics of the grains provide insights into subsurface processes and oceanic conditions. Drag forces exerted by the gas accelerate smaller ice grains to velocities closer to the gas phase, while larger grains decouple earlier and maintain slower, collimated trajectories. This differential acceleration produces distinct velocity stratifications within the plume, influencing both its spatial distribution and optical thickness. The variation in grain velocities is crucial for understanding plume dispersal patterns observed in Cassini data [Yeoh et al., 2015, Tucker et al., 2015]. Supersaturation near the vent promotes rapid condensation, leading to grain growth, whereas sublimation occurs at higher altitudes where temperatures and pressures decline. These phase changes alter the size distribution of grains and contribute to the evolution of the plume's composition with altitude. Observational data confirm the presence of layered grain populations, consistent with these modeled behaviors [Yeoh et al., 2017, Dhariwal et al., 2012]. Observations reveal that micron-sized grains remain collimated within ten vent diameters due to their higher coupling with the gas flow, while smaller grains disperse more broadly. These behaviors align with high-resolution Cassini imaging of narrow plume cores and have been quantitatively validated by advanced DSMC models [Yeoh et al., 2015, Mahieux et al., 2019].

2.6. Far-field flow dynamics modeling

The far-field dynamics of Enceladus' plumes constitute a critical framework for deciphering the moon's geophysical activity, subsurface composition, and interactions within Saturn's environment. These plumes, emanating from Enceladus' south polar tiger stripes, undergo complex transformations as they expand from the collisional near-field regime to the free-molecular domain at higher altitudes.

The evolution of plume flow from a dense, collisional regime near the vent to a free-molecular state at elevated altitudes is a defining feature of far-field dynamics. At low altitudes, the high density of molecules ensures frequent inter-particle collisions, maintaining continuum-like behavior with Knudsen numbers below 0.1. As the plume expands, molecular collisions diminish, transitioning the flow to a free-molecular regime characterized by Knudsen numbers exceeding unity [Yeoh et al., 2015]. This transition is effectively captured through Direct Simulation Monte Carlo (DSMC) methods, which provide a statistical framework for modeling molecular behavior in regimes where traditional computational fluid dynamics (CFD) approaches are inadequate. Yeoh et al. [2015] employed DSMC techniques to simulate the transition of Enceladus' plume from collisional to free-molecular behavior over several kilometers and Figure 2.11 shows the contours of local knudsen number at 25 m and 10 km altitude. Their analysis elucidated the altitudinal thresholds of this transition and the role of vent parameters in shaping the extent of the collisional zone [Yeoh et al., 2015].

Far-field plume dynamics have been validated against observational data from Cassini's INMS and UVIS instruments. The variation of H_2O density has been plotted along with the INMS data for the E3 flyby for different fit cases discussed in Yeoh et al. [2017] has been shown in Figure 2.12. These datasets provide detailed measurements of gas densities, velocities, and compositions along Cassini's trajectories, enabling robust comparisons with numerical models. Yeoh et al. [2017] successfully replicated INMS density measurements using a free-molecular model extending plume simulations into the far-field. Their study found that observed H_2O densities during Cassini's E3, E5, and E7 flybys were consistent with venting rates of 400–500 kg/s. UVIS optical depth measurements further corroborated these findings by quantifying plume density distributions at higher altitudes [Yeoh et al., 2017]. Schmidt et al. [2008] explored the role of ice grain dynamics in explaining the plume's optical brightness variations as observed by Cassini imaging instruments. Their models demonstrated how grain size distributions and spatial arrangements influence light scattering properties, shaping the plume's observed appearance [Postberg et al., 2011].

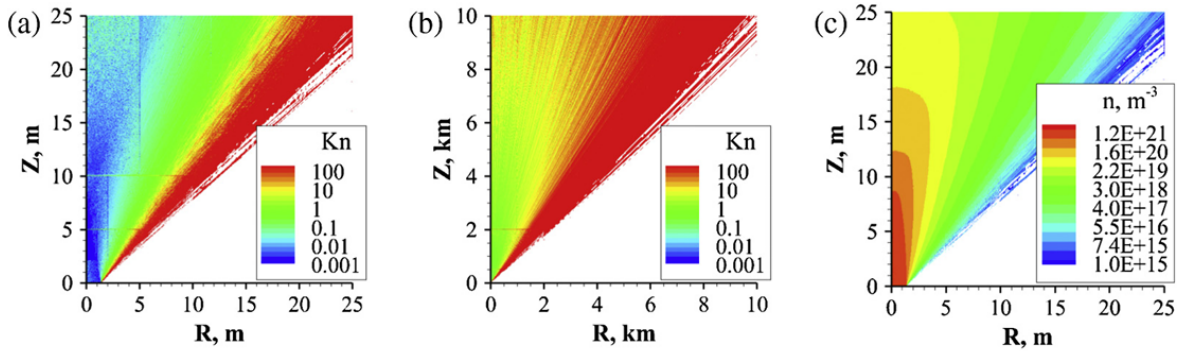

Figure 2.11: Contours of local Knudsen number, Kn,from (a) vent to 25 m and (b) vent to 10 km.(c)Contours of gas number density, n,from vent to 25 m.These are for Mach-5 vent conditions [Yeoh et al., 2015]

Mahieux et al. [2019] expanded on these insights by developing parametric models to describe critical field parameters, including density, velocity, and temperature, at altitudes up to 10 km. These models circumvent the computational expense of iterative DSMC simulations while enabling predictions across varied vent conditions. The results revealed that the transition altitude is highly sensitive to parameters such as vent mass flow rate, temperature, and pressure [Mahieux et al., 2019]. Vent conditions, encompassing diameter, mass flow rate, gas composition, and temperature, critically dictate the plume's far-field properties. These parameters influence initial velocity, thermal distribution, and density profiles. Yeoh et al. [2017] analyzed these relationships by simulating plume behavior under Mach-3 and Mach-5 vent conditions. The findings indicated that higher Mach numbers yield narrower, more collimated plumes, while lower Mach numbers produce broader, diffuse profiles [Yeoh et al., 2017].

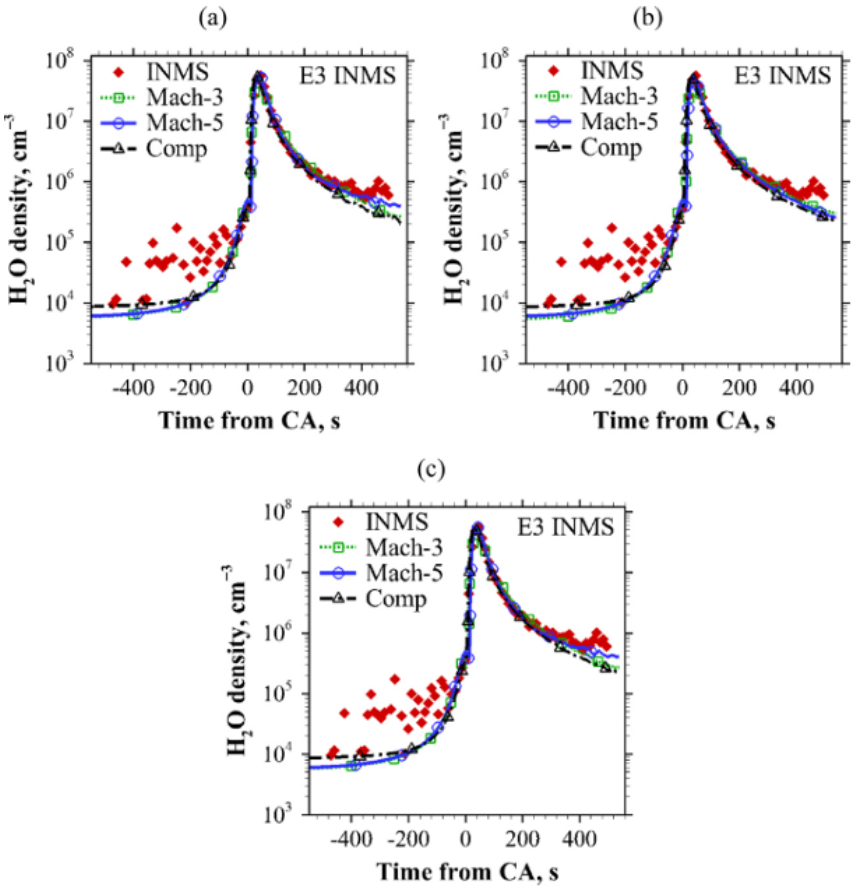

Figure 2.12: H_2O density profiles in comparison to E3 INMS profile for the different fit cases taken from Yeoh et al. [2017]

2.7. Ice grain modeling

The ice grains observed in the plumes span a wide size range, from nanometer-sized particles to larger micron-sized grains. These grains exhibit differing spatial distributions and velocity profiles, suggesting a dynamic and multifaceted ejection mechanism. Tucker et al. [2015], Postberg et al. [2011] highlighted that smaller grains achieve higher velocities due to greater coupling with the surrounding gas, while larger grains tend to decouple earlier and remain in lower altitudes of the plume. These observations have driven efforts to model the underlying physical mechanisms governing ice grain behavior. Figure 2.13 shows the results for an axisymmetric nozzle geometry (explained in Tucker et al. [2015]) with a vent exit radius of 20 m. The plots also show the different particle sizes used for the model and how their exit speeds vary with the inlet position and many other results.

The formation of ice grains in Enceladus' plumes involves complex physical and chemical processes, including condensation, sublimation, and interactions with subsurface materials. One of the primary mechanisms for ice grain formation is condensation from water vapor within the plume. In the high-pressure subsurface environment, water vapor condenses onto nucleation sites, forming grains that are subsequently entrained in the flow. Nakajima and Ingersoll [2016] proposed a controlled boiling model, where water vapor and ice grains are ejected from a liquid reservoir through narrow fractures. Their simulations showed that the condensation rate and resulting grain size are highly sensitive to the depth and width of the cracks.

Tucker et al. [2015] highlighted that the temperature and pressure conditions near the vent play a crucial role in determining the size distribution of grains. Smaller grains tend to form closer to the vent where supersaturation levels are highest, while larger grains form in regions with lower supersaturation. In addition to condensation, ice grains can form through the sublimation of pre-existing ice in the subsurface. This mechanism is particularly relevant in regions where heat flux is high, such as near the tiger stripes. Models by Ingersoll and Pankine [2010] suggested that sublimation-driven plumes are less likely to produce salt-rich grains, as observed in Cassini data, implying that this mechanism may be secondary to condensation from liquid reservoirs. Postberg et al. [2011] provided compelling evidence for the presence of salt-rich grains in the plumes, suggesting that these grains originate from subsurface spray mechanisms. Their analysis showed that the composition of these grains closely matches that of a liquid water reservoir in contact with Enceladus' rocky core. The spray mechanism involves the ejection of liquid droplets, which rapidly freeze upon reaching the vent.

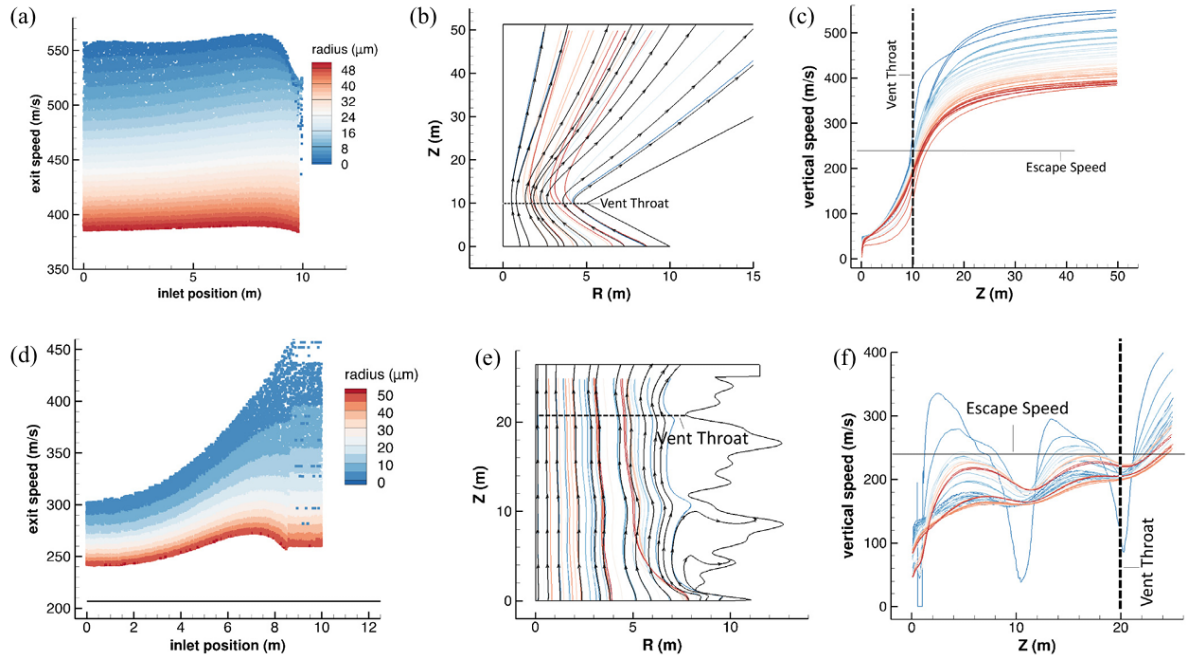

Figure 2.13: Grain results for an axisymmetric nozzle vent with an exit radius of 20m (a-c). (a and d) Terminal grain speeds (colored shapes) versus inlet position. Grain trajectories (b and e) and vertical speed (c and f) of grains versus vent height [Tucker et al., 2015]

The coupling between gas and ice grains is a critical factor influencing grain dynamics. Smaller grains, due to their higher surface area-to-mass ratio, experience stronger drag forces and are accelerated to higher velocities. In contrast, larger grains decouple from the gas flow earlier and retain lower velocities. Li et al. [2013] modeled the velocity distribution of grains in the near-vent region, showing that gas-grain interactions are most intense within the first few meters. Their simulations revealed that the grain velocity profile becomes stratified with altitude, reflecting the size-dependent acceleration of grains. The size-dependent behavior of ice grains is further influenced by the geometry of the vent. Narrower vents produce higher gas velocities, resulting in stronger drag forces and greater acceleration of small grains. Tucker et al. [2015] demonstrated that the terminal velocity of grains is highly sensitive to the vent geometry and gas flow properties, with narrower vents favoring the ejection of smaller, faster grains. The spatial distribution of ice grains within the plume is governed by their initial ejection conditions and subsequent interactions with the gas flow. Postberg et al. [2011] noted a stratification of grain composition within the plume, with salt-rich grains dominating near the vent and salt-poor grains becoming more prevalent at higher altitudes.

3

Methodology

The models discussed in chapter 2 provide a foundation for understanding the dynamics of Enceladus' plumes, from subsurface channel transport to far-field plume expansion. Building on these insights, chapter 3 outlines the methodology employed to simulate plume behavior using numerical techniques. This chapter begins by discussing the initial conditions adopted from existing models explained in the previous chapter, ensuring consistency with observed and theoretical insights. The modeling framework will be introduced next, detailing the capabilities and roles of OpenFOAM and DSMC in capturing the continuum and rarefied flow regimes, respectively. This is followed by the solver that will be used for the thesis, i.e., dsmcFOAM.

With all the different models discussed in the previous chapter, with each model providing a different set of parameters for the vent geometry and the physical conditions of the plumes. However, to answer the research questions discussed in chapter 4, the parameters used in the models of Yeoh et al. [2015, 2017], Tucker et al. [2015], Mahieux et al. [2019] and Nakajima and Ingersoll [2016] will provide the initial conditions for the numerical simulation using OpenFOAM.

Yeoh et al. [2015] is a cornerstone study that uses DSMC methods to model the plume dynamics comprehensively. This method captures the transition of the plume from a dense, collisional regime near the vent to a free-molecular regime at higher altitudes. This transition is crucial for understanding the acceleration of the plume, as the rapid expansion into the vacuum reduces gas density and allows ice grains to decouple from the gas flow. The work also provides detailed insights into the physical mechanisms that drive plume acceleration, highlighting the role of pressure, temperature, and vent geometry in shaping the plume's behavior. Specifically, the paper shows that the initial conditions at the vent, such as Mach numbers (Mach-3 and Mach-5) and the triple-point conditions of water (273 K and 611 Pa), play a vital role in determining the velocity distribution of the ejected material [Yeoh et al., 2015]. It also demonstrates how vent conditions influence the nucleation of ice grains by providing the thermodynamic environment necessary for phase change and condensation. The high temperatures and pressures near the vent enable rapid nucleation, while the subsequent expansion and cooling promote grain growth. The altitude-dependent modeling reveals how the rarefaction of the gas phase and the resulting turbulence affect the growth rates and size distribution of the ice grains. By tracking the interaction between gas molecules and grains as the plume ascends, the paper highlights the importance of collisional processes in shaping the final size distributions observed in space [Yeoh et al., 2015].

Yeoh et al. [2017] bridges the gap between theoretical models and observational data. It aligns the outputs of the DSMC simulation with Cassini's INMS and UVIS data providing empirical validation of numerical models. This allows for a detailed analysis of how well the simulations replicate the observed acceleration of the plume. The paper emphasizes the role of high Mach numbers at vent exits, demonstrating that supersonic flow conditions (>Mach 5) drive significant acceleration of the gas and grain phases [Yeoh et al., 2017]. This also explains how the interaction between gas dynamics and vent geometry influences the spatial evolution of grain sizes within the plume. Furthermore, the use of Cassini

data to determine water vapor production rates—ranging from 400 to 900 kg/s depending on the flyby (E3, E5, and E7)—provides critical insights into the variability of vent activity [Yeoh et al., 2017]. This variability is directly tied to sub-question 5, as it reflects the influence of the tiger stripe crevasses on the plume's properties.

Tucker et al. [2015] offers a focused analysis of how vent geometry influences gas flow and grain acceleration. It demonstrates that subsurface conditions, such as pressure (318 Pa) and temperature (227.4 K), are crucial for shaping the behavior of the plume [Tucker et al., 2015]. The paper explores the connection between vent geometry and nucleation rates of ice grains, as well as the implications of grain size distributions for understanding tiger stripe crevasses. The study highlights the importance of drag forces on grain trajectories, showing that micron-sized grains are influenced by gas velocities of 300–500 m/s near the vents [Tucker et al., 2015]. These findings are instrumental in explaining how turbulence and mixing impact grain growth and distribution. Moreover, the paper's emphasis on comparing drag coefficients for different vent geometries reveals how gas-grain interactions vary spatially within the plume.

Mahieux et al. [2019] takes a systematic approach to evaluate the effects of various vent parameters, such as vent radius, water vapor and ice exit speeds, and the ice-to-vapor mass ratio, on plume dynamics. This study provides an understanding of how these parameters influence the acceleration and distribution of plume material. The parametric analysis sheds light on how vent exit conditions drive the initial acceleration of the plume, making it a crucial piece of the puzzle.The study also quantifies how cooling rates and mixing efficiencies affect ice grain growth and final size distributions [Mahieux et al., 2019]. By defining polynomial approximations for the field parameters at altitudes of 10 km, the paper offers valuable insights into the transition from dense, collisional flow near the surface to free-molecular flow at higher altitudes.

Nakajima and Ingersoll [2016] focuses on the thermodynamic processes driving the plume emissions from narrow cracks in the tiger stripes. The study models vapor-driven jets emerging from subsurface liquid reservoirs and investigates how crack width (0.05–0.075 m) and depth influence the vapor and ice particle production rates. This paper is particularly relevant as it links the characteristics of the tiger stripe crevasses to the observed grain size distributions and dynamics. The authors propose a "controlled boiling mechanism," where the back pressure of the flow regulates the evaporation rate, ensuring that the plume remains active while avoiding complete depletion of the subsurface reservoir. Moreover, the paper highlights how latent heat release and condensation onto the icy walls of the vents contribute to the overall energy balance, providing a thermodynamic perspective that enriches the discussion of plume dynamics [Nakajima and Ingersoll, 2016].

Finally, Dhariwal et al. [2012] offers a detailed analysis of near-field dynamics, emphasizing the behavior of water vapor and ice grains as they emerge from subsurface reservoirs through narrow vent channels. The paper uses a collision-limiter condensation model, which takes into account the interactions between gas molecules and ice grains in a rarefied flow regime. This method captures the transition from dense, collisional flow near the vents to free-molecular flow at higher altitudes, where the density of the plume decreases significantly. Dhariwal et al. [2012] also highlights he role of temperature gradients and cooling rates in shaping the dynamics of the plume. As water vapor cools rapidly upon expansion, it condenses onto existing grains, promoting their growth. The collision-limiter model reveals how turbulent mixing near the vent enhances these processes, leading to a distribution of grain sizes that evolve with altitude. The influence of vent geometry is also explored as discussed in section 2.5, showing the variations in throat width and channel shape affect the flow field, grain growth rates, and the overall dynamics of the plume. These characteristics are linked to the tiger stripe fractures, and providing valuable insights into the subsurface conditions that drive plume activity. Li et al. [2013] extends this understanding by employing the DSMC method to model the near-field dynamics of Enceladus' plumes. This paper focuses on the coupling between gas and grain phases, exploring how subsurface conditions and vent geometries influence the behavior of the plume as it escapes into space. While the collision limiter model used in the two papers is for subsurface and near-field modeling, this thesis will use the approach to model and better understand the nucleation and growth of particles in the plumes of Enceladus.

Collectively, these papers offer a comprehensive framework for understanding the behavior of Enceladus' plumes. One of the main observations when studying the above models is that the authors

compared their results to the E3, E5 and E7 flybys of the Cassini mission. These flybys were at a relatively higher altitude when compared to the later flybys of E14, E17 and E18 which were much closer to the surface of Enceladus. A summary of the models has been represented in Table 3.1 and the initial conditions discussed in the above papers has been shown in Table 3.2.

Table 3.1: Summary of the models with their observations and results

Research Paper	Models	Observations	Results
On understanding the physics of the Enceladus south polar plume via numerical simulation [Yeoh et al., 2015]	DSMC method with two-phase coupling (gas and grains), studying transitions from continuum to free-molecular flow.	- Plume flow transitions from collisional near the vents to free-molecular at higher altitudes. - Micron-sized grains decouple from the gas within 10 vent diameters, while nanometer-sized grains remain coupled to the gas for longer distances. - Collisions at the vent affect gas molecular speeds far from the surface.	- Supersonic flow near the vent is driven by temperature drops rather than speed increases. - Large vent sizes (several tens of meters) are required to produce micron-sized grains observed by Cassini. - Smaller grains spread widely while larger grains maintain collimation, forming distinct beams.
Constraining the Enceladus plume using numerical simulation and Cassini data [Yeoh et al., 2017]	Multi-scale models combining DSMC near-field results with free-molecular planetary-scale models.	- Cassini flybys recorded variable H2O production rates, ranging from 400 to 900 kg/s. - Distributed sources (Tiger Stripes) contribute more significantly than individual jets to the overall plume. - Local temporal variability in specific regions (e.g., Cairo stripe).	- Distributed sources dominate due to the uniformity of flow over large areas, while narrow jets represent localized, high-velocity outputs. - High Mach numbers (>5) at vents suggest deep underground sources, consistent with evaporation from liquid reservoirs or sublimation of icy reservoirs. - Spreading angles for grains are influenced by subsurface mechanisms, not solely by surface conditions.

Research Paper	Models	Observations	Results
2D models of gas flow and ice grain acceleration in Enceladus' vents using DSMC methods [Tucker et al., 2015]	2D DSMC models investigating the effects of vent geometry on gas and grain dynamics.	- Gas velocities at the vent reach 300–1000 m/s, significantly higher than the escape speed (240 m/s). - Micron-sized ice grains are ejected near escape velocity, while larger grains fail to reach high altitudes. - Observed plume stratification includes salt-rich grains closer to the surface and smaller, salt-poor grains at higher altitudes.	- Narrow vent geometries with dense gas flow enhance micron-sized grain acceleration. - Grain acceleration depends on drag forces, which vary with vent density and geometry. - Gas dynamics dictate the plume's vertical and horizontal structures, affecting the grain size distribution and escape potential.
Parametric study of water vapor and ice particle plumes using DSMC [Mahieux et al., 2019]	DSMC simulations focusing on parametric variations in vent radius, mass flow, and particle properties.	- Near-surface flow dynamics exhibit rapid density and temperature changes. - Vent parameters, including exit velocity, angle, and flow temperature, strongly influence the collisionless flow at higher altitudes. - Cross-correlation between water vapor and ice particle exit speeds observed.	- Polynomial fits enable efficient prediction of plume properties, reducing the need for computationally expensive DSMC simulations for each scenario. - Vent exit angle plays a significant role in determining lateral spreading of the plume. - The approach provides generalized tools for studying plume dynamics on other icy bodies (e.g., Europa or Ceres).
Controlled boiling on Enceladus: Model of the vapor-driven jets [Nakajima and Ingersoll, 2016]	Fluid dynamics of vapor flow in cracks, coupled with thermal interactions and latent heat effects.	- Tidal stresses control the width of the tiger stripe fractures, influencing vapor flow rates. - Observed heat flow along tiger stripes correlates with latent heat release due to condensation on ice walls. - Plume mass flow rate and ice-to-vapor ratios vary significantly with crack width and orbital position (e.g., apocenter).	- Optimal crack widths of 0.05–0.075 m are necessary to replicate observed vapor flow rates. - Crack tapering near the surface helps explain observed vapor and particle distributions. - Thermal energy from latent heat of condensation contributes to observed hot spots near tiger stripes, reinforcing the link between plume activity and crack geometry. - Ice-to-vapor ratios reflect conditions at the liquid-vapor interface, indicating active boiling processes in subsurface reservoirs.

Research Paper	Models	Observations	Results
Modeling and Simulation of Near-field Enceladus Plumes from Tiger Stripe Fractures using a Collision-limiter Condensation Model [Dhariwal et al., 2012]	Equilibrium Direct Simulation Monte Carlo (eDSMC) for gas dynamics, combined with an overlay technique for ice grain properties (number density and radius).	- Gas flows were modeled as continuum and inviscid within a 45 m-long subsurface channel. - Ice grain trajectories and growth were computed separately using gas flow data. - Two vent geometries: double-throated and conical nozzles were studied.	- Subsurface jet sources are consistent with boiling liquid conditions. - Double-throated vents showed better control over grain ejection. - Supersaturation near the vent led to rapid ice grain condensation, while sublimation dominated at higher altitudes.
DSMC Simulation of Near-field Enceladus Plumes from Tiger Stripe Fractures [Li et al., 2013]	eDSMC for high-pressure gas flows with an additional condensation model for ice grain nucleation, growth, and motion.	- Significant differences between gas and grain velocities, with grains moving slower (60 m/s) than gas (300–500 m/s). - Grain size and velocity depend on vent geometry and gas drag coefficients.	- Vent geometry (e.g., conical vs. double-throated) strongly influences grain size distribution and ejection velocities. - Coupled condensation and sublimation processes dictate grain size evolution in the plume. - Ice-to-vapor mass ratios depend on vent shape and subsurface temperature.

Table 3.2: Summary of the Initial Conditions for Numerical Simulations of Enceladus' Plumes

Research Paper	Parameter	Value
On understanding the physics of the Enceladus south polar plume via numerical simulation [Yeoh et al., 2015]	Vent Mach number	3–5
	Temperature	190–273 K
	Ice/Water Vapor Ratio	0.2–0.7
Constraining the Enceladus plume using numerical simulation and Cassini data [Yeoh et al., 2017]	H_2O Production Rate	400–900 kg/s
	Vent Mach number	>5
	Vent Size	Meters in diameter
2D models of gas flow and ice grain acceleration in Enceladus' vents using DSMC methods [Tucker et al., 2015]	Gas Density	$10^{14} - 10^{20}\,\mathrm{m}^{-3}$
	Gas Velocity	300–1000 m/s
Parametric study of water vapor and water ice particle plumes [Mahieux et al., 2019]	Vent Radius	Meters
	Water Vapor and Ice Grain Speed	Mach 5

Research Paper	Parameter	Value
	Ice Grain Radius	Micron
Controlled boiling on Enceladus: Model of the vapor-driven jets [Nakajima and Ingersoll, 2016]	Crack Width	0.05–0.075 m
	Temperature	273 K
	Vapor Mass Flow Rate	200 kg/s
	Salinity	0.5–2%
Modeling and Simulation of Near-field Enceladus Plumes from Tiger Stripe Fractures [Dhariwal et al., 2012]	Subsurface Channel Length	45 m
	Gas Velocity	300–500 m/s
	Ice Grain Concentration	Low
DSMC Simulation of Near-field Enceladus Plumes from Tiger Stripe Fractures [Li et al., 2013]	Temperature	273 K
	Pressure	611 Pa
	Flow Model	Subsurface boiling, modeled as a nozzle

4

My Thesis

The previous chapters have explained the importance of Enceladus' icy plumes, showing they are a direct sample of a subsurface ocean that might be habitable. Research using data from the Cassini mission has produced detailed models of the plumes' composition and behavior near the moon's surface. However, the review of existing models in Chapter 2 showed a clear research gap. While we have a good understanding of what the plumes are made of, there is no clear agreement on how they behave at higher altitudes. The central unresolved question is whether the plumes continuously accelerate as they expand into the vacuum of space, or if they eventually begin to slow down. This uncertainty exists because most models have focused on the plume's origin and near-field dynamics, leaving their far-field behavior less understood, leading to the following research questions.

MQ: Are the plumes of Enceladus accelerating as they expand above the surface to the spacecraft?

To answer the main research question, this thesis will use the dsmcFOAM solver to create a numerical simulation of a single plume of Enceladus. This model will track the plume's expansion from the dense environment in the near-field region and expand the results to the far-field region. By analyzing the velocity of gas and ice particles throughout this simulated journey and comparing the results to Cassini data, we can determine if the plume is accelerating or decelerating as it moves away from Enceladus.

This thesis is structured around the main research question, which has been broken down into three sub-questions. These three sub-questions will explore the relationship between flow dynamics and particle size, the factors governing growth of ice grain particles, and evaluating and drawing inferences from the numerical simulations to compare the results with the observations made by the Cassini spacecraft.

SQ.1: What is the relationship between plume flow dynamics and the size of the particles of the plume?

This thesis will perform a comparative study using the dsmcFOAM solver. One set of simulations will model the plume composed only of water gas particles, while the other set will also include the presence of ice grain particles in the flow. By comparing the two sets of results through various flow properties (like velocity, pressure, and temperature) the impact that the presence of ice grain particles have on the dynamics of the flow can be understood.

SQ.2: What are the key factors influencing the growth of ice grain particles in Enceladus' plumes, and how do vent conditions influence this process?

A post-processing model will be developed to analyze the results from the dsmcFOAM simulations from SQ.1. This model will calculate the growth of individual ice grains based on various factors (like sticking coefficient, velocity, number density, temperature, residence time) in the plume. By running simulations with different initial vent conditions, it can determined how parameters like exit velocity and temperature influence the final size distribution of the ice grain particles.

SQ.3: How do numerical simulations of flow properties compare with the observations made by the Cassini Spacecraft?

The simulation results will be compared with observational data from the Cassini spacecraft. The simulated gas and particle density fields will be used to generate synthetic occultation profiles, which will be used to understand the occultation observations made by the spacecraft. These simulated profiles will then be compared to the actual stellar occultation data recorded by Cassini's UVIS instrument, providing a clear method to predict the flow properties of the plumes of Enceladus.

4.1. Modeling Framework

Now that all the model parameters have been discussed in detail, this section will discuss the two modeling frameworks that will be used for this thesis, DSMC and OpenFOAM.

4.1.1. DSMC

DSMC methodologies are instrumental for modeling the rarefied, far-field dynamics of Enceladus' plumes, capturing molecular-level behaviors beyond traditional continuum assumptions. These simulations provide insights into:

- Transition Regimes: DSMC captures the shift from collisional to free-molecular flow, elucidating plume behavior at higher altitudes [Tenishev et al., 2010, Meier et al., 2015]
- Ice Grain Trajectories: This method models grain decoupling from carrier gas, clarifying spatial distribution and dispersion profiles [Yeoh et al., 2017, Mahieux et al., 2019]
- Rarefied Gas Phenomena: DSMC effectively simulates cooling, condensation, and stratification, enhancing understanding of far-field plume structures [Mahieux et al., 2019, Dhariwal et al., 2012]

4.1.2. OpenFOAM

OpenFOAM (Open-source Field Operation and Manipulation) is a framework for developing application executables that use packaged functionality contained within a collection of over 100 C++ libraries [Jasak, 2009]. Around 200 pre-built applications from two different categories—utilities and solvers—are included with OpenFOAM. It facilitates the modeling of complex multiphase flows and gas-particle interactions. Its primary advantages include:

- Customizable Solvers: OpenFOAM supports precise simulations of vent geometries and their impact on plume expansion
- Phase Transition Representation: It integrates mechanisms like nucleation and condensation, crucial for understanding plume composition
- Turbulence Modeling: The platform effectively resolves turbulence and mixing dynamics in the near-field region, enhancing the interpretation of initial plume characteristics

4.2. Simulation Setup

To get the best of both world, OpenFOAM has a dedicated specialized computational solver within its framework known as *dsmcFOAM* explicitly designed for DSMC methods. By leveraging OpenFOAM's modular and scalable infrastructure, dsmcFOAM facilitates the exploration of intricate non-equilibrium effects critical to understanding rarefied flow environments.

4.2.1. Functionality

dsmcFOAM's advanced capabilities are particularly well-suited for studying the rarefied dynamics of Enceladus' plumes, providing detailed insights into their physical and chemical characteristics.

1. Rarefied Flow Modeling
   - Accurately captures the transition from continuum-like subsurface conditions to free-molecular flow in vacuum conditions.
   - Models the ejection of water vapor and ice grains from Enceladus' tiger stripes, effectively replicating observed plume behavior.

2. Collision Dynamics
   - Simulates interactions among water molecules, ice grains, and trace gases, elucidating nucleation processes and particle growth mechanisms.
   - Accounts for energy transfer during collisions, revealing velocity and temperature distribution patterns critical to understanding plume acceleration.

3. Non-Equilibrium Phenomena
   - Analyzes temperature anisotropies, velocity gradients, and other non-equilibrium characteristics within the plumes.
   - Investigates underlying mechanisms driving plume evolution, including subsurface conditions and vent geometries.

4. Multi-Species Interaction
   - Resolves complex chemical and physical interactions between water vapor, salts, and organic compounds within the plume.
   - Predicts compositional profiles and helps interpret mass spectrometry and other observational data.

4.2.2. dsmcFOAM Workflow

For a general dsmcFOAM simulation, first, the simulations particles are initiated on the grid in such a way that mean velocity, pressure, temperature respect a user-defined values. Then and until the end of the simulation, the next step are repeated [Airiau, 2022]:

1. Ballistic movement, the position of each particle is updated:

$$r_i(t + \Delta t) = r_i(t) + \Delta t u_i(t) \tag{4.1}$$

2. Particles indexation, need to know in what cell they are.
3. Performing collision in a stochastic manner. Velocities (and other quantities) of the particles involved in a collision are updated but their position remain unchanged
4. Sampling quantities (density, velocity, temperature, etc.).

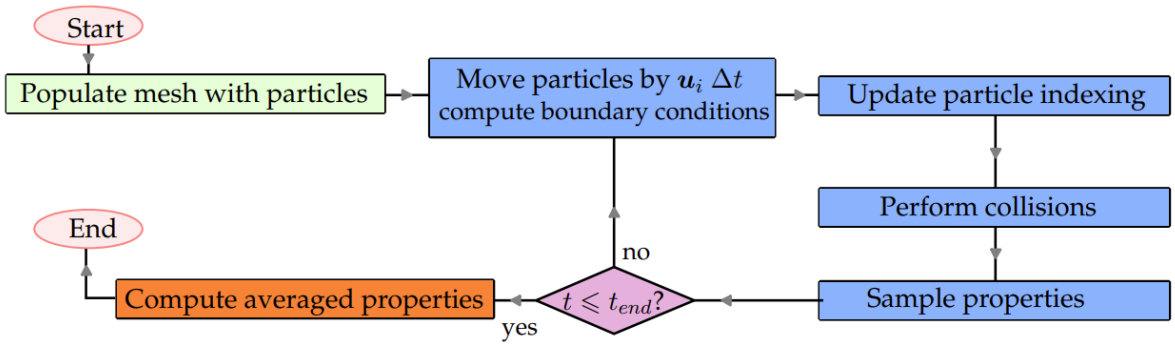

Figure 4.1: General workflow of dsmcFOAM [Scanlon et al., 2010]

5

OpenFOAM Set-Up

OpenFOAM provides a large database of tutorials and test cases for each of the different solvers available when installed. dsmcFoam, introduced in section 4.2, provided a brief overview about the dsmcFoam solver which will be used for this thesis. This chapter will provide a better understanding of the solver and its intricacies. It starts by detailing the baseline architecture of OpenFOAM and then detail into the test cases available for the solver. The test case model is then modified to validate the results obtained in Yeoh et al. [2015] which is then expanded to the free molecular flow region.

5.1. OpenFOAM Architecture

OpenFOAM uses a standard case structure for all its solvers. Each case consists of three main directories, '0', 'constant' and 'system'. The '0' folder is the initial conditions folder (also known as the time directory folder) which contains all the boundary conditions for the simulation with separate files for conditions like velocity, temperature, pressure and other boundary conditions depending upon the solver requirements. The data can be: either, initial values and boundary conditions that the user must specify to define the problem; or, results written to file by OpenFOAM. The 'constant' folder contains a full description of the mesh used by the case for the simulation under the 'polyMesh' subdirectory. It also contains other details about the physical properties of the case depending upon the application. For example, for a dsmcFoam case, the 'dsmcProperties' file contains the collisional models, wall interaction models and other physical models that will be used by the solver. The 'system' folder contains files with the solution procedure of the solver. Every OpenFOAM case contains three files - 'controlDict', 'fvSchemes' and 'fvSolution' - these files run the simulation parameters. A brief overview of the OpenFOAM case architecture for the dsmcFoam solver that will be used for this thesis has been shown in Figure 5.1 and all the directories, subdirectories and files have been discussed in detail in the subsequent sections in this chapter.

5.1.1. Time '0' directory

As shown in Figure 5.1, the dsmcFoam solver contains the following files [Greenshields, 2024]:

1. **boundaryU, boundaryT:** The wall and free stream conditions at the boundary are specified for velocity and temperature with these fields - only the data on the patches is used, the cell data is not. These are the only two fields which supply data to the case.
2. **dsmcRhoN:** The population of dsmc particles in cells is recorded to visualise how well the cell population conditions required for dsmc are met. The boundary conditions are zeroGradient because only cell data is meaningful.
3. **fD, q:** The wall heat flux (q) and force density (fD, i.e. stress vector) is recorded with these fields - only the data on wall patches is relevant, the cell data is not.
4. **iDof, internalE, linearKE, momentum, rhoM, rhoN:** These fields are the densities of extensive quantities in the simulation, i.e. of number, mass, momentum, energy. Cell data is recorded in the internal field and the boundaryField is used to record the data of particles that strike wall patches.

The properties of particles striking wall faces are weighted by 1/(Un*fA), where Un is the normal component of the particle's velocity and fA is the face area. This is done so that when intensive quantities, such as velocity or temperature, are evaluated on the wall the values are correct this allows velocity slip and temperature jump to be evaluated.

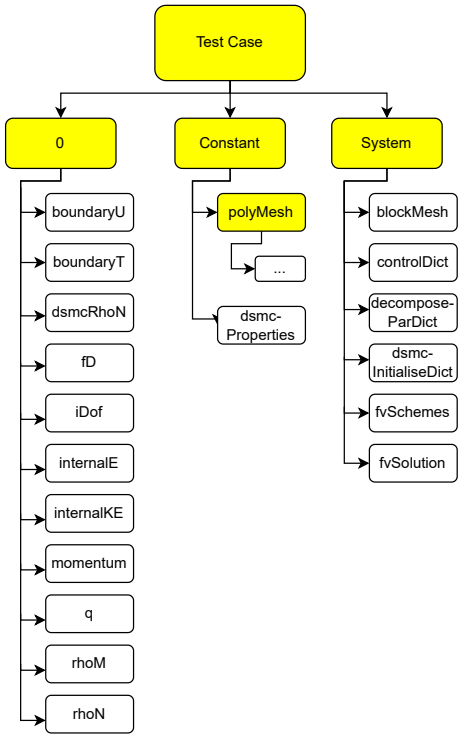

Figure 5.1: OpenFOAM Case Architecture ('Yellow' color box represents a directory and 'white' color box represents a file)

5.1.2. 'constant' directory

As shown in Figure 5.1, this directory contains a subdirectory known as 'polyMesh' which contains the details about the mesh and the computational domain of the simulation. The mesh files have been discussed in detail in Greenshields [2024]. The 'constant' directory also contains an important file for dsmcFoam known as 'dsmcProperties'. This file defines the wall interaction models, collision models, molecular properties and various other parameters which are integral for setting up a DSMC simulation. These parameters have been discussed in Table 5.1.

Table 5.1: Parameters defined in *dsmcProperties*

Name	**Parameter**	**Description**
nEquivalentParticles	Number of equivalent particles	Number of real molecules per DSMC particle
WallInteractionModel	Wall interaction model	Governs particle-wall interactions
BinaryCollisionModel	Collisional model	Controls collisions between the particles
InflowBoundaryModel	Inlfow blundary model	Generates inflow particles with correct distribution
typeIdList	Particle names	List assigning IDs to each species
moleculeProperties	Molecule properties	Physical parameters for each species

nEquivaletntParticles
As explained in Table 5.1, *nEquivaletntParticles* defines the number of real molecules per DSMC particles. This is calculated by:

$$n_p = n_{ppc} N_{cells} = \frac{n_\infty V_{cell}}{n_{ep}} \tag{5.1}$$

Where n_p is the number of simulated DSMC particles, n_{ppc} is the number of DSMC particles per cell (usually 20 DSMC particles per cell), N_{cells} is the number of cells in the computational domain, n_∞ is the number density of the particles, V_{cell} is the total volume of the computational domain and n_{ep} is the number of equivalent DSMC particles defined for the simulation.

BinaryCollisionModel
The *BinaryCollisionModel* defines the collisional model in the simulation. There are 3 different collisional models: Hard Sphere (HS), Variable Hard Sphere (VHS) and Variable Soft Sphere (VSS) models. The HS model is the simplest collisional model which treats the particles as non-deformable, non-rotating spheres with constant diameter and the collisional cross-sectional is independent of the relative collisional speed. The VHS improves on the HS model by varying the effective collisional cross-section with the relative collisional speed.

5.1.3. 'system' directory
The 'system' directory is the most important directory as it sets up the simulation with the convergence criteria, time step, mesh generation (using *blockMeshDict* file) and various other parameters crucial for the simulation. As shown in Figure 5.1, the directory has many files and the function of each file is presented in Table 5.2. The parameters defined in each of the files listed in Table 5.2 have been discussed in detail in the subsequent sections.

Table 5.2: Files listed in *system* directory

File	Description
blockMeshDict	Defines the mesh geometry using blocks, vertices, and boundary patches
controlDict	The master control file for regulating the time settings, output, and solver info
decomposeParDict	Controls domain decomposition for parallel runs
dsmcInitialiseDict	Provides the initial conditions for the particles
fvSchemes	Specifies numerical discretization schemes
fvSolution	Controls the solver and its algorithms

5.2. Simulation Set-up Process
When starting off with OpenFOAM, it is good practice to start off using one of the tutorial cases provided by OpenFOAM as mentioned in Greenshields [2024]. After the test case has been validated using existing literature, the computational domain cam be modified for the use case of this thesis. However, when setting the domain size is significantly large (as was the case with Yeoh et al. [2015] with a computational domain of 25m x 25m), it is recommended to scale down the computational domain and then expand to a larger domain.

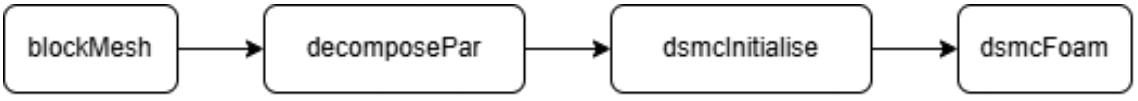

Figure 5.2: *dsmcFoam* simulation set-up process

5.2.1. Running the Simulation

Running an OpenFOAM simulation is quite straightforward for most of its solvers, however, when the domain size is large and the simulations aren't quite simple, it is important to understand what every step of running the simulation does. This process has been illustrated in Figure 5.2. Each part of the process has been explained below.

blockMesh

The 'blockMeshDict' file creates the meshes required for the simulation by a parametric method with grading and curved edges. The file contains the details of the domain geometry and the boundary conditions for the geometry. To generate the mesh from this data, the command *blockMesh* is run which creates a new directory 'polyMesh' under the 'constant' directory. This 'polyMesh' directory consists the mesh data with 'points', 'faces', 'cells' and 'boundary' files.

blockMesh works on the basis of breaking down the domain geometry into a collection of one or more 3D hexahedral blocks. The blocks' edges may be splines, arcs, or straight lines. In order for *blockMesh* to generate the mesh data, the mesh is supposedly specified as a number of cells in each direction of the block. An overview of the 'blockMeshDict' file and its contents are listed in Table 5.3.

Table 5.3: Parameters defined in *blockMeshDict* file

Parameters	**Description**
vertices	List of 3D points defining the corners of the mesh
blocks	Defines the hexahedral mesh blocks using the indices of the vertices
boundary	Defines named patches (e.g., inlet, outlet, walls) for the corresponding faces in the computational domain
mergePatchPairs	Merges common boundary patches during mesh generation

decomposePar

The 'decomposeParDict' file breaks up the computational domain with minimal effort by decomposing the mesh and its fields. They are decomposed based on the parameters specified in the 'decomposeParDict' file. These parameters are discussed in detail in Table 5.4.

Table 5.4: Parameters defined in *decomposeParDict* file

Parameters	**Description**
numberOfSubDomains	Number of partitions for parallel computing
method	Decomposition strategy for parallelization

To decompose the domain, the *deocomposePar* command is executed which generates a set of sub directories, one for each processor, in the case directory. Each directory is named *processorN* where N = 0,1,2,3, ... represents the processor number which contains a time directory giving decomposed field information and a *constant/polyMesh* directory containing the decomposed mesh description.

dsmcInitialise

Before running the solver, the mesh and its computational domain needs to be initialised and populated with DSMC particles. The *dsmcInitialise* command is a pre-processing utility to create initial configurations of these DSMC particles for the given geometries. The parameters defined in the 'dsmcInitialiseDict' are listed in the Table 5.5.

Table 5.5: Parameters defined in *dsmcInitialiseDict* file

Parameters	**Description**
numberDensities	Initial particle number densities per species in m^{-3}
Temperature	Temperature of the flow at the inlet boundary condition
Velocity	Velocity of the flow at the inlet boundary condition

After executing the *dsmcInitialise* command, the output generated is shown in Figure 5.3 which shows the number of DSMC particles inserted in the mesh. Only after this output has been generated and particles have been inserted, the solver (*dsmcFoam*) can be run.

```
Create mesh for time = 0

Initialising dsmc for Time = 0


Constructing constant properties for
    N2
    O2

Initialising particles

Total number of molecules added: 20984


ClockTime = 0 s

End
```

Figure 5.3: Output after executing the *dsmcInitialise* command

dsmcFoam

'dsmcFoam' is the solver and the command *dsmcFoam* starts the solver. The process followed by the solver is shown in Figure 5.4.

```
Create mesh for time = 0


Constructing dsmcCloud
Selecting BinaryCollisionModel LarsenBorgnakkeVariableHardSphere
Selecting WallInteractionModel MaxwellianThermal
Selecting InflowBoundaryModel FreeStream

Constructing constant properties for
    N2
    O2

Starting time loop
```

Figure 5.4: *dsmcFoam* initial process

At every time step of the solver, the values displayed on the terminal window are shown in Figure 5.5.

```
Time = 15.2354s

    Particles inserted             = 0
    Collisions                     = 7267
    Acceptance rate                = 0.002931541034

Cloud name: dsmc
    Number of dsmc particles       = 22457
    Number of molecules            = 4.5520339e+23
    Mass in system                 = 0.0721720631
    Average linear momentum        = (-1.234849209e-24 8.20233005e-24 9.255256954e-27)
    |Average linear momentum|      = 8.294766813e-24
    Average linear kinetic energy  = 2.808980809e-21
    Average internal energy        = 1.10154081e-21
    Average total energy           = 3.910521619e-21

ExecutionTime = 6830.498455 s  ClockTime = 6833 s
```

Figure 5.5: *dsmcFoam* output on the terminal window

The *dsmcFoam* solver, as explained earlier, is controlled by the parameters defined in the 'controlDict' file. The parameters defined in this file is discussed in Table 5.6.

Table 5.6: Parameters defined in *controlDict* file

Parameters	**Description**
application	Specifies the solver to be used
startTime	Start time of the simulation
deltaT	Time step size of the simulation
writeInterval	Time between output writes (in seconds or steps)
writePrecision	Number of decimal places of different values in the output files
adjustTimeStep	Enables dynamic time stepping
functions	Used for post-processing utilities

6

Validation and Verification

With a basic understanding of the parameters and the content of *dsmcFoam*, it is important to simulate different cases to better understand the working and validate *dsmcFoam* so that it can be applied to the conditions representative of Enceladus and it's plumes. For this thesis, 5 cases have been discussed and simulated one of which is an OpenFOAM test case and the other 4 cases are used to validate and verify the results from the existing literature, particularly the results obtained by Yeoh et al. [2015], which have been discussed in detail in the subsequent subsections.

6.1. OpenFOAM test case

To understand the working of the *dsmcFoam*, it is important to run test cases provided by the development team. OpenFOAM provide multiple test cases for each solver to fully understand its working and the dynamics involved. The list of test cases provided can be found in the "~/ opt/ openfoam11/ tutorials/ legacy/ lagrangian/ dsmcFom/" directory. For this thesis, the wedge case has been used as the benchmark test case.

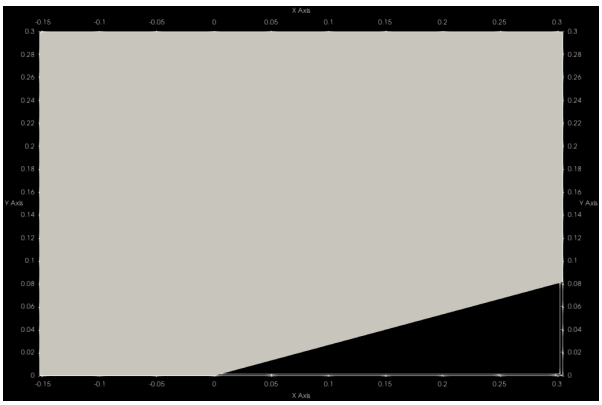

Figure 6.1: Geometry of the wedge case

The test case uses a standard wedge case geometry with a half-wedge angle of 15°as shown in Figure 6.1. With the domain now defined, the mesh was generated with the meshing parameters predefined in the *blockMeshDict* file. The meshed domain is shown in Figure 6.2. While the domain and mesh may look straightforward and simple, the boundary conditions are a slightly different when considering a simple nozzle jet flow. As seen in Figure 6.2, all boundaries are defined as 'flow', i.e., the inlet with a flow velocity of (1736 0 0) m/s and flow temperature of 300 K at all boundaries. The slanted boundary is defined as a no slip wall with a wall temperature of 550 K. These boundary conditions were predefined in the case provided by OpenFOAM and were not modified for this test case.

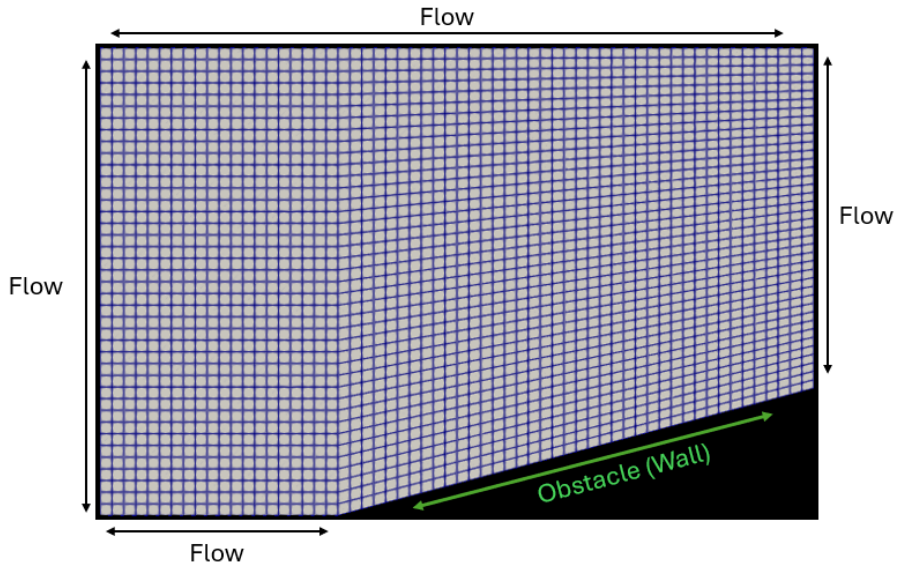

Figure 6.2: Boundary conditions and mesh of the wedge geometry

With the mesh generated and boundary conditions well defined, the initial conditions are defined to simulate the flow. For this test case, the initial conditions have been pre-defined by OpenFOAM and have no been modified and reported in Table 6.1. The calculation of certain parameters like equivalent particles and time step size has been explained in earlier sections.

Table 6.1: Initial conditions of the wedge case

Parameters	**Value**
Number densities	• N_2 - 0.777x10^{20} m^{-3} • O_2 - 0.223x10^{20} m^{-3}
Flow Temperature	300 K
Flow Velocity	(1736 0 0) m/s
Collisional Model	Larsen Borgnakke Variable Hard Sphere Model
Wall interaction model	Maxwellian Thermal Model
Wall Temperature	550 K
Number of equivalent particles	5x10^{12}
Time step (ΔT)	2x10^{-6} seconds

After running the simulations, the results are shown in Figure 6.3 and they were as expected of a typical wedge case with supersonic flow. The results of this case are not important to the scope of this thesis as this case is being used to validate if the solver can provide reliable results. To understand the physics of the flow, please refer to Anderson [1990]. Since the flow over the wedge is supersonic at a Mach number of 5, the results can be validated using standard oblique shock relations from Anderson [1990] which provides a comprehensive discussion about using supersonic flow. These relations provide downstream values of the flow just after the shock which were used to validate the results obtained from the OpenFOAM test case. The results from the test case were obtained from at the nose (at (x,y) = (0 0)) of the wedge geometry and this point has been shown in Figure 6.3a. The results have been tabulated and shown in Table 6.2.

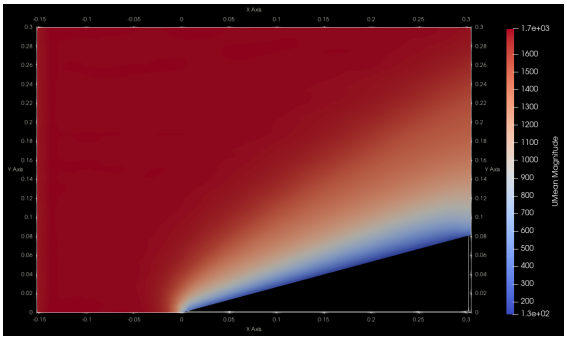

(a) Mean velocity contour for the OpenFOAM test case

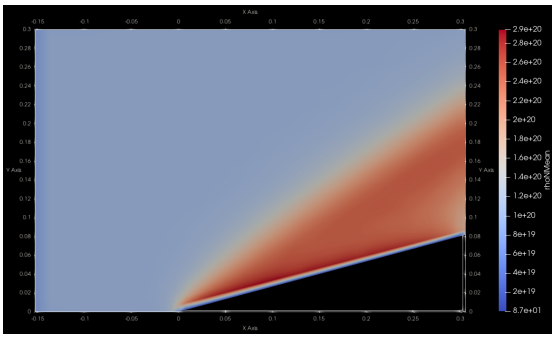

(b) Mean number density contour for the OpenFOAM test case

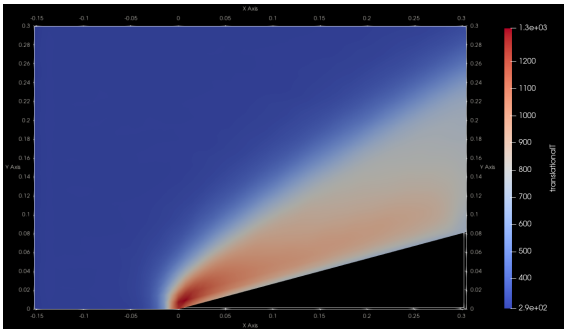

(c) Translational temperature contour for the OpenFOAM test case

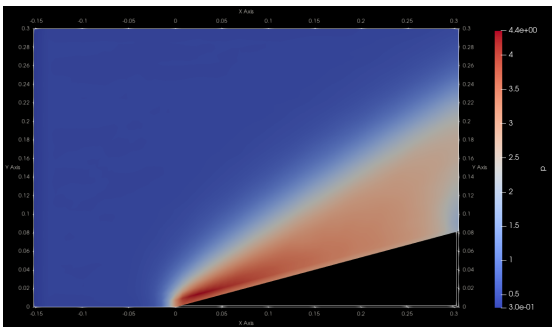

(d) Pressure contour for the OpenFOAM test case

Figure 6.3: Contour plots for various parameters from the OpenFOAM test case

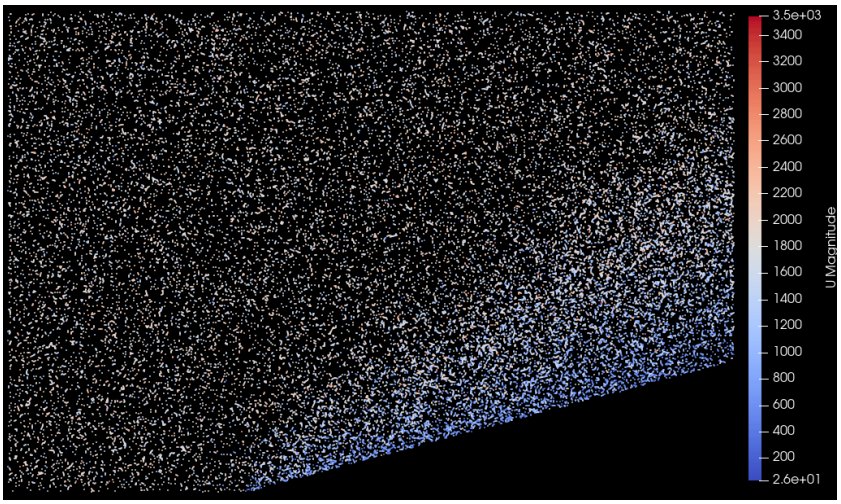

Figure 6.4: Individual particle velocities contour for the OpenFOAM test case

Table 6.2: Validation of the wedge case

Parameters	From simulation	From oblique shock relations
Velocity (m/s)	1582	1617
Pressure (Pa)	1.151	1.986
Temperature (K)	518.3	519.6
Number Density (m^{-3})	2.424x10^{20}	2.745x10^{20}

Table 6.2 shows that the results obtained from the OpenFOAM test case are reliable as they match well with the analytical results obtained using the oblique shock relations. There is still an error between the simulation and the analytical results which is expected due to the sensitivity of the DSMC simulations.

6.2. Expansion of the test case

Now that the working and setup of the OpenFOAM test case has been studied and analyzed, it is now expanded from the test case to a new domain. The new geometry will be similar to the geometry used by Yeoh et al. [2015]. One important thing to note is that the geometry discussed in section 6.1, is nearly 100x smaller than the geometry used by Yeoh et al. [2015]. In Yeoh et al. [2015], the authors start with a computational domain of 25m x 25m. A summary of the cases used for V&V has been discussed in Table 6.3.

Table 6.3: Summary of the *dsmcFoam* cases

Cases	Case Description
Case - 1	• Computational Domain size: 0.25m x 0.25m • Number of Cells: 1760 • Molecules: H_2O
Case - 2	• Computational Domain size: 25m x 25m • Number of Cells: 2750 • Molecules: H_2O
Case - 3	• Computational Domain size: 25m x 25m • Number of Cells: 275000 • Molecules: H_2O
Case - 4	• Computational Domain size: 25m x 25m • Number of Cells: 2750 • Molecules: H_2O, Water Ice

6.2.1. Case 1 - Small Domain, Coarse Mesh

As discussed earlier in Table 6.3, Case 1 has a small computational domain. The main reason for using a small computational domain is to check if the model works for a smaller size of the computational domain. This would save computational time and power before investigating into a computational domain of 25m x 25m as used in Yeoh et al. [2015]. Figure 6.5 shows the domain, the boundary conditions and the mesh of Case 1. The mesh has 1760 cells. One important boundary condition to note is that except the symmetry condition, all other boundaries are defined as inlet. This might be counter intuitive as generally the boundaries other than the inlet and the wall are usually defined as ”zeroGradient” boundary conditions to state that the flow in the direction of the boundary perpendicular is extrapolated from the adjacent internal cells. Initial simulations were performed using this boundary condition which resulted in an under-developed flow but due to the sensitive nature of the DSMC simulations as discussed by Bird [2013], boundary conditions do effect the flow in the computational domain. Hence, considering similar boundary conditions from the test case provided by OpenFOAM discussed in the earlier section in this chapter, the boundary conditions were modified as illustrated in Figure 6.5.

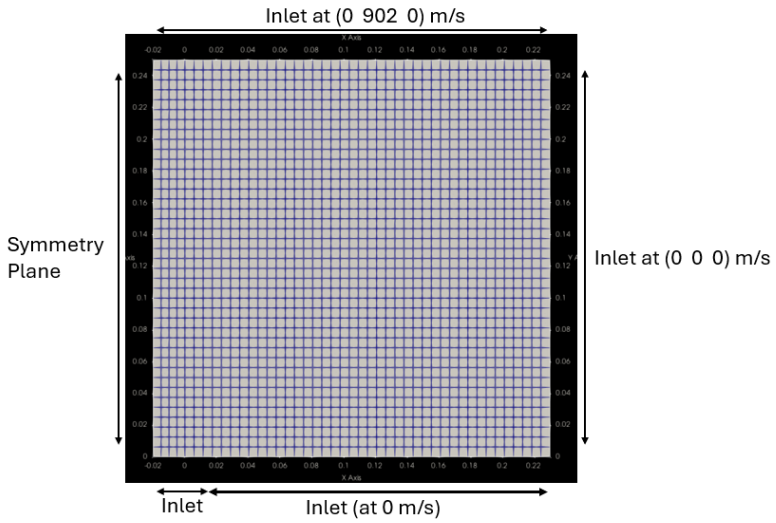

Figure 6.5: Boundary conditions and mesh for Case 1

During the initial runs, as defined in the section 6.1, the flow velocities at the inlet boundaries (except the inlet next to the vent at (0 0 0) m/s) were defined at (0 902 0) m/s but the flow took a long time to reach steady state due to which the right boundary (at x=0.25m) is also defined at (0 0 0) m/s. These results have not been discussed in this thesis due to the extensive computational time required. For this thesis an important assumption is made, i.e., the boundary next to the vent has not been defined as a wall to make the simulation simpler and not involve the particle-wall interactions due to the increased computational complexities. This assumption will be valid for all the cases in this thesis. The initial conditions of Case 1 have been summarized in Table 6.4 as taken from Yeoh et al. [2015].

Table 6.4: Initial conditions for Case 1

Parameters	**Value**
Number densities	H_2O - 1.1417x10^{21} m^{-3}
Flow Temperature	53 K
Flow Velocity	(0 902 0) m/s
Collisional Model	Variable Hard Sphere Model
Number of equivalent particles	2.027x10^{13}
Time step (ΔT)	8.9x10^{-6} seconds

With the boundary conditions and initial conditions established and other conditions set up, the contours of mean velocity, pressure, mean number density, translational velocity and particle velocities and their distribution along the y-axis obtained are shown from Figure 6.6a to Figure 6.10. The distributions have been extracted at y=-0.019m Figure 6.6a shows the mean velocity contour for this case with Figure 6.6b showing its distribution along the y-axis. From the figure it is evident that the mean velocity of the water gas particles decreases by 2.2% as it moves away from the surface. The decrease in mean velocity may be due to the small domain size as there is less room for expansion for the water gas particles to expand and accelerate.

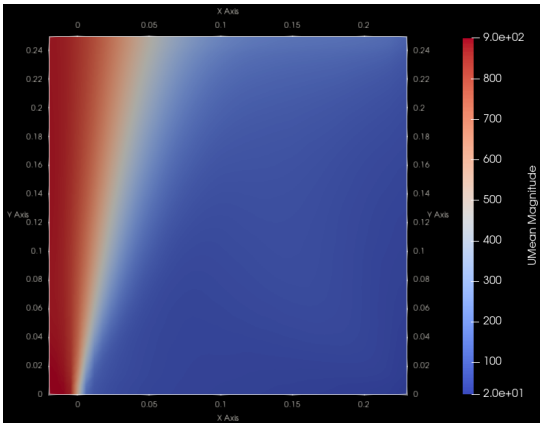

(a) Mean velocity contour for Case 1

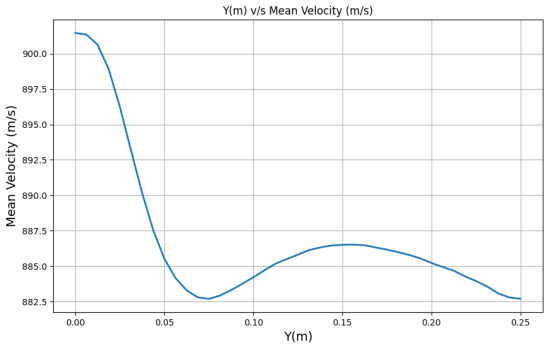

(b) Mean velocity distribution for Case 1

Figure 6.6: Mean velocity details for Case 1

Figure 6.7 shows how the pressure changes as the plumes are ejected from the surface. It can be observed that the pressure increases rapidly for the initial 0.06m to 1.15Pa before gradually declining to less than 0.5Pa at 0.25m. This might be due to multiple reasons like the number density and the mass flow rate of the water gas particles. Figure 6.8b presents that the pressure is maximum (at 0.06 m) in the same region as the mean number density of the particles is also the highest at approximately 1.3x10^{21} m^{-3}. Note that the point at the lowest pressure (at 0.25 m), the mean number density is also the lowest at 0.6x10^{21} m^{-3}. This is also the same for the translational temperature illustrated in Figure 6.9b with the maximum temperature at 0.06 m of 66 K and lowest temperature at 0.25 m of 57 K. This also explains the likely reason for the decline in mean velocity as that the flow expands from a lower pressure region to a higher pressure region which decelerates the flow. This is also indicated by the shock in the translational temperature contour Figure 6.9a as the temperature increases drastically around the flow.

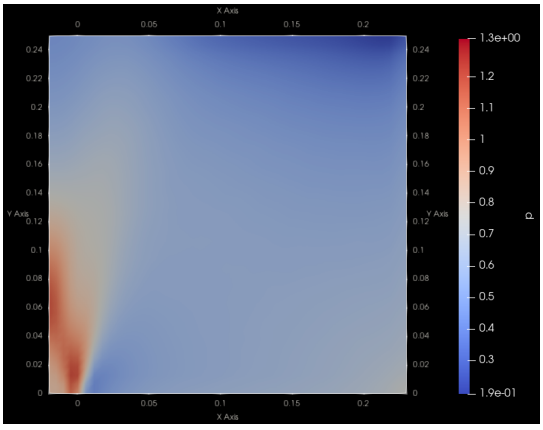

(a) Pressure contour for Case 1

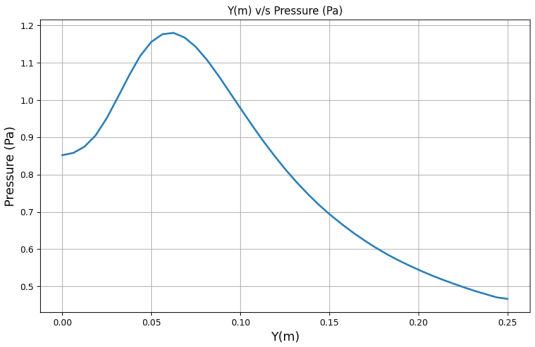

(b) Pressure distribution for Case 1

Figure 6.7: Pressure details for Case 1

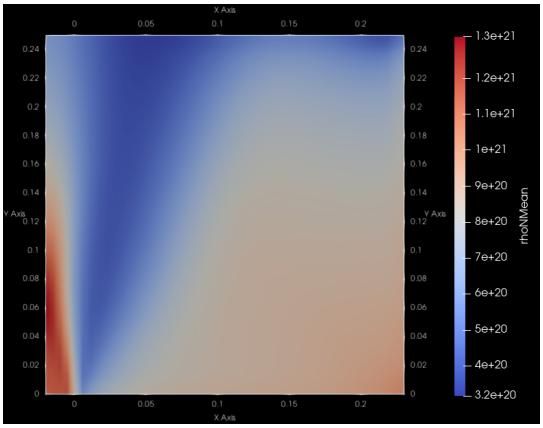

(a) Mean number density contour for Case 1

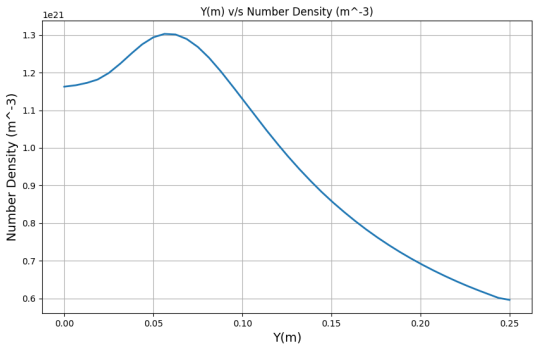

(b) Mean number density distribution for Case 1

Figure 6.8: Translational Temperature details for Case 1

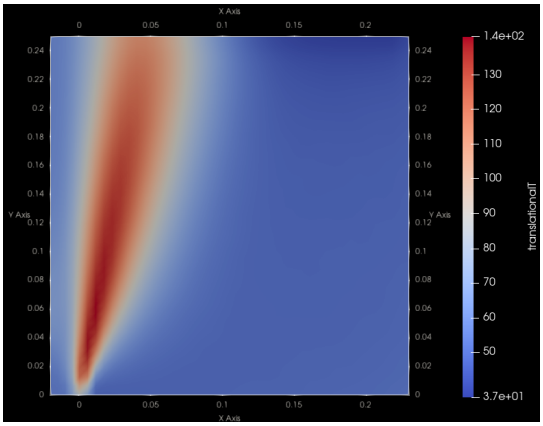

(a) Translational temperature contour for Case 1

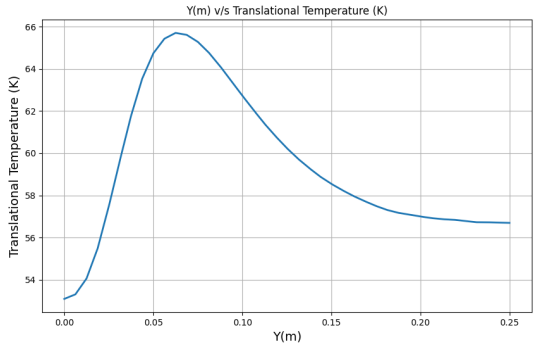

(b) Translational temperature distribution for Case 1

Figure 6.9: Mean Number density details for Case 1

While Figure 6.6a shows the mean velocity contour of the simulation, it is also important to look at the individual velocities of the particles which is illustrated in Figure 6.10. From the contour legend it is visible that the maximum velocity of some of the particles is around the 1300-1400 m/s range with the presence of low velocity particles in the 500-700 m/s range. This shows that some of the particles are accelerating when they exit the surface and expand into outerspace which is contradicting to the mean velocity profile which shows a decline in Figure 6.6b. This contradiction is due to the calculation of mean velocity. The mean velocity is calculated by taking the mean value of the particle velocities in a single cell. In the flow, there will be particles that do not accelerate completely due to momentum loss and/or not being able to expand fully which decreases the mean velocity values, hence the contradiction. However, the size of this computational domain is too small to say this with certainty as the domain size limits the expansion of the water gas particles with the boundary conditions effecting the flow properties. Since the main purpose of Case 1 was to get a baseline simulation running, it can now be expanded to a 25m x 25m computational domain similar to the one used by Yeoh et al. [2015].

Table 6.5: Results summary after Case 1

Case	Results
Case 1	• Computational domain size is 0.25m x 0.25m with only water gas particles • Water gas particle velocity increases • Mean velocity of the flow decreases • Pressure and mean number density decreases • Translational temperature decreases after an initial spike

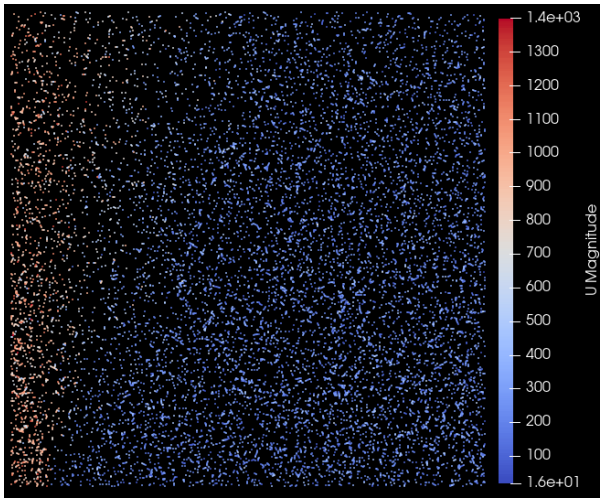

Figure 6.10: Particle velocities contour for Case 1

6.2.2. Case 2 - Large Domain, Coarse Mesh

While Case 1 does produce results, the small domain size restricts the expansion of water gas particles which does not allow the flow to expand completely and it might lead to underprediction of results. The boundary conditions also influences the properties of the flow due to the small domain size. This case expands the computational domain to a size of 25m x 25m keeping the same boundary conditions and initial conditions as Case 1. The number of cells in the mesh increase slightly to 2750 cells due to the larger domain size while also keeping the mesh coarse. The initial conditions have been summarized in Table 6.6.

Table 6.6: Initial conditions for Case 2

Parameters	Value
Number densities	H_2O - 1.1417x10^{21} m^{-3}
Flow Temperature	53 K
Flow Velocity	(0 902 0) m/s
Collisional Model	Variable Hard Sphere Model
Number of equivalent particles	2.027x10^{19}
Time step (ΔT)	5.426x10^{-6} seconds

Figure 6.12a shows the mean velocity contour for this case with Figure 6.12b showing its distribution along the y-axis. Contrary to what was seen in Case 1, Figure 6.12b shows that the mean velocity of the particles increases as the flow develops and expands from the vent. The flow reaches a maximum mean velocity of 905 m/s in the 25m domain. Figure 6.13b shows how the pressure changes as the plumes are ejected from the surface. It can be observed that it reaches a maximum pressure of around 0.84 Pa at around 1.5 m and decreases down to 0.55 Pa at an altitude of 25 m. The mean number

density and the translational temperature of the plumes also show similar behaviors with a maximum of 1.15x10^{21} m^{-3} and 53 K respectively at an altitude of 1.5 m and decreases to 0.86x10^{21} m^{-3} and 47 K respectively at an altitude of 25 m from the vent.

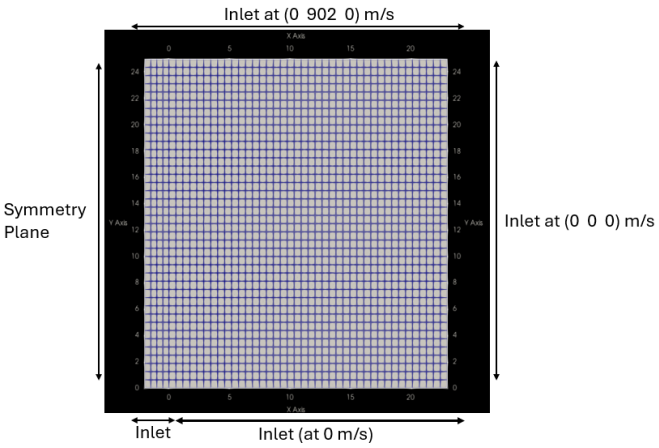

Figure 6.11: Boundary conditions and mesh for Case 2

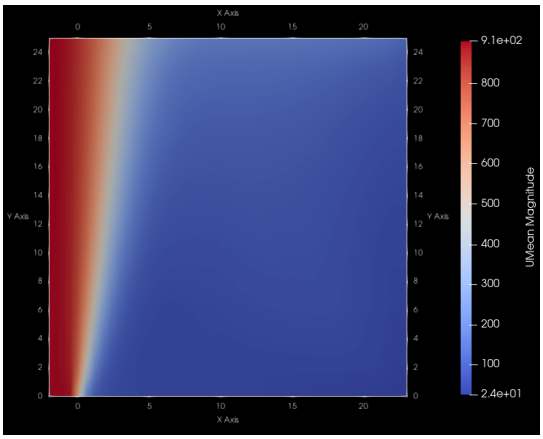

(a) Mean velocity contour for Case 2

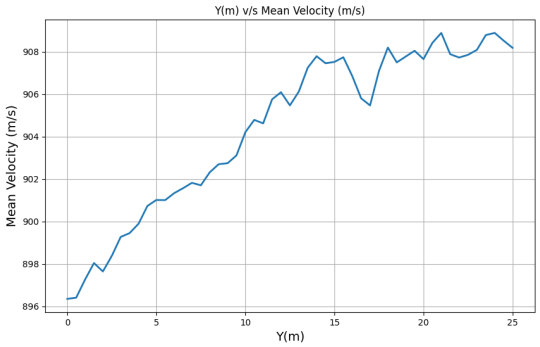

(b) Mean velocity distribution for Case 2

Figure 6.12: Mean velocity details for Case 2

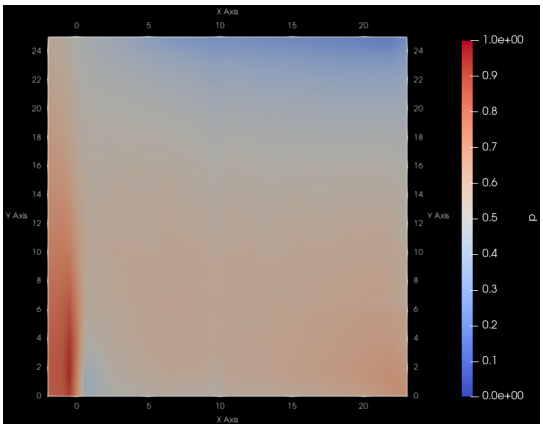

(a) Pressure contour for Case 2

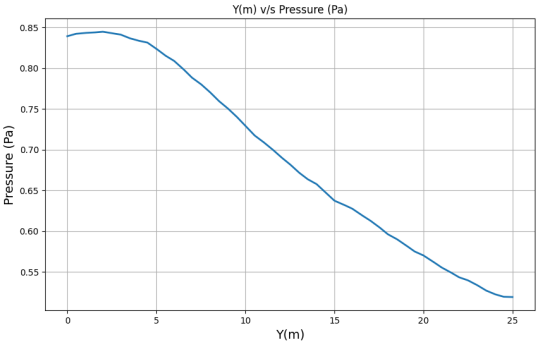

(b) Pressure distribution for Case 2

Figure 6.13: Pressure details for Case 2

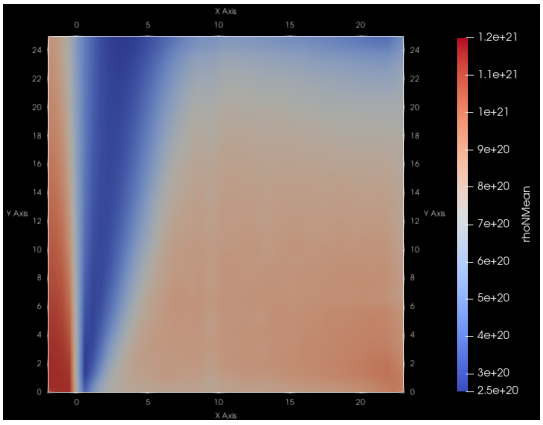

(a) Mean number density contour for Case 2

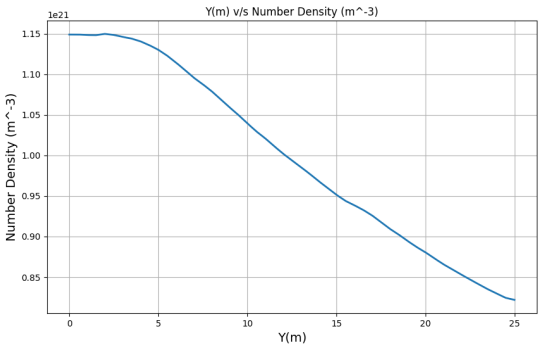

(b) Mean number density distribution for Case 2

Figure 6.14: Mean number density details for Case 2

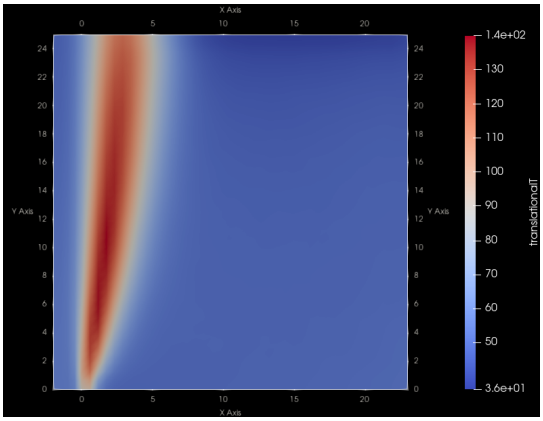

(a) Translational temperature contour for Case 2

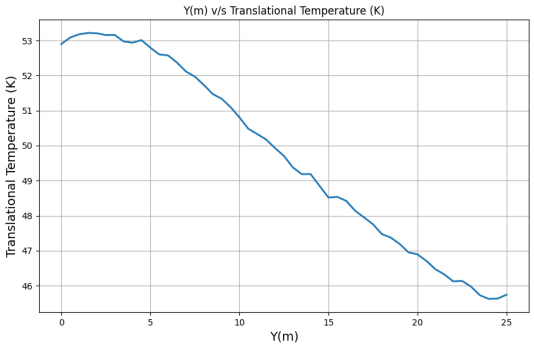

(b) Translational temperature distribution for Case 2

Figure 6.15: Translational temperature details for Case 2

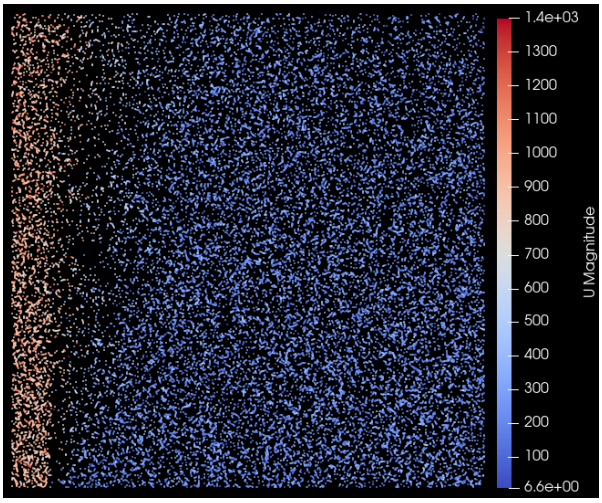

Figure 6.16: Particle velocities contour for Case 2

Looking at the individual velocities of the particles in Figure 6.16, the maximum velocity of the particles within the plumes is in the range of 1300-1400 m/s with a minimum velocity of around 500-700 m/s in the

flow. The individual particle velocities provide an initial indication of the fact that the flow is accelerating after exiting the surface. In this case, Case 2, a coarse mesh was used and in the next case, Case 3, finer mesh will be used to verify whether the results are dependent on the mesh resolution or if mesh convergence is achieved using the current mesh.

Table 6.7: Results summary after Case 2

Case	Results
Case 1	• Computational domain size is 0.25m x 0.25m with only water gas particles • Water gas particle velocity increases • Mean velocity of the flow decreases • Pressure and mean number density decreases • Translational temperature decreases after an initial spike
Case 2	• Computational domain size is 25m x 25m with only water gas particles • Water gas particle velocity increases • Mean flow velocity of the flow increases • Pressure, mean number density and translational temperature all decrease from their initial values

6.2.3. Case 3 - Large Domain, Fine Mesh

With Case 2 providing initial results, it is important to check if the results are effected by the mesh resolution. Bird [2013] states that the cell size of the mesh should be less than the mean free path of the particles and for the computational domain size of 25m x 25m, the mean free path is 0.01m. This case achieves a cell size of 0.045m which is very close to the mean free path (0.01m), thus creating 275000 cells in the mesh and providing a good estimate of the results that can be obtained using Bird [2013]'s condition.

Moving onto the results, the mean velocity contour in Figure 6.18 looks similar to the previous case but the flow is accelerating at higher speeds with a maximum mean velocity of 935 m/s in this domain. This difference in velocity is due to the smaller cell size in this case and when the data is plotted, the mean velocity in this cell is higher when compared to the plot in the coarse mesh. Since the cell size is larger, it covers a larger area and the average velocity of the cell decreases hence the difference in values. Figure 6.18a and Figure 6.18b shows how two different meshes with the same computational domain size have different number of equivalent particles per cell, with the former having a finer mesh and more number of equivalent particles and the latter with a coarser mesh having less number of equivalent particles. The smaller cell size in Case 2 led to artificial smoothening of the results due to which the simulation underpredicts the solution.

Table 6.8: Initial conditions for Case 3

Parameters	Value
Number densities	H_2O - 1.1417x10^{21} m^{-3}
Flow Temperature	53 K
Flow Velocity	(0 902 0) m/s
Collisional Model	Variable Hard Sphere Model
Number of equivalent particles	4.4598x10^{16}
Time step (ΔT)	5.4258x10^{-6} seconds

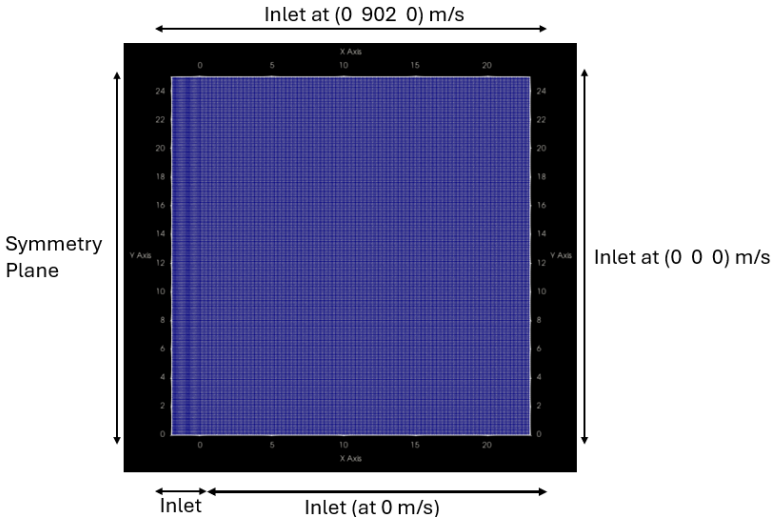

Figure 6.17: Boundary conditions and mesh for Case 3

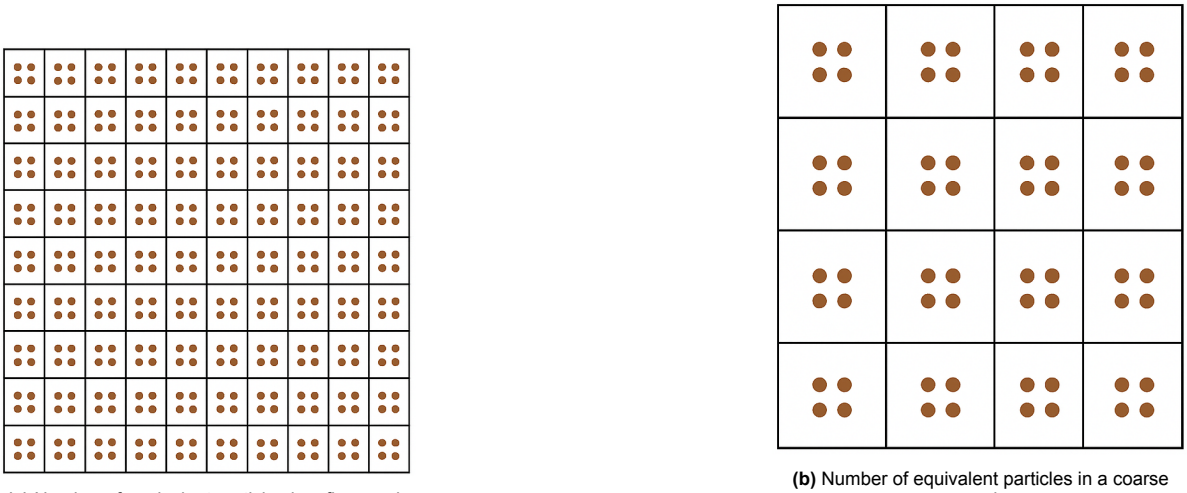

(a) Number of equivalent particles in a fine mesh

(b) Number of equivalent particles in a coarse mesh

Figure 6.18: Number of equivalent particles in a mesh

The difference in the number of particles can be clearly seen when looking at the particle velocities of both the cases in Figure 6.16 and Figure 6.23. Figure 6.23 clearly has significantly more particles but the difference in the particle velocities is not significantly high either as seen in the contours. As was the instance for mean velocity, the pressure contour and plot follows the same behaviour as Case 2 but with one difference, the drop in pressure. The pressure in Case 2 decreases to 0.15 Pa rather than 0.55 Pa that was observed in Case 2. This is similar to the mean number densities and the translational temperature when compared to Case 2. When looking closely, two of the properties (pressure and translational temperature) are dependent on the mean number density of the particles as this influences the number of collisions that occur. Figure 6.21b shows that the number density at the edge of the domain, at 25 m, the mean number density is 0.4x10^{21} m^{-3}, which is less than half the mean number density of Case 2. The explanation for this is similar to the mean velocity difference of the two cases, the size of the cells. Since the cell size is larger, the number of particles in the cell is higher leading to a higher mean number density count and higher pressure as there are more number of particles in that cell. This also increases the chances for collisions to occur which leads to a higher translational temperature.

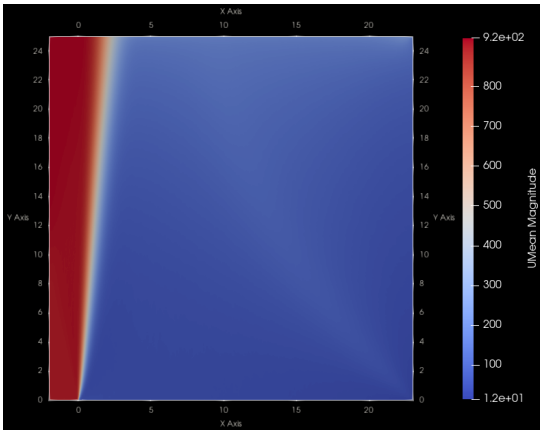

(a) Mean velocity contour for Case 3

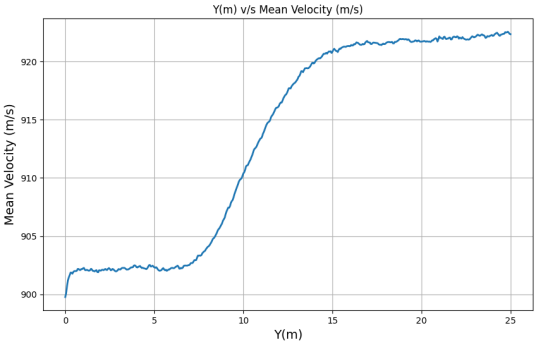

(b) Mean velocity distribution for Case 3

Figure 6.19: Mean velocity details for Case 3

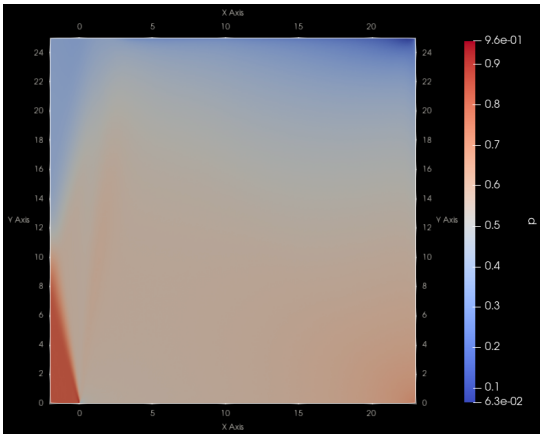

(a) Pressure contour for Case 3

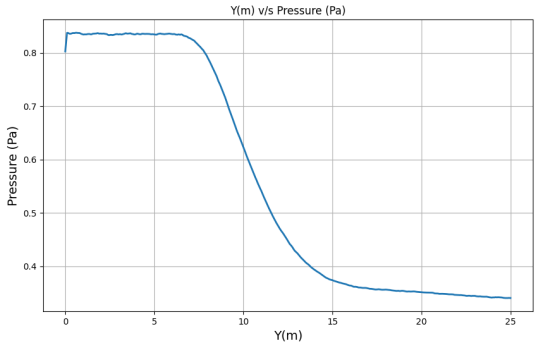

(b) Pressure distribution for Case 3

Figure 6.20: Pressure details for Case 3

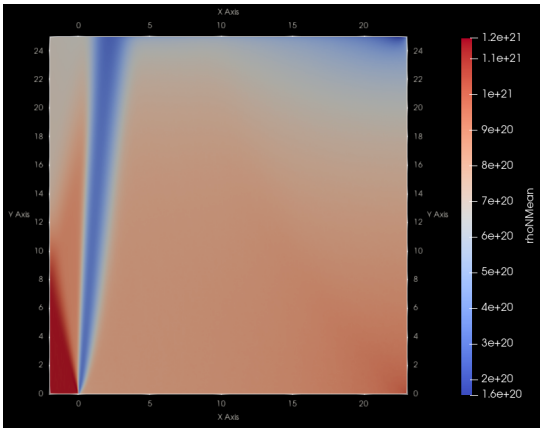

(a) Mean number density contour for Case 3

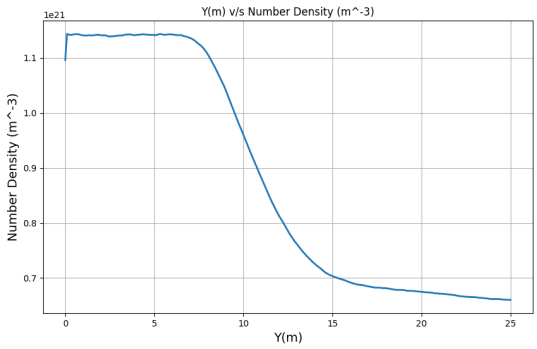

(b) Mean number density distribution for Case 3

Figure 6.21: Mean number density details for Case 3

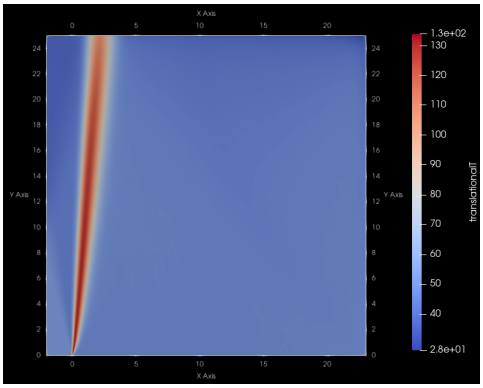

(a) Translational temperature contour for Case 3

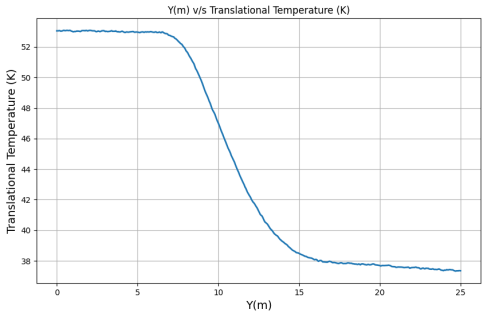

(b) Translational temperature distribution for Case 3

Figure 6.22: Translational temperature details for Case 3

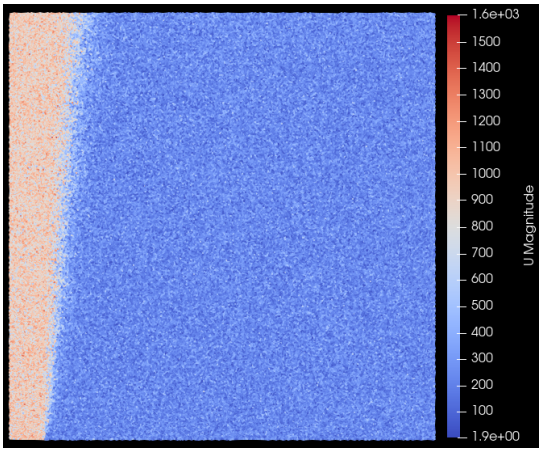

Figure 6.23: Particle velocities contour for Case 3

When comparing the normalized results of the gas translational temperatures obtained by Yeoh et al. [2015] along the centerline of the flow in Figure 6.24b to the normalized results of this case as shown in Figure 6.24a, it can be observed that the two plots follow a similar trend with DSMC simulation results providing a slope of -0.788 compared to the -0.8 obtained by Yeoh et al. [2015].

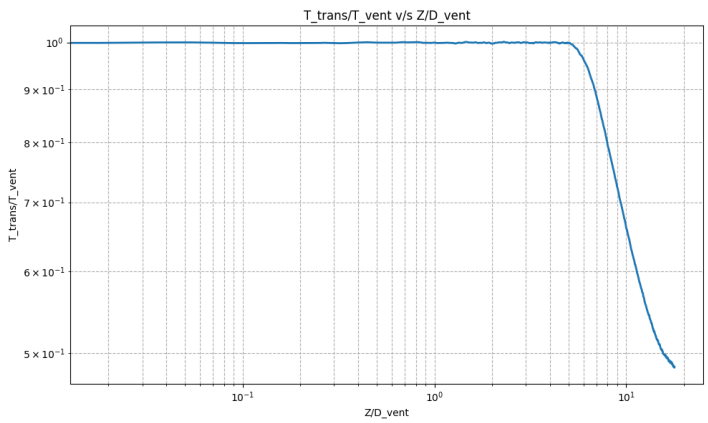

(a) Case 3

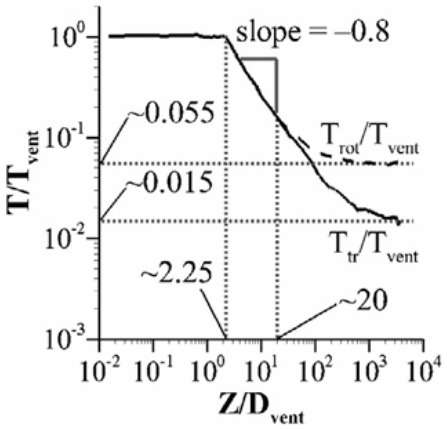

(b) Yeoh et al. [2015]

Figure 6.24: Comparison of the normalized results obtained by Case 3 results and Yeoh et al. [2015]

Table 6.9: Results summary after Case 3

Case	Results
Case 1	• Computational domain size is 0.25m x 0.25m with only water gas particles • Water gas particle velocity increases • Mean velocity of the flow decreases • Pressure and mean number density decreases • Translational temperature decreases after an initial spike
Case 2	• Computational domain size is 25m x 25m with only water gas particles with 2750 cells • Water gas particle velocity increases • Mean flow velocity of the flow increases slightly to 905 m/s • Pressure, mean number density and translational temperature all decrease gradually from their initial values
Case 3	• Computational domain size is 25m x 25m with only water gas particles with 44000 cells • Water gas particle velocity increases • Mean flow velocity of the flow increases significantly to 935 m/s • Pressure, mean number density and translational temperature have a steep decrease from their initial values

6.2.4. Case 4 - Icy Grains

The plumes of Enceladus do not just release water gas, they also have icy grains within the flow. Accurately modeling these icy grains along with water gas is a crucial aspect of this thesis. To model the case with ice grains, same boundary conditions as Case 2 but with slightly modified initial conditions. These modified initial conditions are detailed in Table 6.10.

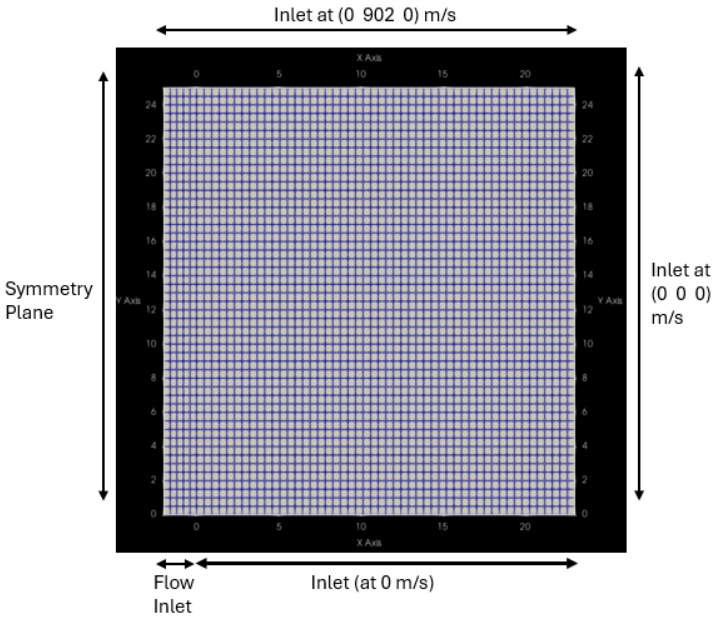

Figure 6.25: Mesh and Boundary Conditions of Case 4

Table 6.10: Initial conditions for Case 4

Parameters	**Value**
Number densities	• H_2O - 1.1417x10^{21} m^{-3} • Water Ice - 1x10^{14} m^{-3}
Flow Temperature	53 K
Flow Velocity	(0 902 0) m/s
Collisional Model	Variable Hard Sphere Model
Size of ice grain particles	5 nm
Number of equivalent particles	2.027x10^{19}
Time step (ΔT)	5.4258x10^{-6} seconds

With icy grains inserted into the plume flow along with the water gas particles, the results obtained are different from the plume flow obtained using only water gas molecules. Figure 6.26a shows the mean velocity contour of the plumes. Figure 6.26b shows mean velocity distribution along the y-axis illustrating a deceleration rather than an small acceleration like it was observed in Figure 6.12b for Case 2. This is due to the transfer of momentum from the water gas particles to the ice particles which results in a loss of velocity. When looking at the difference in water gas particle velocities of the two cases in Figure 6.27b and Figure 6.16, it can be observed that the particle velocity is relatively slower at around 800-900 m/s for this case when compared to 950-1050 m/s for Case 2. This difference in velocity leads to the mean velocity dropping from 900 m/s at the surface to 852 m/s. Figure 6.27a shows the velocity of the ice grain particles in the flow and it can be observed that the ice grain particles in the main flow have a higher velocity in the 850-900 m/s range. However, there are many particles present outside the flow of the plumes which are at a significantly lower velocity (<250m/s). These particles are inserted by the simulation due to the influence of the boundary conditions and hence lie outside the flow of the plumes.

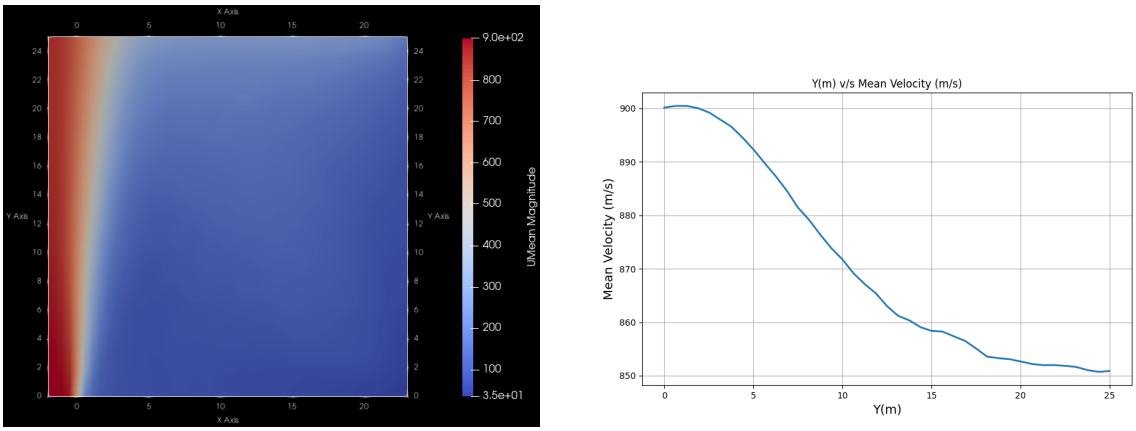

(a) Mean velocity contour for Case 4

(b) Mean velocity distribution for Case 4

Figure 6.26: Mean velocity details of Case 4

Looking at Figure 6.28a, there is a clear shock present in the contour which is due to the supersonic expansion of the flow into near-vacuum conditions. Figure 6.28b shows that there is an initial increase in pressure but it drops after the flow starts to expand into the domain. This is also visible with the mean number density plot shown in Figure 6.29b. While the drop is not that significant for pressure, the mean number density drops off steeply as it expands into vacuum conditions. The gradual drop in pressure is due to the variation in translational temperature as visible in Figure 6.30b, which is directly proportional to both temperature and number density. Another reason for the plateauing of the translational temperature after a point is due to the energy release when the water gas particles

collide with the ice grain particles which releases energy and leads to a relatively higher temperature. As observed, the inclusion of ice grain particles has a strong effect on the flow dynamics.

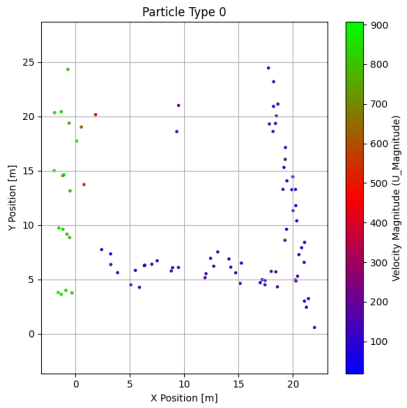

(a) Number of ice grain particles and their velocities for Case 4

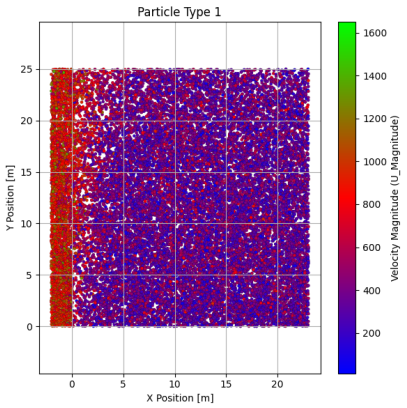

(b) Number of water gas particles and their velocities for Case 4

Figure 6.27: Particles in the flow

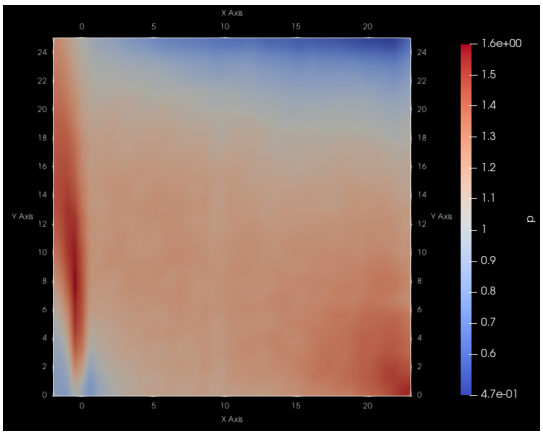

(a) Pressure contour for Case 4

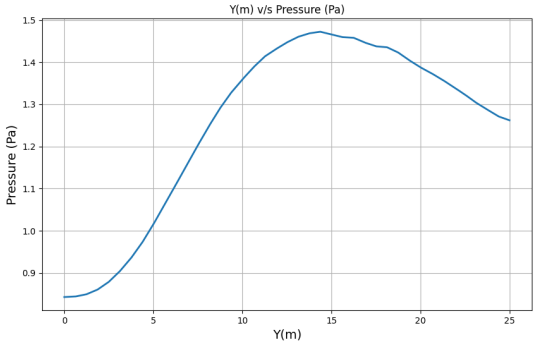

(b) Pressure distribution for Case 4

Figure 6.28: Pressure details of Case 4

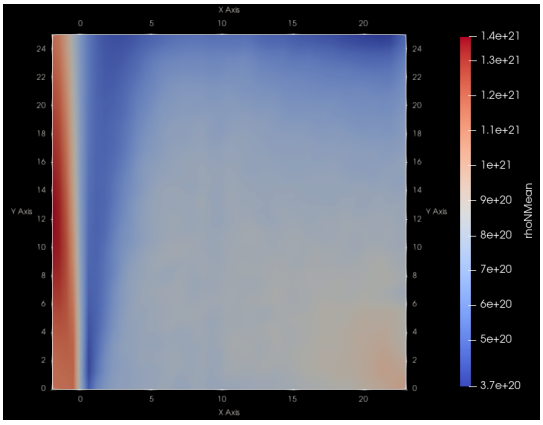

(a) Mean number density contour for Case 4

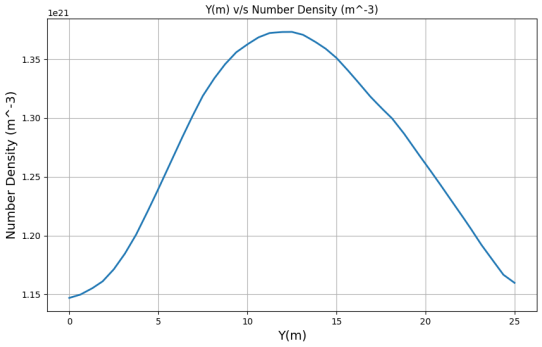

(b) Mean number density distribution for Case 4

Figure 6.29: Mean number density details of Case 4

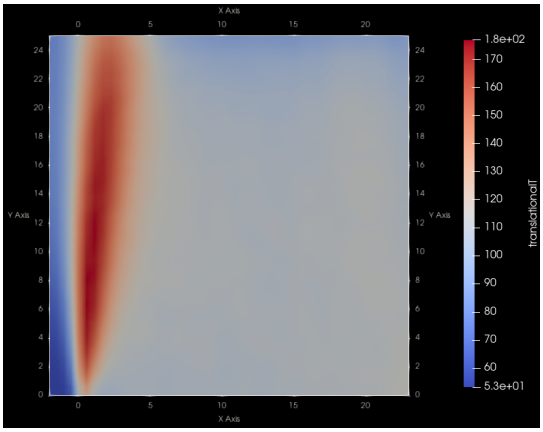

(a) Translational temperature contour for Case 4

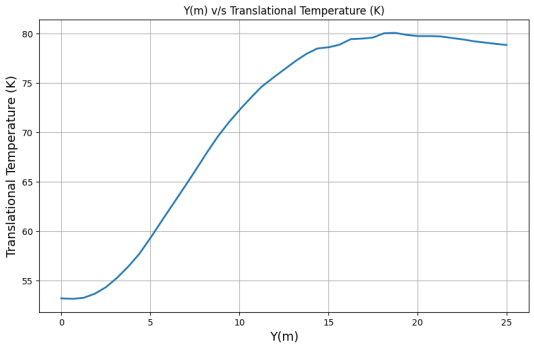

(b) Translational temperature distribution for Case 4

Figure 6.30: Translational temperature details of Case 4

Table 6.11: Results summary after Case 4

Case	Results
Case 1	• Computational domain size is 0.25m x 0.25m with only water gas particles • Water gas particle velocity increases • Mean velocity of the flow decreases • Pressure and mean number density decreases • Translational temperature decreases after an initial spike
Case 2	• Computational domain size is 25m x 25m with only water gas particles with 2750 cells • Water gas particle velocity increases • Mean flow velocity of the flow slightly increases to 905 m/s • Pressure, mean number density and translational temperature all decrease from their initial values
Case 3	• Computational domain size is 25m x 25m with only water gas particles with 44000 cells • Water gas particle velocity increases • Mean flow velocity of the flow increases significantly to 935 m/s • Pressure, mean number density and translational temperature have a steep decrease from their initial values
Case 4	• Computational domain size is 25m x 25m with water gas and ice grain particles with 2750 cells • Water gas particle velocity are relatively lower than Case 2 and ice grain particle velocities are in the 850-900 m/s range • Mean flow velocity of the flow decrease to approximately 850 m/s • Pressure and mean number density decreases while the translational temperature plateaus after the initial spike

6.3. Discussion

With all the results of the cases discussed in the above section, it is important to understand the difference in the results of the first 3 cases (Cases 1, 2 and 3). This section compares the cases by discussing the profiles of each parameter in depth. From the above final case summary it is clear that there was a clear divergence across the various profiles of the 3 cases. This divergence can mainly be governed by 2 major factors: mesh resolution and the domain size. To gain a better understanding of the results, three additional cases were simulated with a computational domain size of 25m x 25m and similar initial conditions with the only difference being the number of cells. The additional cases, Case

3a, 3b and 3c have 6375, 11000 and 44000 cells respectively. This variation in the mesh resolution is used to study the influence of cell size on a DSMC simulation with the results of the simulation attached in Appendix A.

As discussed earlier, according to Bird [2013], the ideal size of each cell in the mesh for a DSMC simulation shall be equal to the mean free path in the direction of flow of the particles. This condition can be acheived but the computational time required for such simulations is signifcantly high. For reference, the time required to obtain initial results for Case 3 was over 5 days. Thus for future cases, a better understanding of the dependence of the results on the mesh resolution is important to save on the computational time and power.

In Case 1, since the computational domain is scaled down by 100x the length of the vent is only 0.02m with a domain size of 0.25m x 0.25m. This restricts the available space for the water gas particles to expand and accelerate which results in a drop in the mean velocity as visible in Figure 6.31. The small domain size also forces boundary interactions with the flow which interferes with the flow expansion which leads to artificially suppressed peak velocities. Bird [2013] also states that in DSMC simulations, the domain size should be large enough such that the boundary condition do not interfere with the flow. In all the next cases, the vent size is increased to the real length of 2m with a domain size of 25m x 25m with Case 2 having a coarse mesh of 2750 cells. Since the mesh is coarse, the sharp increase in mean velocity that normally happens just above the vent appears more gradual. Due to the large cell size of the mesh, the mesh does not have enough resolution to capture very rapid changes over short distances. This results in the acceleration region in the simulation looking more of smoother than it physically is. This phenomenon is often referred to as numerical diffusion or gradient smoothing [Bird, 2013]. While the overall expansion trends remain physically realistic, the coarseness of the mesh may under-predict the acceleration of the mean velocity transitions in the near-field regions. The effect of the cell size is clearly depicted in the mean velocity of Case 3. In Case 3, while the computational domain remains the same as Case 2, the number of cells increases to 275000 making the mesh finer and being very close to Bird [2013] condition of the cell size of the mesh. This increase in the mesh resolution leads to a more accurate capture of the sharp gradient of the mean velocities. The resulting mean velocity profile reaches the highest peak of all three cases showing a continuous and rapid acceleration. From Figure 6.31 Cases 3a, 3b and 3c have been added to show how the number of cells and the cell size influence the results of the simulations.

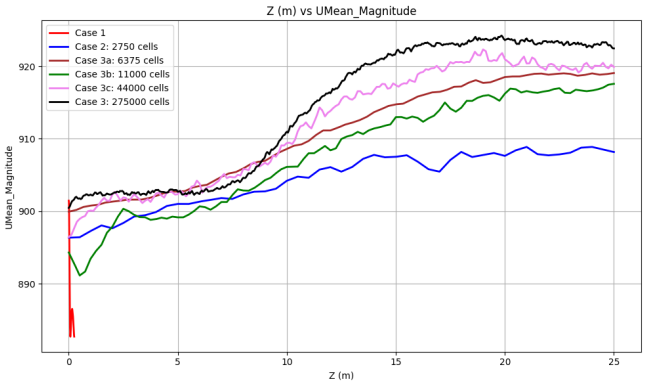

Figure 6.31: Mean velocity comparison of Cases 1, 2, 3, 3a, 3b and 3c

When analyzing the pressure distribution for the 3 cases, the rationale is not very different. In Case 1, the small domain size does not allow for complete expansion and decompression of water gas which causes the pressure to remain relatively high throughout the domain. Case 2 allows for a much better expansion and decompression of water gas with altitude due to the larger domain size, but the results are not perfect. As was the case with the mean velocity, the coarse mesh causes numerical diffusion making the drop in pressure much smoother and under-predicting the results as illustrated in Figure 6.32. Case 3, however, with a fine mesh and larger domain provides the best depiction of the drop in pressure following the rapid expansion and decompression. Similar to the mean velocity plot, there is a divergence between the two cases but Cases 5 and 6 do indicate that there is a bigger

drop in pressure than what is simulated by Case 2. This does make sense as as the plumes move away from the surface, there will be drop in pressure. Looking at the mean number density plots of the five cases in Figure 6.33, the profiles closely resemble those of the pressure shown in Figure 6.32. As expressed in Equation 6.1, pressure is directly proportional to the mean number density, which explains the similarity in trends observed for the five cases and allows the same rationale to be applied to both parameters. From Equation 6.1, it is also evident that pressure is directly proportional to the translational temperature. Subsequently, the translational temperature profiles in Figure 6.34 follow a similar trend to that of pressure and mean number density, as expected, and the same reasoning can be extended to explain their behavior.

$$p = nk_B T_{trans} \tag{6.1}$$

From the above discussion it is clear that going for an extremely coarse mesh for the far-field region could lead to underestimation of results due to numerical diffusion and the influence that the cell size has on the flow of the plumes. However, it would be extremely time consuming if the flow is simulated using the ideal condition of the cell size mentioned earlier in this section. For reference, Case 3c with 44000 cells has a cell size of 0.125m and took over 500hrs to reach close to convergence. Hence, for the far-field region using a relatively coarse mesh like Case 3a (with a cell size of 0.25m) took less than quarter the time of Case 3c.

To summarize, it can be observed that the error percentage in the results for the various cases discussed in this section is approximately 2%, which is a relatively low percentage. This error has been calculated by using Case 3 as the reference point as Case 3 reaches the closest to Bird [2013]'s condition for the cell size less than the mean free path of the particles. With such a low error percentage, the mesh resolution used in cases 2 and 3a can be used for future cases as the computational time required will be significantly large.

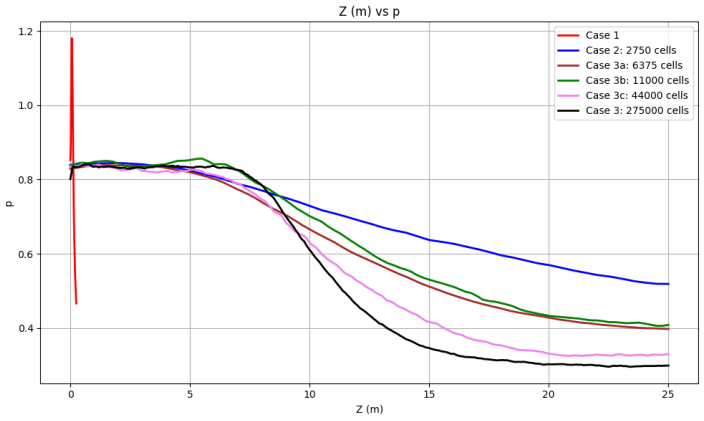

Figure 6.32: Pressure comparison of Cases 1, 2, 3, 3a, 3b and 3c

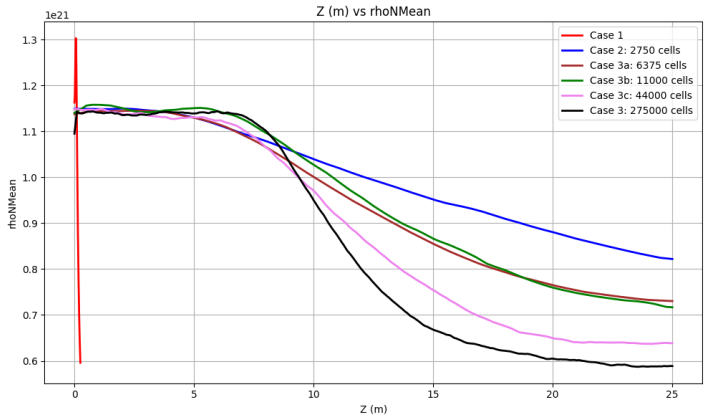

Figure 6.33: Mean Number Density comparison of Cases 1, 2, 3, 3a, 3b and 3c

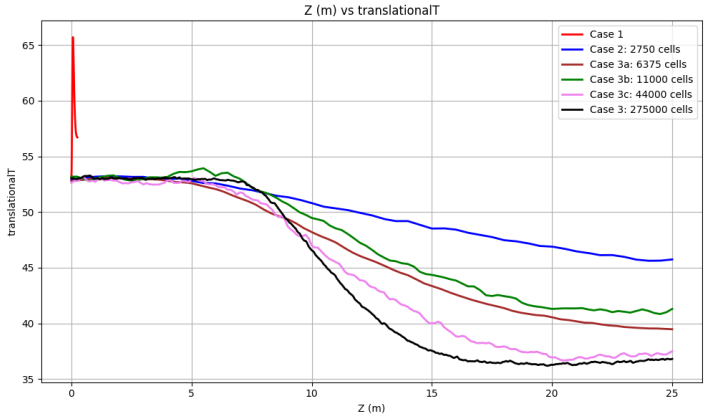

Figure 6.34: Translational temperature comparison of Cases 1, 2, 3, 3a, 3b and 3c

7

Results

With the initial near-field simulation completed, this chapter discusses the results that are obtained at higher velocities to better understand observations made by the Cassini spacecraft.

Table 7.1: Summary of cases for the far-field region

Cases	**Case Description**
Case - 5	• Computational Domain size: 25m x 25m • Number of Cells: 24750 • Velocity: (0 4000 0) m/s • Molecules: H_2O
Case - 6	• Computational Domain size: 25m x 25m • Number of Cells: 2750 • Velocity: (0 4000 0) m/s • Molecules: H_2O, Ice

As it can be noticed in Table 7.1, the velocities are higher from (0 902 0) m/s to (0 4000 0) m/s. This increase in velocity will allows for a better transition within the larger domain helping the solver to capture the full range of physical behaviors of the water gas particles as the plume expands into a vacuum.

7.1. Case 5

Case 5 is similar to Cases 2/3 with almost identical boundary and initial conditions except the velocity set at (0 4000 0) m/s. This case will serve as a link between the near-field and far-field region as the velocity in the cases for far-field region is increased to (0 4000 0) m/s. The number of cells is set to 24750 with a final summary of the initial conditions listed in Table 7.2.

Table 7.2: Initial conditions for Case 5

Parameters	**Value**
Number densities	H_2O - 1.1417x10^{21} m^{-3}
Flow Temperature	53 K
Flow Velocity	(0 4000 0) m/s
Collisional Model	Variable Hard Sphere Model
Number of equivalent particles	4.4598x10^{16}
Time step (ΔT)	5.4258x10^{-6} seconds

The magnitude of the mean velocity shown in Figure 7.1a illustrates a high-velocity region along the vertical centerline starting from the inlet. The mean velocity peaks at around 4000 m/s in the region around the inlet as expected and then gradually starts declining, albeit by not much. The mean velocity drops from 4000 m/s to 3998.5 m/s along the 25m domain height as seen in Figure 7.1b. This decline may be due to the momentum loss of the particles due to collisions occurring because of back scattering of particles because of the boundary conditions. This back scattering is a common occurrence due to the influence of boundary conditions on the flow features. As mentioned earlier in the report, the boundary conditions play an important role in the simulation and according to Bird [2013], the computational domain should be large enough such that the boundary conditions do not interfere with the flow.

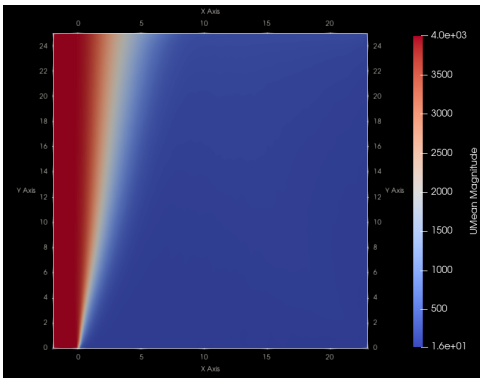

(a) Mean Velocity contour for Case 5

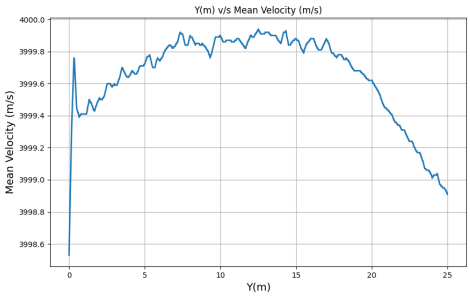

(b) Mean Velocity distribution for Case 5

Figure 7.1: Mean Velocity for Case 5

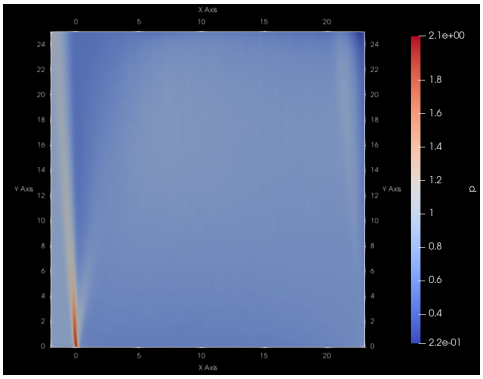

(a) Pressure contour for Case 5

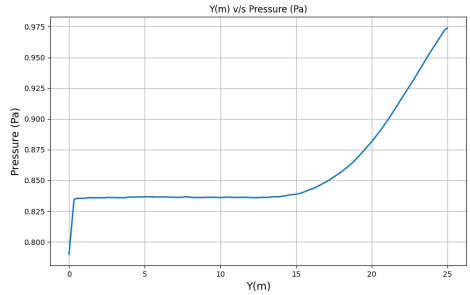

(b) Pressure distribution for Case 5

Figure 7.2: Pressure for Case 5

Figure 7.2b shows that as it is the case for the mean velocity, the change in pressure is also very small but follows a distinct trend. The pressure quickly increases from 0.79Pa to 0.83Pa in the same region as the mean velocity increased but it then stabilizes upto 15m at 0.83Pa. This is then met by a rapid increase to 0.975Pa at 25m. This rapid increase is likely due to the particles clustering near the boundaries due to the back scattered particles which was the case with the mean velocity. This is another typical effect of DSMC simulations being influenced by the boundary conditions due to the domain size not being large enough.

The number density follows a similar trend to pressure starting at $1.08\times10^{21}\mathrm{m}^{-3}$ near the inlet and rising slightly $1.14\times10^{21}\mathrm{m}^{-3}$ coinciding with the location where the pressure and mean velocity both increased initially. This is consistent with the results discussed in Bird [2013] which states that in DSMC simulations with supersonic inflow require a short distance to stabilize into a steady jet. After stabilizing, the number density gradually increases to $1.24\mathrm{x}10^{21}\mathrm{m}^{-3}$ at 25m. The accumulation effect

due to the boundary conditions influencing the flow features by limiting the expansion due to the small computational domain size. The translational temperature remains nearly constant throughout most of the domain, consistent with the low inlet value of 53K. Only a slight increase is observed in the upper part of the domain, rising to 56.7K at 25m. This slight increase in temperature is consistent when considering the Equation 6.1 as the flow is still almost within the continuum flow regime with the knudsen number approximately equal to 0.04.

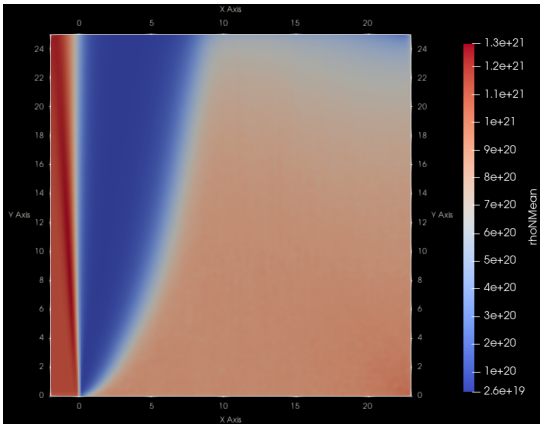

(a) Mean number density contour for Case 5

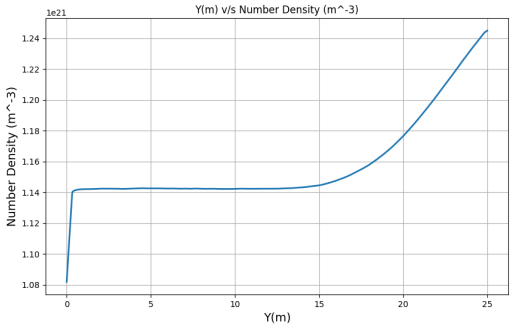

(b) Mean number density distribution for Case 5

Figure 7.3: Mean number density for Case 5

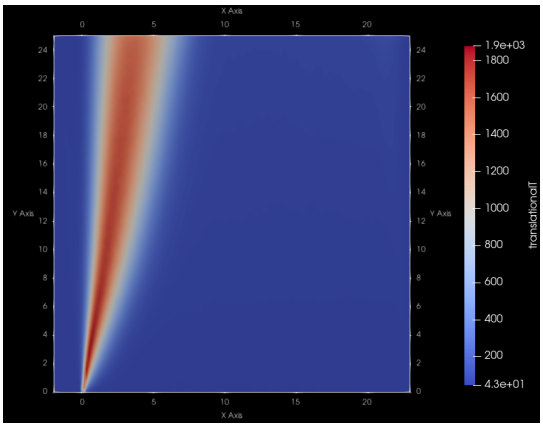

(a) Translational temperature contour for Case 5

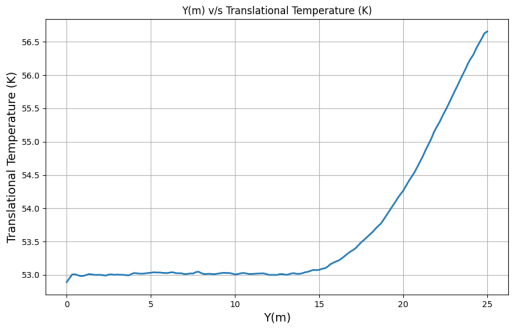

(b) Translational temperature distribution for Case 5

Figure 7.4: Translational temperature for Case 5

7.2. Case 6

Case 6 follows the previous case by inserting ice grain particles to study and analyses the effect that ice grains have on the flow features. The boundary and initial conditions remain identical to Case 6 except for the addition of ice grain particles and it has been summarized in Table 7.3.

Similar to Case 4, the influence of ice grain particles in the flow is evident in Figure 7.5 with a steady decline in the mean velocity of the flow. While difference is not substantial, the gradual decline does indicate the presence of slower particles in the flow as observed in Figure 7.6. Figure 7.6a shows that the ice grain particles in the flow have a relative lower velocity when compared to the water gas particles in Figure 7.6b. The ice grains reach a maximum velocity of around 4000 m/s while some of the water gas particles accelerate well above 4000 m/s but majority of the water gas particles stay between the 3800-4000 m/s range. The faster water gas particles lose their velocities when it collides with the ice grain particles which results in reduction in velocity of the water gas particles leading to an overall lower mean velocity of the flow. The drop is not large as the particles travel through this domain quickly due

to the small domain size and high velocity leading to a 0.4% drop in mean velocity when compared to 5.45% drop in mean velocity in Case 4.

Table 7.3: Initial conditions for Case 6

Parameters	**Value**
Number densities	• H_2O - 1.1417x10^{21} m^{-3} • Water Ice - 1x10^{18} m^{-3}
Flow Temperature	53 K
Flow Velocity	(0 4000 0) m/s
Collisional Model	Variable Hard Sphere Model
Size of ice grain particles	5 nm
Number of equivalent particles	2.027x10^{19}
Time step (ΔT)	5.4258x10^{-6} seconds

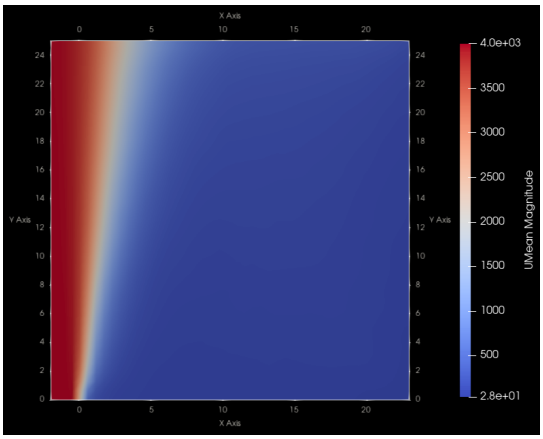

(a) Mean velocity contour for Case 6

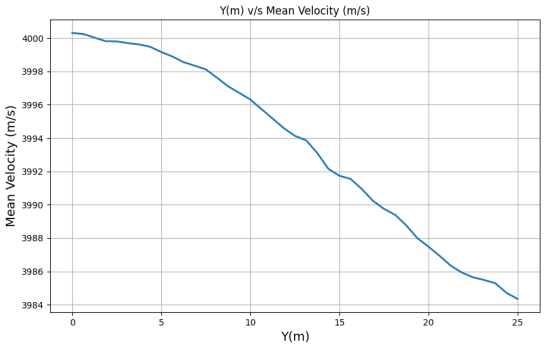

(b) Mean velocity distribution for Case 6

Figure 7.5: Mean velocity details of Case 6

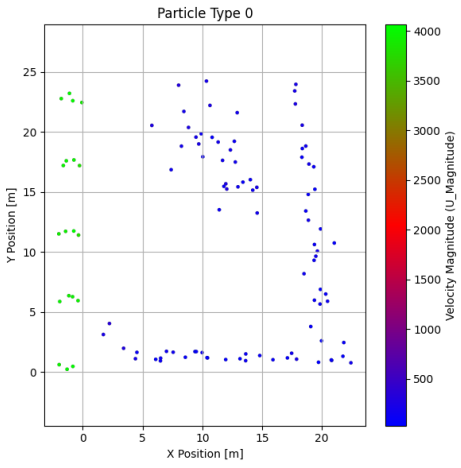

(a) Number of ice grain particles and their velocities for Case 6

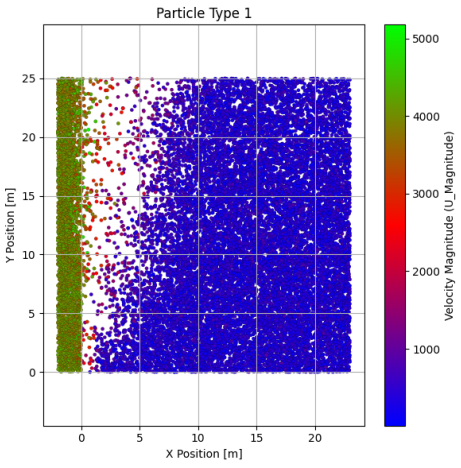

(b) Number of water gas particles and their velocities for Case 6

Figure 7.6: Particles in the flow

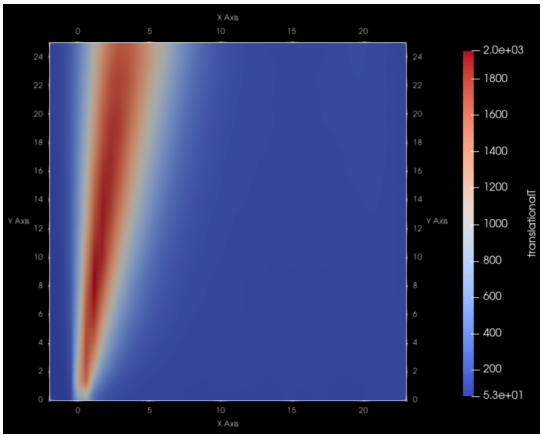

(a) Translational temperature contour for Case 4

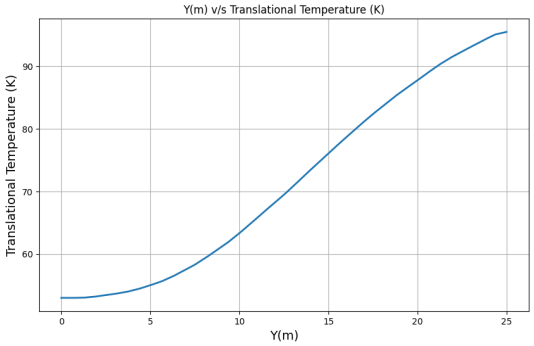

(b) Translational temperature distribution for Case 6

Figure 7.7: Translational temperature details of Case 6

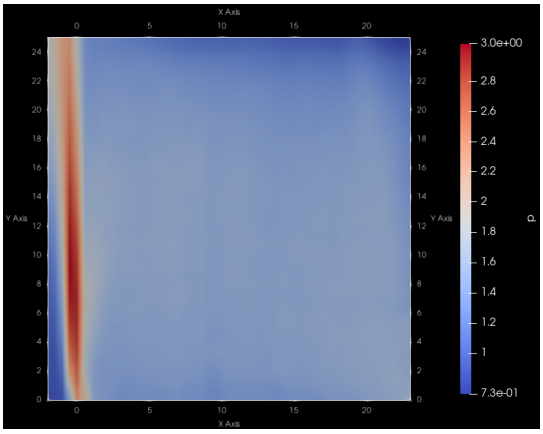

(a) Pressure contour for Case 6

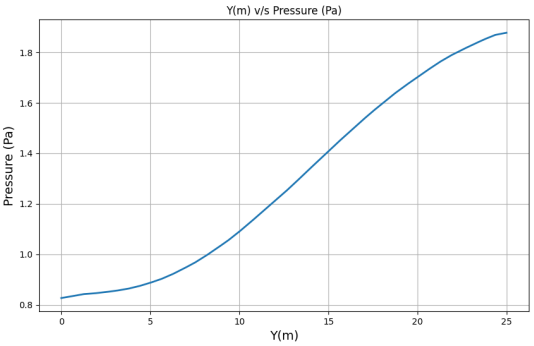

(b) Pressure distribution for Case 6

Figure 7.8: Pressure details of Case 6

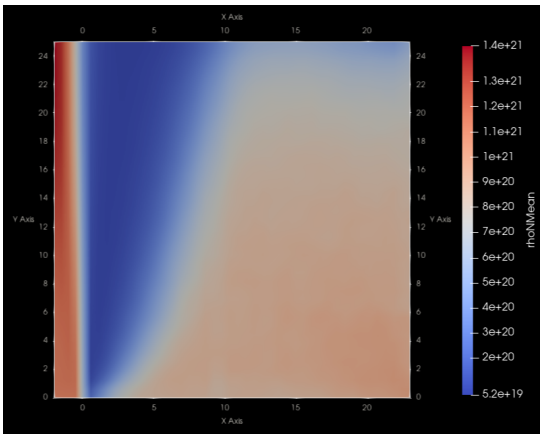

(a) Mean number density contour for Case 6

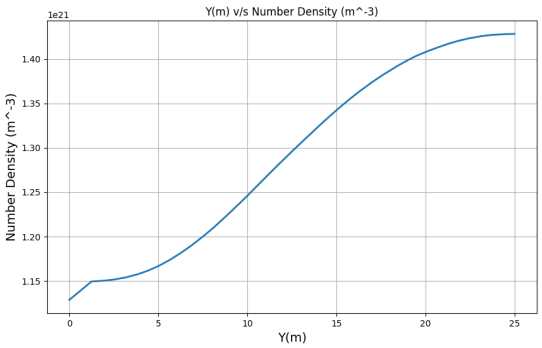

(b) Mean number density distribution for Case 6

Figure 7.9: Mean number density details of Case 6

The translational temperature follows a steady increase from 53K to 95K at 25m altitude as observed in Figure 7.7. Meanwhile the translational temperature in Case 4 increased to around 89K. This difference

in temperature is due to the higher velocity of particles leading to a higher kinetic energy which results in a slighly larger loss in energy when collisions occur between the particles. Figure 7.9 shows the mean number density profile of the flow which increases from 1.13x10^{21} m^{-3} to 1.43x10^{21} m^{-3} at 25m. This increase is due to the high velocity of the flow which results in the flow exiting the domain quickly which results in the flow being not fully expanded and due to the high number density of particles, the number density continues to increase as the boundary conditions continue to influence the results. The pressure profile of this case illustrated in Figure 7.8 follows a similar trend acting in accordance with Equation 6.1 with the pressure increasing from 0.81Pa at the surface to 1.82Pa at 25m.

8

Post-Processing

With the completion of these the simulations ranging from the near-field region to the far-field region using dsmcFoam, post-processing of the results is carried out to gain valuable insights the physics and the behavior of the water gas and ice particles. An important factor that needs to be evaluated is the possibility of grain growth of the ice grain particles after they exit the vents and what conditions influence its growth, if any.

8.1. Grain growth

To check for ice grain growth, it is vital to understand the factors that influence the same. A continuum overlay approach developed by Viswanath et al. [2005] originally used to model soot combustion in rocket plumes has been modified by Li et al. [2013] for the ice grain growth modeling using mass conservation law. Using this approach, the mass of an ice grain can be written as:

$$m_g = \frac{4}{3}\pi r_g^3 \rho_w \tag{8.1}$$

where ρ_w is the density of water gas. The increase in the mass of ice grain after one time step can be defined as:

$$m_g + C\Delta t \tag{8.2}$$

where C is the accretion rate since the number of water molecules colliding with the spherical surface of the ice grain. The accretion rate is given as:

$$C = \pi r_g^2 \overline{v}_w n_w q \tag{8.3}$$

where q is the sticking probability, $\overline{v}_w$ is the mean thermal speed of water gas which be derived using Equation 8.4 and n_w is the local number density of water gas molecules.

$$\overline{v}_w = \sqrt{\frac{8k_b T_w}{\pi m_w}} \tag{8.4}$$

where k_b is the Boltzmann constant ($1.38e^{-23} J/K$) and T_w is the local temperature of water gas. Based on the above set of equations, the new ice grain radius can now be simplified as:

$$r_g' = (\frac{3(\frac{4}{3}\pi r_g^3 \rho_w + C\Delta t)}{4\pi\rho_g})^{1/3} \tag{8.5}$$

And the rate of increase of the ice grain radius is:

$$\frac{dr_g}{dt} = \frac{Cm_w}{4\pi r_g^2 \rho_g} \tag{8.6}$$

Substituting for C and simplifying the equation, gives the ice grain growth equation:

$$\frac{dr_g}{dt} = \frac{\overline{v}_w n_w q m_w}{4\rho_g} \tag{8.7}$$

where m_w is the mass of the water gas molecule, q is the sticking coefficient and ρ_g is the density of the ice grain. To simplify Equation 8.7, it can be integrated and written as:

$$r_g = r_0 + (\frac{\overline{v}_w n_w q m_w}{4\rho_g})t_{res} \tag{8.8}$$

where r_0 is the initial radius of the ice grain and t is the residence time of the ice grain in that particular region. While this approach of checking for the growth of ice grains will be the most efficient, it makes the following assumptions:

- The ice grain stays in the same cell during t_{res}
- The local flow properties do not change during t_{res}
- The ice grain properties remain the same during the t_{res}
- The ice grain growth is consistent over the entire ice grain

Modeling the growth of ice grains was done using a python script which has been uploaded on the GitHub repository[1]. To make the model more realistic, randomness can be introduced into 2 factors which are influenced naturally, the sticking coefficient and the residence time. Sticking coefficient for each ice grain is different, hence a introducing randomness allows for a more realistic results. Since it has been assumed that the ice grain stays within the same cell and the flow properties do not change during t_{res}, introducing randomness and having different residence times for each grain, would allow for a more robust system for checking of growth of the icy grains. However, for better understanding the grain growth for the ice grain particles of Cases 4 and 6 for the sticking coefficient at 0.2 [Li et al., 2013] and t_{res} has been varied by the amount of time that a particle resides in the cell. From Figure 8.3 and Figure 8.4 it is clear that as the residence time increases the size of the particles increases for the fixed sticking coefficient. This does make sense physically as the final grain size is directly proportional to the residence time as seen in Equation 8.7.

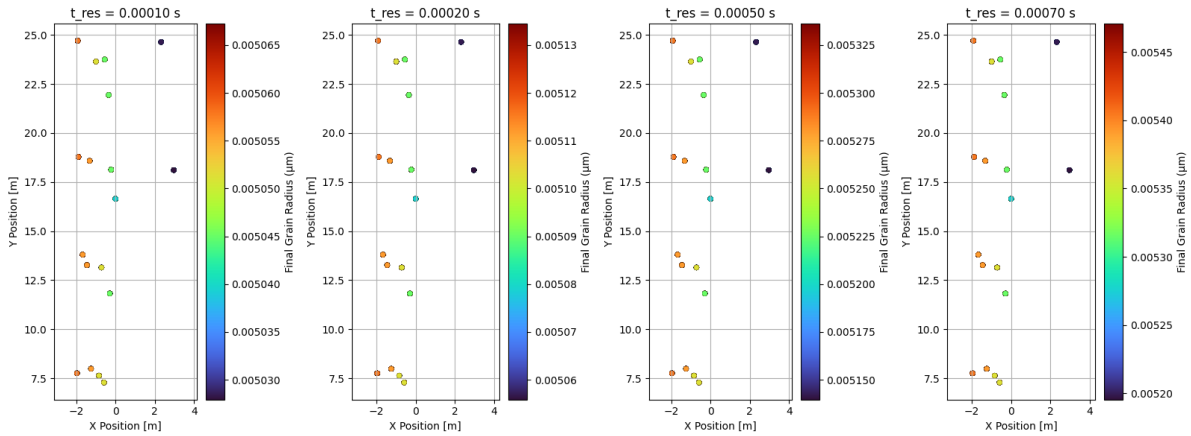

(a) t_{res} = 1x10^{-4} seconds **(b)** t_{res} = 2x10^{-4} seconds **(c)** t_{res} = 5x10^{-4} seconds **(d)** t_{res} = 7x10^{-4} seconds

Figure 8.1: Growth of ice grain particles in Case 4 for q = 0.2 for different residence times

[1] `https://github.com/deepanshu6901/Investigating_the_Physics_of_the_Plumes_of_Enceladus_using_DSMC`

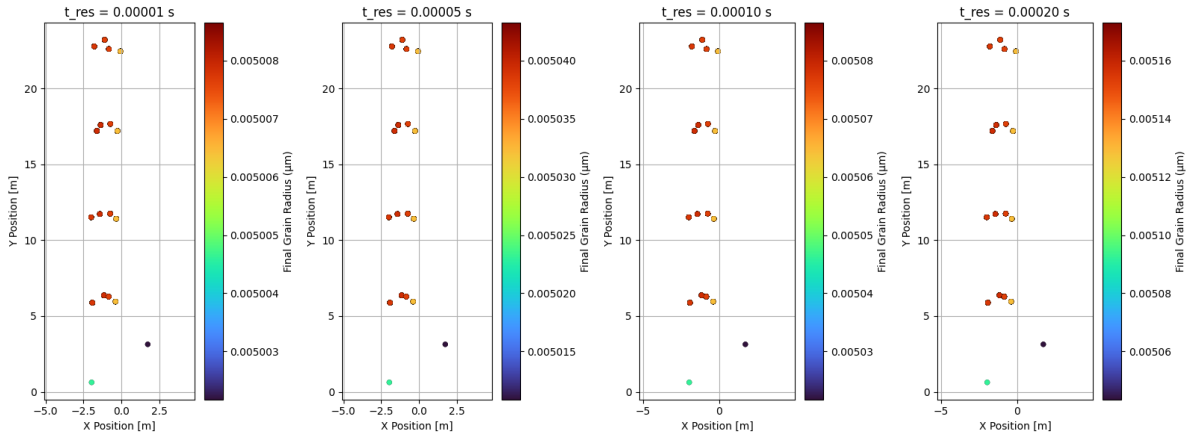

(a) t_{res} = 0.1x10^{-4} seconds **(b)** t_{res} = 0.5x10^{-4} seconds **(c)** t_{res} = 1x10^{-4} seconds **(d)** t_{res} = 2x10^{-4} seconds

Figure 8.2: Growth of ice grain particles in Case 6 for q = 0.2 for different residence times

8.2. Analysis

After looking at the growth of ice grain particles in the flow, it is important to see how these particles effect the flow properties for different flow velocities. Figure 8.3 and Figure 8.4 illustrate the different parameters for flow velocities of (0 902 0)m/s and (0 4000 0)m/s respectively.

Figure 8.3a, the mean velocity with only water gas particles increases gradually from around 900 m/s to 905 m/s while it decreases to 851 m/s when the flow has ice grain particles. This decrease in velocity is due to the momentum being transferred from water gas particles to the ice grain particles due to collisions which causes the particles to lose their kinetic energy. As discussed in Case 4, the ice grain particles in the flow have a maximum velocity of approximately 900 m/s (Figure 6.27a) which means the ice grain particles are not accelerating significantly due to the relatively larger size when compared to the water gas particles. Figure 8.3b exhibits the translational temperature of the two cases and it shows an opposing behavior. Case 2 shows that the temperature decreases from 53K to approximately 46K downstream, illustrating cooling of the particles during expansion. However, the translational temperature for Case 4 increase to 80K before plateauing. This indicates the transfer of kinetic energy through collisions which increases the translational temperature of the flow. For Case 2, both mean number density (Figure 8.3d) and pressure (Figure 8.3c) decrease gradually as the flow expands into outerspace but this changes with the introduction of ice grain particles as both values increase gradually and decreasing. Due to the large size of the ice grain particles, the presence restricts the expansion of the water gas molecules leading to more water gas particles to be accumulated in that region leading to a higher pressure and mean number density. The flow then expands downstream of the ice grain particles which leads to a gradual decrease in the value of the two parameters.

Moving onto the next two cases, Cases 5 and 6, the difference in mean velocity as observed in Figure 8.4a for the two cases is not very significant. The mean velocity decreases from around 4000 m/s to 3992 m/s for Case 5 and 3987 m/s for Case 6. This small difference in velocity is due to the presence of ice grain particles in Case 6 which causes collisions and decreases the mean velocity. Due to the extremely high velocity of particles, there is steady loss of kinetic energy by the water gas particles which gradually increases the translational temperature of the flow as visible in Figure 8.4b. The higher translational temperature in Case 6 when compared to Case 5, is due the loss of kinetic energy being higher because of the collisions of water gas and ice grain particles. When looking at the pressure and mean number density of Cases 5 and 6 in Figure 8.4c and Figure 8.4d, it is a steady incline when compared to Cases 2 and 4. This difference is also due to the extremely high velocity of the particles which due to the small domain size does not allow for full expansion of the flow properties and this underexpansion of the flow leads to relatively higher pressure and number density.

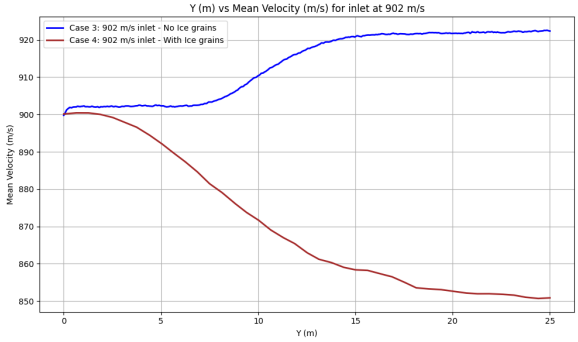

(a) Mean Velocity

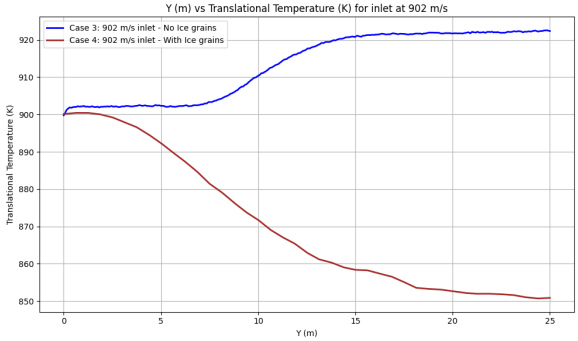

(b) Translational Temperature

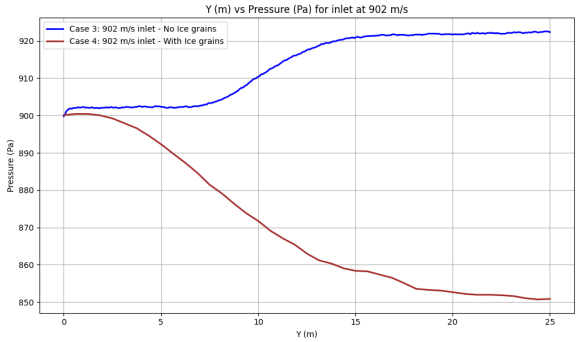

(c) Pressure

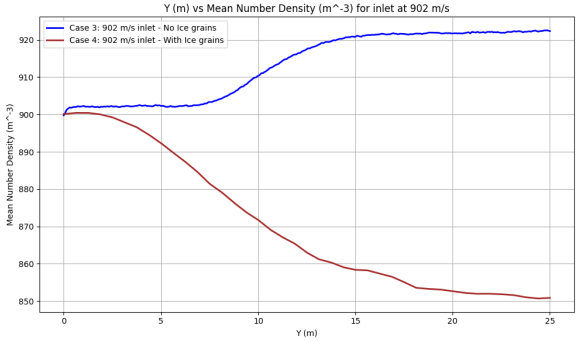

(d) Mean Number Density

Figure 8.3: Comparison of Cases 2 and 4

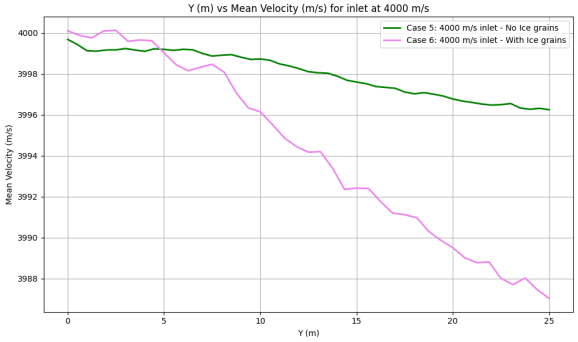

(a) Mean Velocity

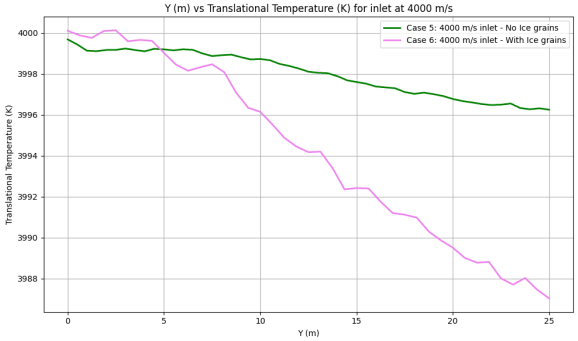

(b) Translational Temperature

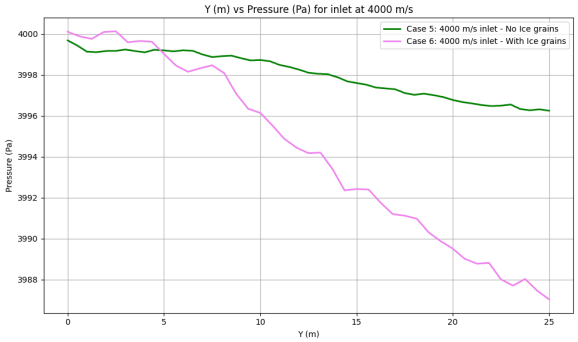

(c) Pressure

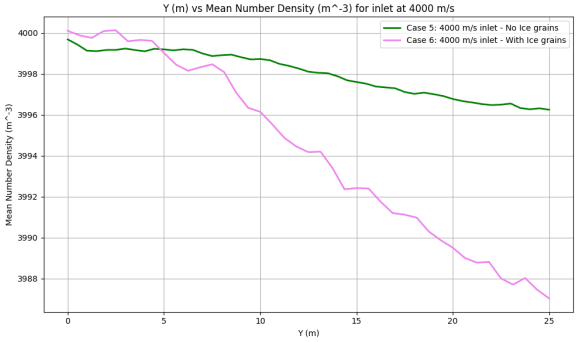

(d) Mean Number Density

Figure 8.4: Comparison of Cases 5 and 6

Table 8.1: Comparison of plume behavior at different inlet velocities

Inlet Velocity	Water Gas Particles only	Ice Grain + Water Gas Particles
(0 902 0) m/s	• Slight acceleration from 900m/s to 905m/s • Translational temperature cools from 53K to 46K • Pressure and Mean Number Density decreases	• Large deceleration from 900m/s to 851m/s • Translational temperature increases upto 80K • Pressure and Mean Number Density increases and then decreases
(0 4000 0) m/s	• Slight deceleration from 4000m/s to 3992m/s • Steady temperature of about 62K • Pressure and Mean Number Density increases	• Relatively larger deceleration from 4000m/s to 3987m/s • Translational temperature increase upto 91K • Pressure and Mean Number Density increases

The analysis performed above involves studying cases with similar mesh resolution for a more consistent analysis as the mesh convergence study that was performed in subsection 6.2.3 indicated an acceptable error range of approximately 2%. However, when investigating Case 3, where the cell size is approximately equal to the mean free path of the molecules, the mean number density contour in Figure 6.21, the flow is similar to a moderately underexpanded nozzle.

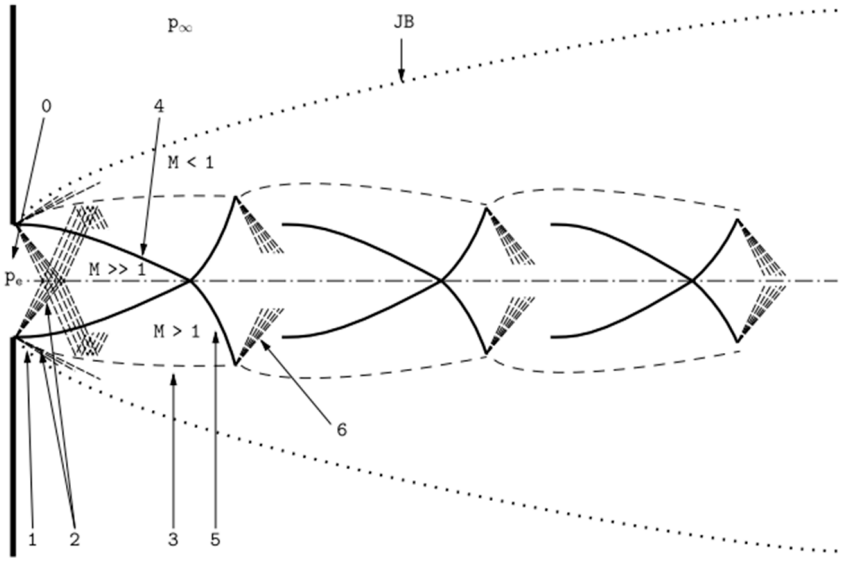

Figure 8.5: Jet structure of a moderately underexpanded nozzle [Franquet et al., 2015]

Franquet et al. [2015] reviewed different underexpanded nozzles and its flow characteristics. Figure 8.5 shows a sketch of the structure of a moderately underexpanded nozzle. At the exit plane (marker 0), is a Prandtl-Mayer expansion fans(marker 2) which expands the fluid downstream of the lips of the nozzle increasing the velocity of the flow while decreasing the pressure and temperature [Franquet et al., 2015]. The constant pressure streamline (marker 3) represents the region where the pressure equals to the ambient pressure and this is where the expansion fans are reflected into compression waves. These waves converge towards the inner part of the jet forming an oblique shock (marker 4). The incidence of the oblique shocks from the other side creates another oblique shock (marker 5) which opens towards the outside boundary of the jet. When this oblique shock encounters the constant pressure streamline

(marker 3), it creates another expansion fan (marker 6) and this structure continues to be replicated further downstream of the flow.

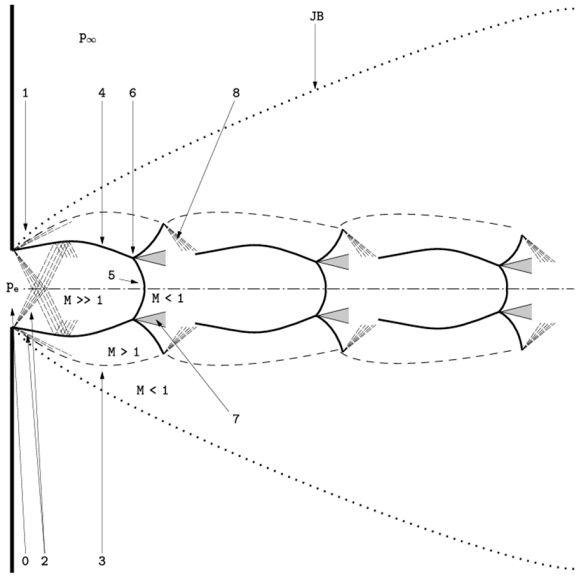

Figure 8.6: Jet structure of an highly underexpanded nozzle [Franquet et al., 2015]

When comparing the flow of an underexpanded nozzle to the simulations results of Case 3, this pattern can be clearly observed as seen in Figure 8.7. This is the same with Case 5 where the flow follows a similar trend to that of an underexpanded nozzle but it is slightly different when compared to Case 3. In Case 5, the interception of the expansion fans is 10m more downstream than Case 3 as the increase in velocity at the exit of the vent leads to a higher mass flow rate. This characteristic is evident when evaluating the results obtained by Kashkovsky et al. [2023] which shows that the shock moves further downstream with an increase in exit Mach number.

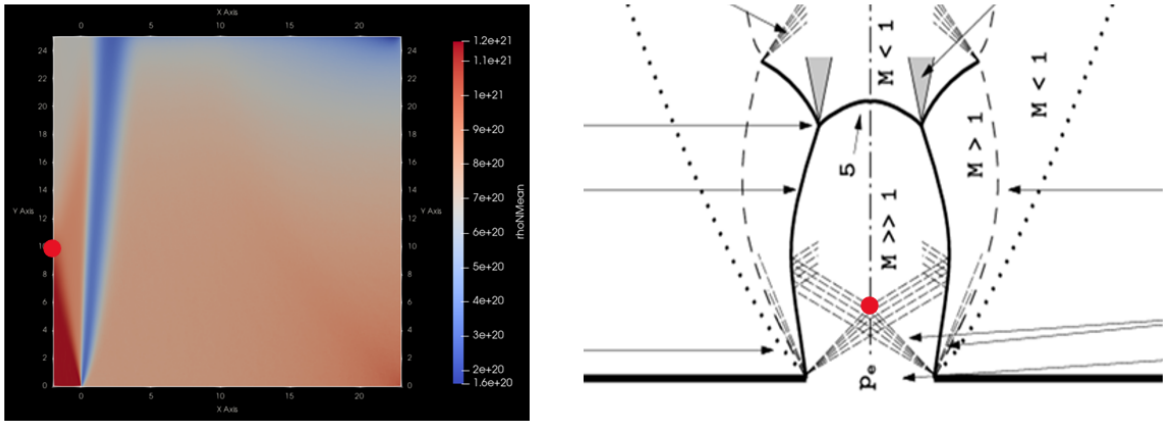

Figure 8.7: Jet structure of an highly underexpanded nozzle [Franquet et al., 2015]. The red dot on the contour on the left is the location at which the expansion fan ends as seen in the figure of the highly undereexpanded nozzle on the right.

Kashkovsky et al. [2023] studies the flow for 5 different knudsen numbers with the highest value of 0.008. The variation in knudsen number is another crucial factor to evaluate and predict the development of the plumes into the far-field region as the knudsen number of the flow of plumes of Enceladus moves from the transitional regime in the near-field region to free molecular regime in the far-field region (10km +). An important observation that can be made from Figure 8.9 is that the shocks become significantly weaker as the knudsen number increases. This observation shows that for the plumes of Enceladus,

as the knudsen number increases, the velocity of the flow will decrease as the shocks will become weaker leading to them disappearing. To study this characteristic, a simulation was performed with a computational domain of 60km x 60km with 14000 cells and the simulation results have been discussed in Appendix B. While the shock has not been captured accurately due to the poor mesh resolution, but it does show the effect of how the shock will not be captured as the flow transitions from transition regime to rarefied and free molecular regime.

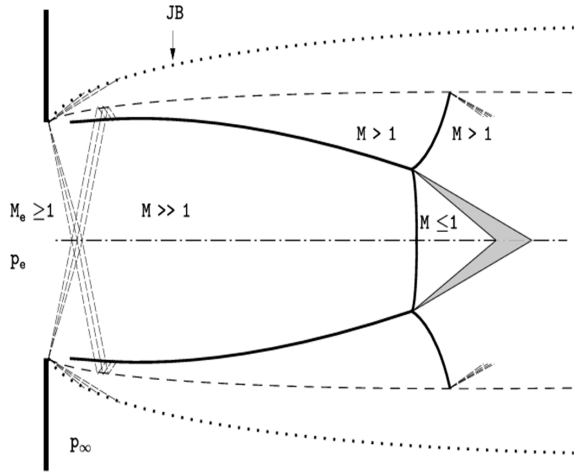

Figure 8.8: Jet structure of a very highly underexpanded nozzle [Franquet et al., 2015]

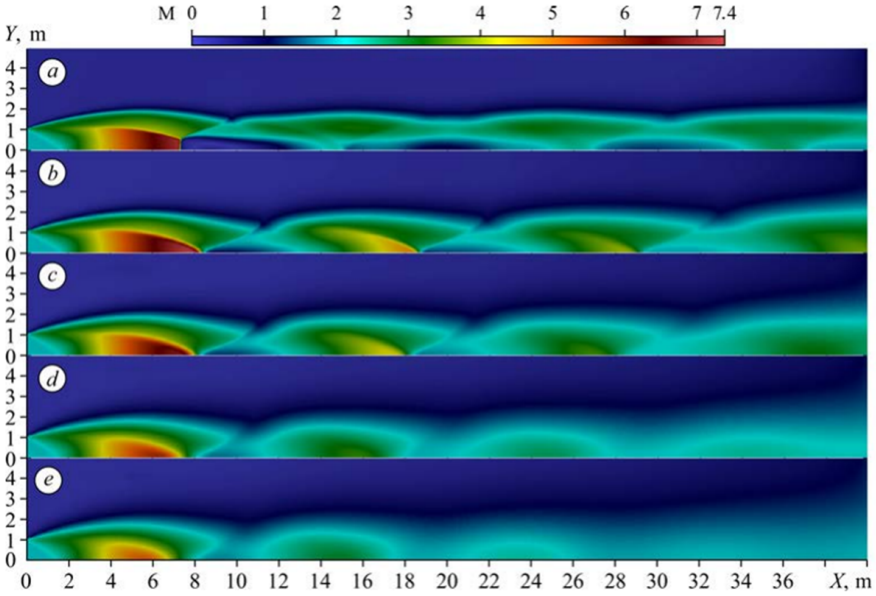

Figure 8.9: Shockwave structure of an underexpanded nozzle jet for various Knudsen numbers: 0.0005 (a), 0.001 (b), 0.002 (c), 0.004 (d), and 0.008 (e) [Kashkovsky et al., 2023]

This flow characteristics discussed above can be observed in the images captured by the ISS instrument onboard the Cassini spacecraft. Figure 8.10 was captured on 21st November 2009 at a distance of approximately 11000km from the moon. It clearly captures the plumes originating from one of the vents. While it is not clear which tiger stripe this plume is originating from, the structure of the plume can be identified. Like the simulation results of Cases 3 and 5, it is evident that the plumes observed by Cassini in Figure 8.10 also show a structure similar to the flow of an underexpanded nozzle. The line in red in Figure 8.10 is illustrative of an expansion fan as seen in Figure 8.5 and the green line shows

the location of intersection of the oblique shocks. From Figure 8.10 it can also be observed that there are no further shocks that are occurring as the knudsen number reaches extremely high due to which the shocks disappear.

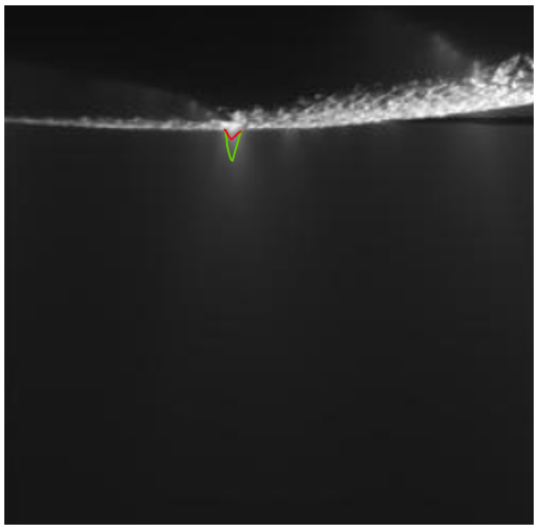

Figure 8.10: Image captured by the ISS instrument onboard the Cassini spacecraft on 21st November 2009 at approximately 11000km

Another image captured by the Cassini spacecraft, Figure 8.11, on 6th May 2015 shows multiple plumes, both big and small, originating from the tiger stripes. Plume (a) in Figure 8.11 is a peculiar case as it highlights the structure of a highly or a very highly underexpanded jet (structure shown in Figure 8.6 and Figure 8.8 respectively) and not of a moderately underexpanded jet. The structure of the plume observed by the Cassini spacecraft in Figure 8.11 is narrow as shown in red lines but the top part of the plume shown in green illustrates a mach disk (marker 5 in Figure 8.6) which is a very characteristic flow feature of a highly and very highly underexpanded jet. For a highly underexpanded jet (as shown in Figure 8.6), the oblique shock is bulged instead of the converging oblique shock that is observed which indicates that the flow is a very highly underexpanded jet. From Figure 8.8 it is clear that the flow decelerates after the mach disk. This is also confirmed by Figure 8.9 which indicates the same but also illustrating that the flow with a sufficiently high knudsen number starts to spread out over a large region. This spreading of particles over a large region has been clearly observed in Figure 8.11 as the flow goes from collimated to becoming completely spread out after the mach disk [Franquet et al., 2015].

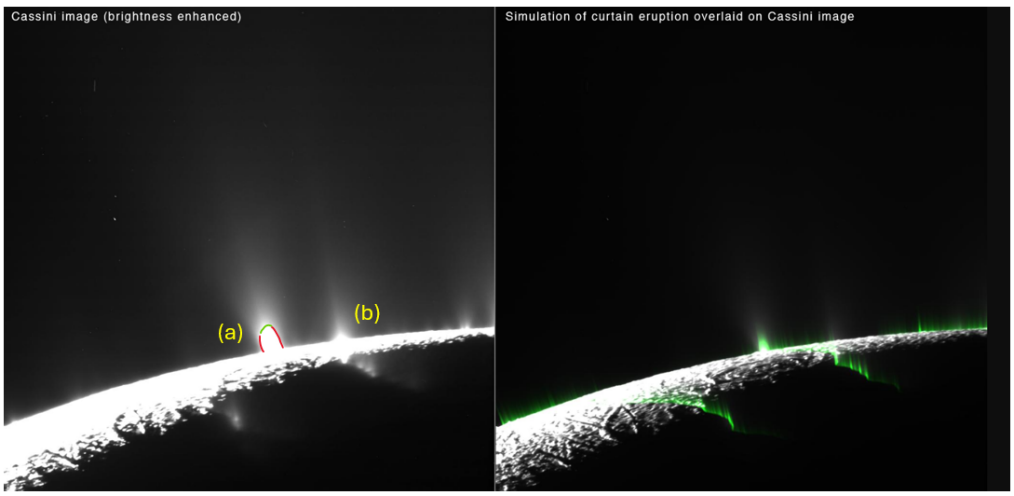

Figure 8.11: Image captured by the ISS instrument onboard the Cassini spacecraft captured on 6th May 2015 (Image Courtesy: NASA)

According to Franquet et al. [2015], as the knudsen number increases, the shocks should start getting weaker and eventually disappear. However, in Figure 8.10 and Figure 8.11, this is not the case as there are clearly well defined shock regions in the flow. The main reason behind this is the mass flow rate of particles. According to Hansen et al. [2011], the mass flow rate of the plumes exiting the vent is over 200 kg/s, which is significantly larger than the mass flow rate simulated in this thesis or the work studied by Kashkovsky et al. [2023].

8.3. The Occultation method

The Cassini spacecraft during its visit to the Saturnian system recorded and recorded many observations using the various instruments discussed in section 1.4. The occultation method is a powerful observational technique used to study the properties of the plumes of Enceladus. It involves measuring the change in light intensity from a distant source, such as a star or the Sun, as it passes behind the target body. By analyzing the absorption of light at different wavelengths, it can deduce the composition, density, and structure of the plumes. This chapter discusses these observations and then compares them to the occultation data obtained from far-field region simulation. Occultations of stars is one of the most important data collected by the UVIS by watching the plumes of Enceladus passing between a star and the spacecraft. It allows to analyze and understand the structure and composition of plumes. It relies on the Beer-Lambert Law, which describes the attenuation of light as it passes through an absorbing medium and is mathematically expressed in Equation 8.9 [Hansen et al., 2011].

$$I = I_0 e^{(-n_c * \sigma)} \tag{8.9}$$

Where I is the occulted intensity of the star, I_0 is the unocculted intensity of the star, n_c is the column density an σ is the absorption cross-section of the particle(s). After rearranging the above equation, τ or optical depth is obtained as expressed in Equation 8.10.

$$\tau = -n_c * \sigma = -ln \frac{I}{I_0} \tag{8.10}$$

From the occultation data obtained by the UVIS instrument onboard the Cassini spacecraft, the resulting occultation profile plots the optical depth as a function of time which bears a direct correlation to the density and structure of the plumes. A higher optical depth indicates the presence of a dense region of the plume while a lower optical depth indicates a less dense region. Stellar and solar occultations observed by the UVIS revealed a dominant presence of water in the gas composition of the plumes [Hansen et al., 2006]. There have been 7 observed occultations of stars including one of our Sun by Enceladus and/or its plume by the Cassini spacecraft which have been discussed in Table 8.2.

Table 8.2: Summary of UVIS occultation observations with water vapor detections [Hansen et al., 2011]

Date	Source	Channel	Integration Time	Min Ray Height (km)	H_2O Flux (kg/s)
17 Feb 2005	λ Scorpii	FUV/HSP	—	—	No detection
14 Jul 2005	γ Orionis	FUV/HSP	5 s / 2 ms	$\sim$100	Detected
24 Oct 2007	ζ Orionis	FUV/HSP	5 s / 2 ms	15.6	240
18 May 2010	Sun	EUV	1 s	$<$60	338
19 Oct 2011	ϵ Orionis	FUV/HSP	2 s / 8 ms	18	337
11 Mar 2016	ϵ Orionis	FUV/HSP	1 s / 2 ms	$\sim$50	313
27 Mar 2017	ϵ Canis Majoris	FUV/HSP	1 s / 2 ms	60	250

Hansen et al. [2011] provided a summarized observations of solar occultation data which establishes a baseline understanding of the properties of the plumes. This data has been used in this thesis to validate the simulation models used. Figure 8.12 shows the UVIS observations obtained in 2010 along with the INMS data of the E7 flyby. Figure 8.13 shows the observations during the 2010 solar occultation illustrating the optical depth profile of the plumes of Enceladus in the Extreme UV (EUV - 85 to 100

nm) wavelength plotted as a function of time. Hansen et al. [2011] discussed the properties of the jets identified in Figure 8.13 in Table 8.3.

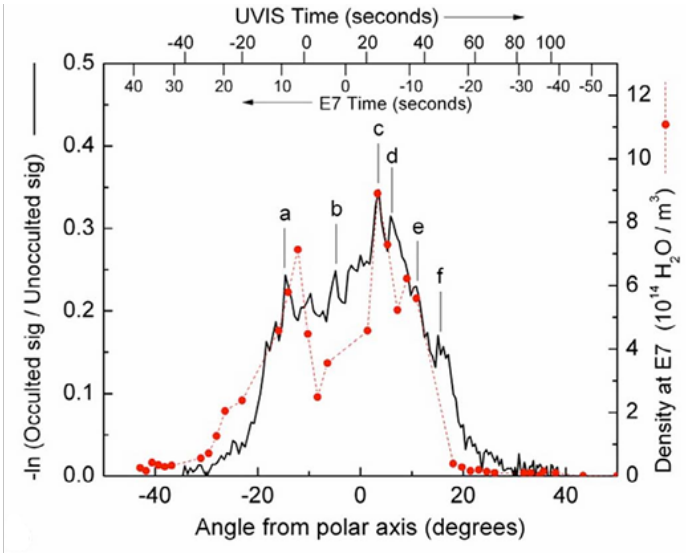

Figure 8.12: UVIS and INMS measurements are plotted versus angle about the center of Enceladus as viewed from Cassini's position during the 2010 UVIS observation. Time is relative to the closest approach for the E7 2009 flyby and relative to minimum ray height for the 2010 solar occultation

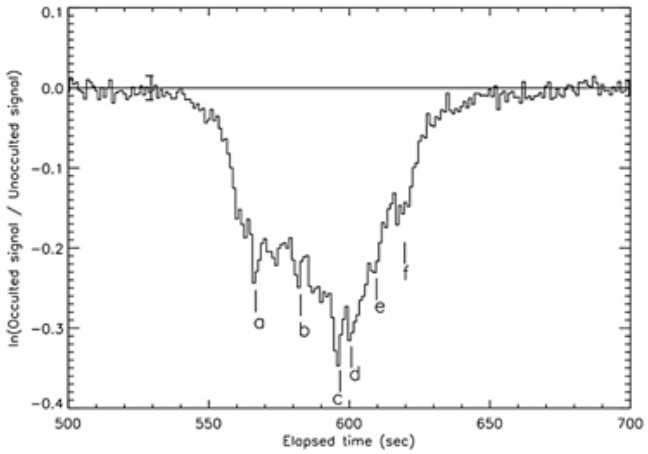

Figure 8.13: Optical Depth variation of the plumes of Enceladus during the 2010 solar occultation showing distinct absorption features from gas jets labeled a-f [Hansen et al., 2011]

8.4. Occultation results of the DSMC simulations

Now with a basic understand of how occultation results are obtained and the observations made by the Cassini spacecraft, this section now evaluates the occultation results obtained through the simulations. It is important to note that the simulations are of a single jet plume and not an entire crack as the observations made by the Cassini spacecraft shown in Figure 8.12 and Figure 8.13 are of multiple plume jets. 4 cases in total were evaluated for the occultation results which includes Cases 3 - 6. Cases 3 and 4 compare the occultation results at 25m with and without ice grain particles with an inlet velocity of (0 902 0) m/s. Cases 5 and 6 also do the same with an inlet velocity of (0 4000 0) m/s as discussed earlier.

Figure 8.14 shows the optical depth of a single plume jet simulated with water gas particles and with and without ice grain particles at 25m altitude and an inlet flow velocity of (0 902 0) m/s. It can clearly be

Table 8.3: Summary of the properties of the jets identified in Figure 8.13 [Hansen et al., 2011]

Feature	Altitude Relative to Limb (km)	Z_0 Altitude Relative to Jet Source (km)	FWHM (km)	Mach Number	Associated Tiger Stripe
a	21.3	21.6	7	6	Alexandria IV
b	22	24	9	—	Cairo V and/or VIII
c	28.4	29	10	5	Baghdad I
d	31.2	36	10	—	Baghdad VII
e	39	40	10	8	Damascus III
f	47.5	49.7	14	7	Damascus II

observed that the intensity is lower when ice grain particles are inserted (Case 4) with the optical depth reaching almost -0.6. This shows that there are more particles present in the plumes which does make sense physically as dsmcFoam adds the number densities of the different particles in the simulation. The addition of the number densities leads to more number of particles in the flow and lower optical depth. The shape of the curve (as discussed in section 8.2) also indicates that the jet is more collimated along the centerline of the plume. This can be confirmed as the optical depth is sharper when compared to Case 3 where the optical depth is spread over a small region around the centerline. In both cases, as the spacecraft moves away from the centerline, the optical depth increases indicating the number of particles gradually decreasing before stabilizing at around -0.2. Ideally, as the spacecraft moves away from the plumes the optical depth should reach zero or close to zero as the star behind the plumes would be visible clearly as observed in Figure 8.13.

Figure 8.15 also shows the optical depth of a single plume jet simulated with water gas particles and with and without ice grain particles at 25m altitude and an inlet flow velocity of (0 4000 0) m/s. As was the case with Figure 8.14, Case 6 with ice grain particles has a lower optical depth of -0.71 when compared to the flow with water gas particles only at an optical depth of -0.62. The rationale for this case is the same as the earlier case with more particles being present in the flow with ice grain particles as in dsmcFoam the particles get summed up leading to a higher particle count. Figure 8.15 indicates the presence of more particles in both cases as the higher velocity pushes more particles through the computational domain resulting in a lower optical depth when compared to Figure 8.14. While the shape of the optical depth for Case 4 and Case 6 are same with varying values, in Case 5, the flow with only water gas particles is significantly more collimated than Case 3. This difference is due to the velocity of the flow. Case 5 has a significantly higher velocity at 4000 m/s which leads to a highly collimated flow in the small 25m domain as compared to Case 3 at 902 m/s due to the lower velocity leads to more expansion and spreading of the flow around the centerline. This is evident as Cases 3 and 4 have a lower optical depth when the spacecraft moves away from the centerline indicating the presence of more particles when comparing to Cases 5 and 6 where the optical depth is close to zero.

The analysis from the occultation results of the DSMC simulation results provides more insights into the occultation observations made by the Cassini spacecraft as seen in Figure 8.13. Hansen et al. [2011] discusses that jets a, b, c and d in Figure 8.13 show an increased absorption of approximately 20%, indicating a higher gas density in the plumes. The occultation results obtained from Cases 4 and 6 as observed in Figure 8.14 and Figure 8.15 confirm that these jets contain a significantly higher number of particles (both waster gas and ice grain particles) when compared to jets e and f. As discussed earlier, Case 3 indicates that the flow is accelerating leading to a highly spread out flow over the domain which is visible in jets e and f in Figure 8.13. It can also be deduced that jet e has more particles than jet f due to a deeper peak which can be observed in the other cases. Jet f would be accelerating more the jet e due to the shallow peak which is characteristic of Case 3 in Figure 8.14.

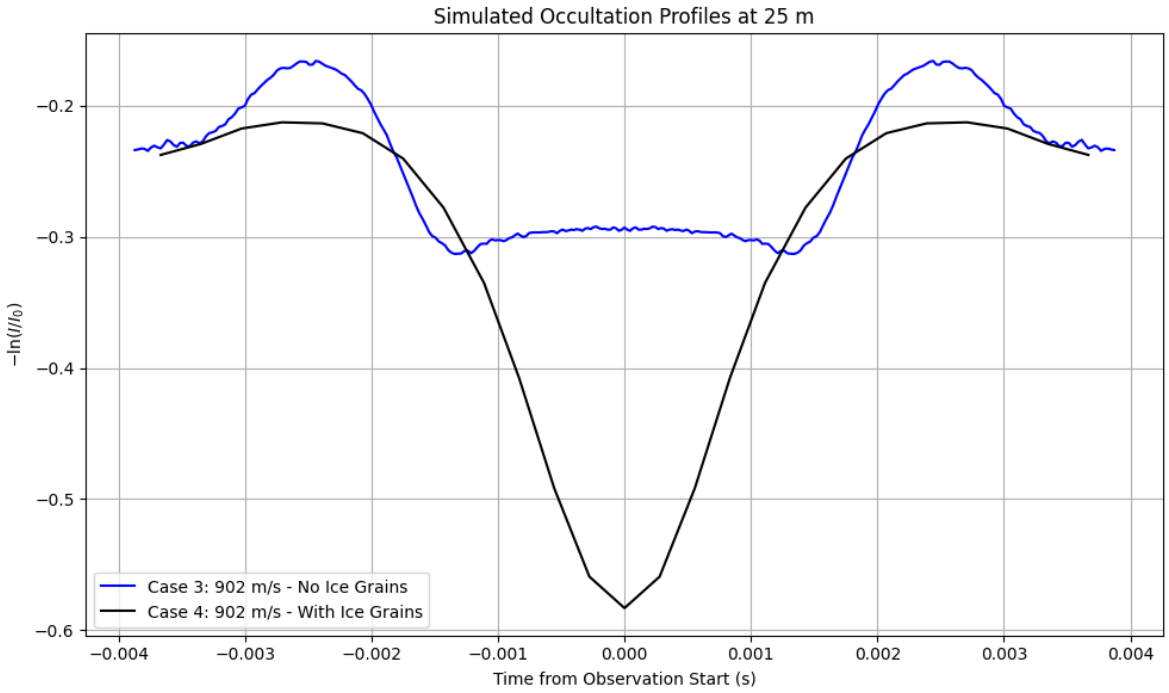

Figure 8.14: Optical Depth results at 25m altitude for (0 902 0) m/s inlet

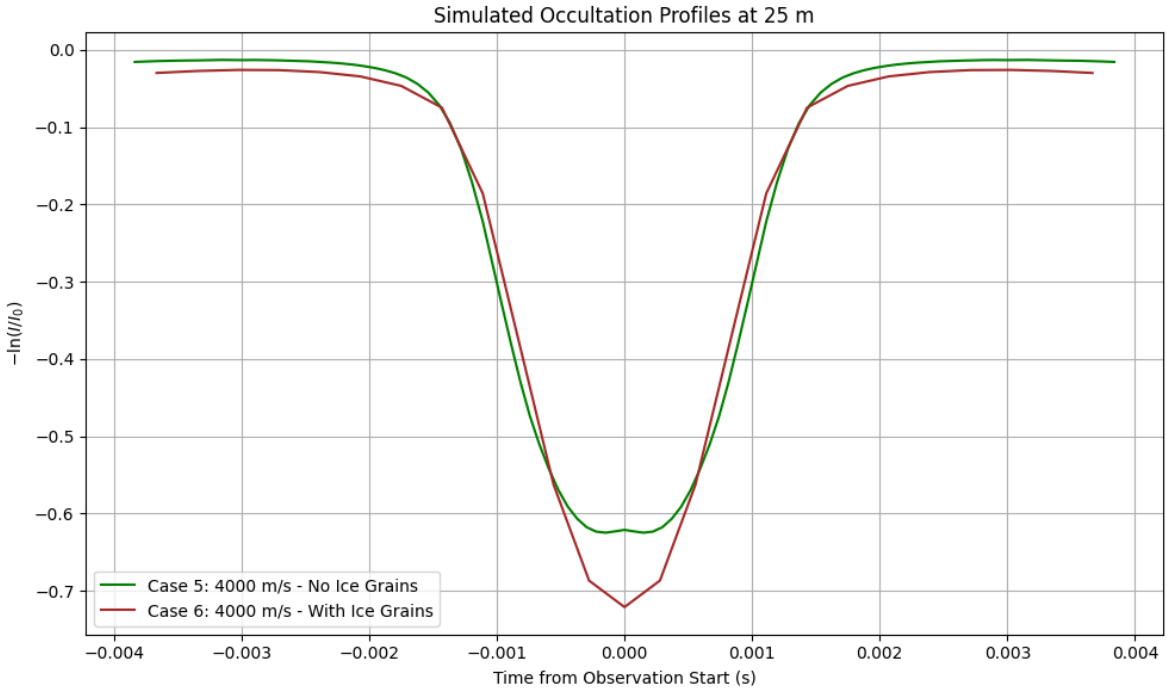

Figure 8.15: Optical Depth results at 25m altitude for (0 4000 0) m/s inlet

9

Conclusions and Recommendations

9.1. Conclusions

The main goal of this thesis was to understand if the plumes were accelerating by modeling them using an open source software like OpenFOAM so that these results can be used to further study and create more advanced models of the plumes. The models of these plumes would also help in better understanding the observations and data obtained by the Cassini spacecraft thus increasing the knowledge of Enceladus and its plumes even further.

Are the plumes accelerating?

No, the plumes are not accelerating as they expand from the surface to the altitude of the Cassini spacecraft. From the various results that were obtained by analyzing the flow of the plumes in various cases, the plumes are accelerating in the near field region of Enceladus. This is clearly visible when looking at individual particle velocities in the flow for all the cases in the near-field region where the flow of the plumes behave similar to that of an underexpanded nozzle. However, from the preliminary results and predictions of the far-field region that were obtained, the flow becomes free-molecular and the particle velocities reduce as they lose energy hence decelerating the flow.

How does the presence of ice grain particles influence the flow dynamics of the plumes?

From Cases 4 and 6, it is evident that the flow properties change significantly as discussed in the section 8.2. While the individual particle velocities do increase, the percentage of particles whose velocities increase were relatively lower when compared to cases with only water gas particles. This was mainly due to higher number of collisions occurring with the ice grain particles leading to a reduction in the velocities. This trend is visible for cases with inlet velocity of 902 m/a and 4000 m/s. The presence of ice grain particles also increased the pressure and translational temperature due to higher number of collisions taking place in the flow. This also impacted the number density of particles in the flow which was higher for both the cases. The presence of ice grain particles does not effect the individual particle velocities of the water gas particles

What are the key factors influencing the growth of ice grain particles?

The key factors influencing the growth of ice grain particles are the sticking coefficient and the properties of the flow around the ice grain particle. The influence of residence time is evident when looking at the growth of ice grain particles discussed in section 8.1 as the size of the particles continued to increase the longer the particles were in that cell. While residence time is not a factor as it is influenced by the properties of the flow around the ice grain particles, i.e., velocity, local number density and the mass of the water gas particles. Since the ice grain particles continue to spend more time in the flow, the size of the ice grain particles will continue to increase as they reach higher altitudes. However, the rate of growth will decrease as the number density and velocity of the particles decreases as the flow reaches higher altitudes. The influence of the sticking coefficient is another important factor as it determines the

probability of the surrounding water gas particles actually interacting and helping the ice grain particle grow. Based on literature, the sticking coefficient was taken to be 0.2. However, the growth of ice grain particles was also checked for higher sticking coefficients (results attached in Appendix C) and it showed a significantly higher grain growth, hence proving the impact of the sticking coefficient.

How do the numerical simulations compare to the Cassini data?

The numerical simulations provide an insight into the occultation observations made by the Cassini spacecraft. As discussed in section 8.4, the simulations helped in understanding which jets were accelerating or decelerating while also providing information about the presence of particles. The sharper, deeper peaks in the occultation data (Figure 8.13) showed that more particles were present in the flow which was also decelerating.

9.2. Recommendations

The current study provides an excellent base to further model and study the plumes for future research to improve the understanding of the plumes of Enceladus. While this thesis provides a baseline for future work, a number of assumptions and compromises were made to limit its scope and due to the computational limitations at hand.

During this thesis a critical assumption was made to reduce the computational time and decrease the complexity of the simulation, i.e., the surface next to the vent was not considered to be a wall. This was mainly done to remove any wall-particle interactions which helps in reducing the complexity of the simulations. For future work this avenue can be explored as it will provide better understanding into the deposition rate of the particles on the surface of Enceladus.

Several compromises were made during the course of this thesis to reduce to the computational time and power required as DSMC simulations are computationally expensive. Mesh resolution and cell size was one of the major trade-offs that was made in this thesis as the cell size in a mesh for a DSMC simulation should be less than the mean free path of the particles. This can be improved significantly by finding an optimal point through mesh convergence studies similar to the one performed in section 6.3. In this thesis, the number of equivalent particles per cell was maintained 20-25 particles per cell. This can be increased upto 50 particles per cell which would provide better results without increasing the statistical noise. However, a staged mesh could be used to accurately simulate the flow of particles which would reduce the computational effort required. Thus, the use of DSMC for simulating the plumes is only recommended if using a multi-staged mesh [Yeoh et al., 2015] upto altitudes of 15-20km.

It is however not recommended to use the dsmcFoam solver of OpenFOAM for further simulations and research as there is little to no documentation available on its workings. While the software is open source, the code being used by the solver is difficult to understand and very difficult to find in the source code with absolutely no documentation. It is recommended to use other open source DSMC solvers, like SPARTA which has a much wider user base and more extensive documentation than the dsmcFoam solver of OpenFOAM.

In this thesis, the plumes were modeled only using water gas and ice grain particles but in reality Cassini detected the presence of other species too which were discussed early on here. Modeling the plumes with other gases like CH_4, NH_3 and other organics could provide a better understanding of the chemical reactions and processes occurring within the plume while hopefully also providing insights into the subsurface ocean of Enceladus.

Due to the long computational time required by these simulations, this thesis was limited to a single vent geometry and two different exit velocities of the plumes. To understand the variability of the plumes, the model presented in this thesis can be modified for different vent geometries and initial conditions. This would allow for a wider range results that can be compared to the occultation observations while providing insights into how the vent geometries effect the occultation results.

One major limitation of DSMC simulations which has been discussed throughout this thesis is the influence of boundary conditions on the flow properties. The influence of the boundary conditions on the flow properties were clearly visible in the 25m x 25m domain. It would be recommended to increase it to an extent where this influence can be negated to get less noisy results. For example, for the 25m

x 25m domain, the x-axis can be increased to 200m which would significantly reduce the impact of the boundary conditions on the flow.

Taking all these recommendations into consideration, this thesis provides a strong foundation for future research to model the plumes of Enceladus and understand the physics even better.

Bibliography

O. Abramov and J. R. Spencer. Endogenic heat from enceladus' south polar fractures: New observations, and models of conductive surface heating. *Icarus*, 199(1):189–196, 2009.

C. Airiau. *High fidelity numerical simulation of a confined flow around a capsule in a dense, diluted and rarefied air*. PhD thesis, Institut de Mécanique des Fluides de Toulouse, 2022.

J. D. Anderson. Modern compressible flow: with historical perspective. *(No Title)*, 1990.

G. A. Bird. *The DSMC method*. [CreateSpace], 2013. ISBN 9781492112907.

R. H. Brown, R. N. Clark, B. J. Buratti, D. P. Cruikshank, J. W. Barnes, R. M. Mastrapa, J. Bauer, S. Newman, T. Momary, K. H. Baines, et al. Composition and physical properties of enceladus' surface. *Science*, 311(5766):1425–1428, 2006.

A. B. Carlson and G. A. Bird. Implementation of a vibrationally linked chemical reaction model for dsmc. Technical report, 1994.

G. D. Crawford and D. J. Stevenson. Gas-driven water volcanism and the resurfacing of europa. *Icarus*, 73(1):66–79, 1988.

R. Dhariwal, R. Kumar, D. A. Levin, D. B. Goldstein, P. L. Varghese, and L. M. Trafton. Modeling and simulation of near-field enceladus plumes from tiger stripe fractures using a collision-limiter condensation model. In *50th AIAA Aerospace Sciences Meeting Including the New Horizons Forum and Aerospace Exposition*, 2012. doi: 10.2514/6.2012-226.

Y. Dong, T. Hill, B. Teolis, B. Magee, and J. Waite. The water vapor plumes of enceladus. *Journal of Geophysical Research: Space Physics*, 116(A10), 2011.

M. Dougherty, K. Khurana, F. Neubauer, C. Russell, J. Saur, J. Leisner, and M. Burton. Identification of a dynamic atmosphere at enceladus with the cassini magnetometer. *Science*, 311(5766):1406–1409, 2006.

E. Franquet, V. Perrier, S. Gibout, and P. Bruel. Free underexpanded jets in a quiescent medium: A review. *Progress in Aerospace Sciences*, 77:25–53, 2015.

P. Gao, P. Kopparla, X. Zhang, and A. P. Ingersoll. Aggregate particles in the plumes of enceladus. *Icarus*, 264:227–238, 2016.

C. Greenshields. *OpenFOAM v12 User Guide*. The OpenFOAM Foundation, London, UK, 2024. URL `https://doc.cfd.direct/openfoam/user-guide-v12`.

C. Hansen, D. E. Shemansky, L. W. Esposito, A. Stewart, B. Lewis, J. Colwell, A. Hendrix, R. A. West, J. Waite Jr, B. Teolis, et al. The composition and structure of the enceladus plume. *Geophysical Research Letters*, 38(11), 2011.

C. J. Hansen, L. Esposito, A. Stewart, J. Colwell, A. Hendrix, W. Pryor, D. Shemansky, and R. West. Enceladus' water vapor plume. *Science*, 311(5766):1422–1425, 2006.

M. Hedman, P. Nicholson, M. Showalter, R. Brown, B. Buratti, and R. Clark. Spectral observations of the enceladus plume with cassini-vims. *The Astrophysical Journal*, 693(2):1749, 2009.

M. Hedman, C. Gosmeyer, P. Nicholson, C. Sotin, R. Brown, R. Clark, K. Baines, B. Buratti, and M. Showalter. An observed correlation between plume activity and tidal stresses on enceladus. *Nature*, 500(7461):182–184, 2013.

T. Hurford, P. Helfenstein, G. Hoppa, R. Greenberg, and B. Bills. Eruptions arising from tidally controlled periodic openings of rifts on enceladus. *Nature*, 447(7142):292–294, 2007.

A. P. Ingersoll and S. P. Ewald. Total particulate mass in enceladus plumes and mass of saturn's e ring inferred from cassini iss images. *Icarus*, 216(2):492–506, 2011.

A. P. Ingersoll and A. A. Pankine. Subsurface heat transfer on enceladus: Conditions under which melting occurs. *Icarus*, 206(2):594–607, 2010.

H. Jasak. Openfoam: Open source cfd in research and industry. *International journal of naval architecture and ocean engineering*, 1(2):89–94, 2009.

R. Jaumann, K. Stephan, G. B. Hansen, R. N. Clark, B. J. Buratti, R. H. Brown, K. H. Baines, S. F. Newman, G. Bellucci, G. Filacchione, A. Coradini, D. P. Cruikshank, C. A. Griffith, C. A. Hibbitts, T. B. McCord, R. M. Nelson, P. D. Nicholson, C. Sotin, and R. Wagner. Distribution of icy particles across enceladus' surface as derived from cassini-vims measurements. *Icarus*, 193:407–419, 2 2008. ISSN 00191035. doi: 10.1016/j.icarus.2007.09.013.

A. Kashkovsky, A. Kudryavtsev, and A. Shershnev. Numerical investigation of the rarefied supersonic underexpanded jet structure using the dsmc method. *Thermophysics and Aeromechanics*, 30(1): 29–36, 2023.

S. Kempf, U. Beckmann, and J. Schmidt. How the enceladus dust plume feeds saturn's e ring. *Icarus*, 206:446–457, 4 2010. ISSN 00191035. doi: 10.1016/j.icarus.2009.09.016.

S. W. Kieffer, X. Lu, G. McFarquhar, and K. H. Wohletz. A redetermination of the ice/vapor ratio of enceladus' plumes: Implications for sublimation and the lack of a liquid water reservoir. *Icarus*, 203 (1):238–241, 2009.

M. R. Kirchoff and P. Schenk. Crater modification and geologic activity in enceladus' heavily cratered plains: Evidence from the impact crater distribution. *Icarus*, 202(2):656–668, 2009.

E. S. Kite and A. M. Rubin. Sustained eruptions on enceladus explained by turbulent dissipation in tiger stripes. *Proceedings of the National Academy of Sciences of the United States of America*, 113: 3972–3975, 4 2016. ISSN 10916490. doi: 10.1073/pnas.1520507113.

Z. Li, R. Dhariwal, and D. A. Levin. Dsmc simulation of near-field enceladus plumes from tiger stripe fractures. In *44th AIAA Thermophysics Conference*, 2013. doi: 10.2514/6.2013-2787.

A. Mahieux, D. B. Goldstein, P. L. Varghese, and L. M. Trafton. Parametric study of water vapor and water ice particle plumes based on dsmc calculations: Application to the enceladus geysers. *Icarus*, 319:729–744, 2 2019. ISSN 10902643. doi: 10.1016/j.icarus.2018.10.022.

D. L. Matson, J. C. Castillo-Rogez, A. G. Davies, and T. V. Johnson. Enceladus: A hypothesis for bringing both heat and chemicals to the surface. *Icarus*, 221:53–62, 9 2012. ISSN 00191035. doi: 10.1016/j.icarus.2012.05.031.

P. Meier, U. Motschmann, J. Schmidt, F. Spahn, T. W. Hill, Y. Dong, G. H. Jones, and H. Kriegel. Modeling the total dust production of enceladus from stochastic charge equilibrium and simulations. *Planetary and Space Science*, 119:208–221, 12 2015. ISSN 00320633. doi: 10.1016/j.pss.2015.10.002.

M. Nakajima and A. P. Ingersoll. Controlled boiling on enceladus. 1. model of the vapor-driven jets. *Icarus*, 272:309–318, 7 2016. ISSN 10902643. doi: 10.1016/j.icarus.2016.02.027.

NASA/JPL. Saturn rings, 2005. URL `https://science.nasa.gov/resource/saturns-rings-2/`.

S. F. Newman, B. J. Buratti, R. H. Brown, R. Jaumann, J. Bauer, and T. Momary. Photometric and spectral analysis of the distribution of crystalline and amorphous ices on enceladus as seen by cassini. *Icarus*, 193:397–406, 2 2008. ISSN 00191035. doi: 10.1016/j.icarus.2007.04.019.

F. Nimmo, J. Spencer, R. Pappalardo, and M. Mullen. Shear heating as the origin of the plumes and heat flux on enceladus. *Nature*, 447(7142):289–291, 2007.

C. Porco, D. DiNino, and F. Nimmo. How the geysers, tidal stresses, and thermal emission across the south polar terrain of enceladus are related. *The Astronomical Journal*, 148(3):45, 2014.

C. C. Porco, P. Helfenstein, P. Thomas, A. Ingersoll, J. Wisdom, R. West, G. Neukum, T. Denk, R. Wagner, T. Roatsch, et al. Cassini observes the active south pole of enceladus. *science*, 311(5766): 1393–1401, 2006.

F. Postberg, S. Kempf, J. Schmidt, N. Brilliantov, A. Beinsen, B. Abel, U. Buck, and R. Srama. Sodium salts in e-ring ice grains from an ocean below the surface of enceladus. *Nature*, 459(7250):1098–1101, 2009.

F. Postberg, J. Schmidt, J. Hillier, S. Kempf, and R. Srama. A salt-water reservoir as the source of a compositionally stratified plume on enceladus. *Nature*, 474(7353):620–622, 2011.

F. Postberg, R. N. Clark, C. J. Hansen, A. J. Coates, C. M. Dalle Ore, F. Scipioni, M. M. Hedman, and J. H. Waite. Plume and surface composition of enceladus. *Enceladus and the icy moons of Saturn*, 129, 2018.

M. Rubin, V. M. Tenishev, M. R. Combi, K. C. Hansen, T. I. Gombosi, K. Altwegg, and H. Balsiger. Monte carlo modeling of neutral gas and dust in the coma of comet 1p/halley. *Icarus*, 213(2):655–677, 2011.

T. Scanlon, E. Roohi, C. White, M. Darbandi, and J. Reese. An open source, parallel dsmc code for rarefied gas flows in arbitrary geometries. *Computers & Fluids*, 39(10):2078–2089, 2010.

P. Schenk, R. Clark, C. Howett, A. Verbiscer, and J. Waite. *Enceladus and the Icy Moons of Saturn*. The University of Arizona Space Science Series. University of Arizona Press, 2018. ISBN 9780816537075. URL `https://books.google.nl/books?id=7cFwDwAAQBAJ`.

J. Schmidt, N. Brilliantov, F. Spahn, and S. Kempf. Slow dust in enceladus' plume from condensation and wall collisions in tiger stripe fractures. *Nature*, 451(7179):685–688, 2008.

J. Spencer, J. Pearl, M. Segura, F. Flasar, A. Mamoutkine, P. Romani, B. Buratti, A. Hendrix, L. Spilker, and R. Lopes. Cassini encounters enceladus: Background and the discovery of a south polar hot spot. *science*, 311(5766):1401–1405, 2006.

J. Spencer, F. Nimmo, A. P. Ingersoll, T. Hurford, E. Kite, A. Rhoden, J. Schmidt, and C. Howett. Plume origins and plumbing: from ocean to surface. *Enceladus and the icy moons of Saturn*, 163, 2018.

J. R. Spencer and F. Nimmo. Enceladus: An active ice world in the saturn system. *Annual Review of Earth and Planetary Sciences*, 41:693–717, 5 2013. ISSN 00846597. doi: 10.1146/annurev-earth-050212-124025.

V. Tenishev, M. R. Combi, B. D. Teolis, and J. H. Waite. An approach to numerical simulation of the gas distribution in the atmosphere of enceladus. *Journal of Geophysical Research: Space Physics*, 115, 2010. ISSN 21699402. doi: 10.1029/2009JA015223.

V. Tenishev, M. R. Combi, and M. Rubin. Numerical simulation of dust in a cometary coma: Application to comet 67p/churyumov-gerasimenko. *The Astrophysical Journal*, 732(2):104, 2011.

B. D. Teolis, M. E. Perry, C. J. Hansen, J. H. Waite, C. C. Porco, J. R. Spencer, and C. J. Howett. Enceladus plume structure and time variability: Comparison of cassini observations. *Astrobiology*, 17:926–940, 9 2017. ISSN 15311074. doi: 10.1089/ast.2017.1647.

E. V. Titov and D. A. Levin. Extension of the dsmc method to high pressure flows. *International Journal of Computational Fluid Dynamics*, 21(9-10):351–368, 2007.

O. J. Tucker, M. R. Combi, and V. M. Tenishev. 2d models of gas flow and ice grain acceleration in enceladus' vents using dsmc methods. *Icarus*, 257:362–376, 9 2015. ISSN 10902643. doi: 10.1016/j.icarus.2015.05.012.

K. Viswanath, K. Brentner, S. Gimelshein, and D. Levin. Investigation of soot combustion in underexpanded jet plume flows. *Journal of thermophysics and heat transfer*, 19(3):282–293, 2005.

W. Wagner. A convergence proof for bird's direct simulation monte carlo method for the boltzmann equation. *Journal of Statistical Physics*, 66:1011–1044, 1992.

J. H. Waite, C. R. Glein, R. S. Perryman, B. D. Teolis, B. A. Magee, G. Miller, J. Grimes, M. E. Perry, K. E. Miller, A. Bouquet, et al. Cassini finds molecular hydrogen in the enceladus plume: evidence for hydrothermal processes. *Science*, 356(6334):155–159, 2017.

J. H. Waite Jr, M. R. Combi, W.-H. Ip, T. E. Cravens, R. L. McNutt Jr, W. Kasprzak, R. Yelle, J. Luhmann, H. Niemann, D. Gell, et al. Cassini ion and neutral mass spectrometer: Enceladus plume composition and structure. *science*, 311(5766):1419–1422, 2006.

J. H. Waite Jr, W. Lewis, B. Magee, J. Lunine, W. McKinnon, C. Glein, O. Mousis, D. Young, T. Brockwell, J. Westlake, et al. Liquid water on enceladus from observations of ammonia and 40ar in the plume. *Nature*, 460(7254):487–490, 2009.

S. K. Yeoh, T. A. Chapman, D. B. Goldstein, P. L. Varghese, and L. M. Trafton. On understanding the physics of the enceladus south polar plume via numerical simulation. *Icarus*, 253:205–222, 6 2015. ISSN 10902643. doi: 10.1016/j.icarus.2015.02.020.

S. K. Yeoh, Z. Li, D. B. Goldstein, P. L. Varghese, D. A. Levin, and L. M. Trafton. Constraining the enceladus plume using numerical simulation and cassini data. *Icarus*, 281:357–378, 1 2017. ISSN 10902643. doi: 10.1016/j.icarus.2016.08.028.

A

Results for Cases 3a, 3b and 3c

A.1. Case 3a

Table A.1: Initial conditions for Case 3a

Parameters	**Value**
Number densities	H_2O - 1.1417x10^{21} m^{-3}
Flow Temperature	53 K
Flow Velocity	(0 902 0) m/s
Collisional Model	Variable Hard Sphere Model
Number of Cells	6375 cells
Number of equivalent particles	4.4598x10^{16}
Time step (ΔT)	5.4258x10^{-6} seconds

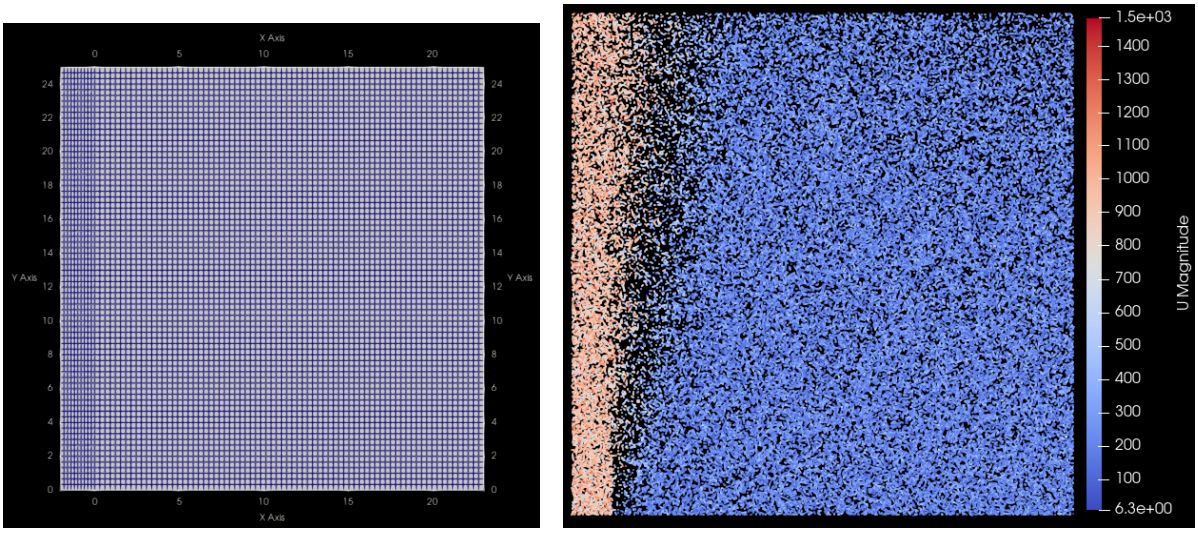

(a) Mesh resolution for Case 3a

(b) Particle velocities for Case 3a

Figure A.1: Mesh and particle velocity details for Case 3a

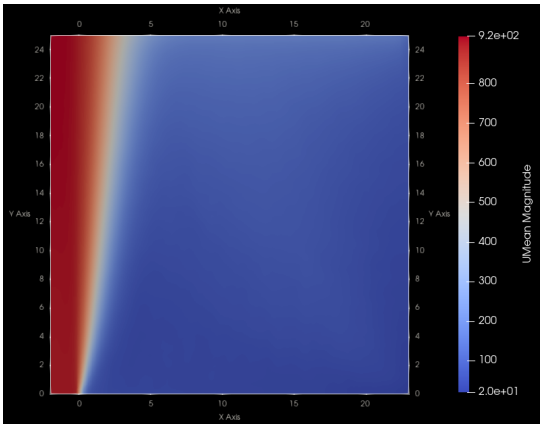

(a) Mean velocity contour for Case 3a

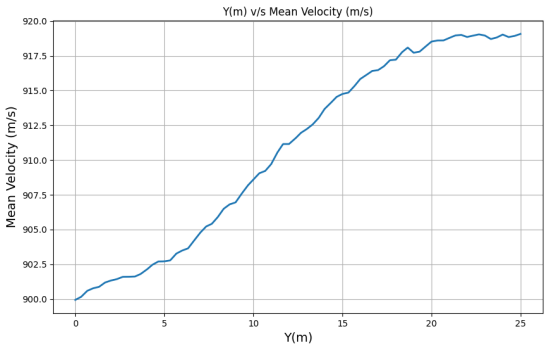

(b) Mean velocity distribution for Case 3a

Figure A.2: Mean velocity details for Case 3a

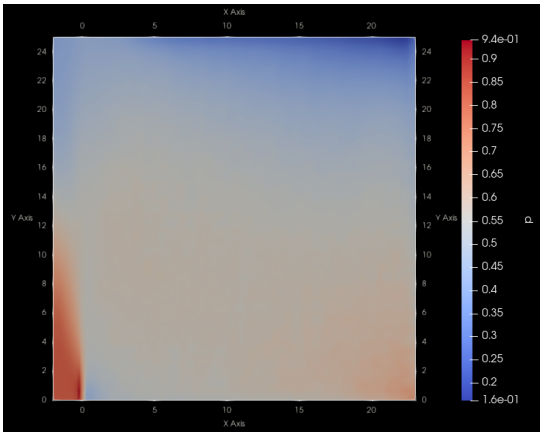

(a) Pressure contour for Case 3a

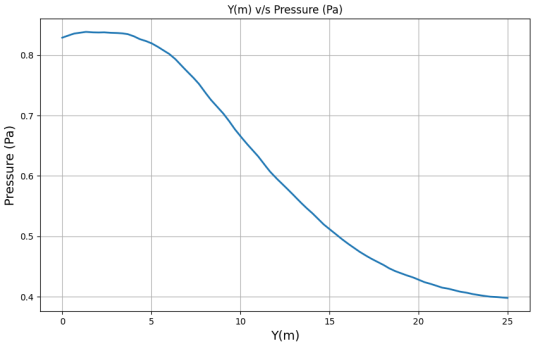

(b) Pressure distribution for Case 3a

Figure A.3: Pressure details for Case 3a

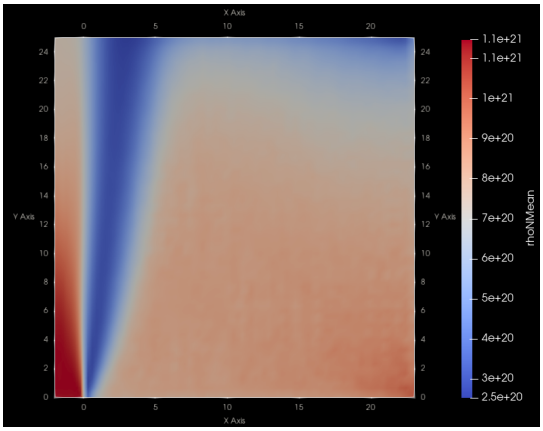

(a) Mean number density contour for Case 3a

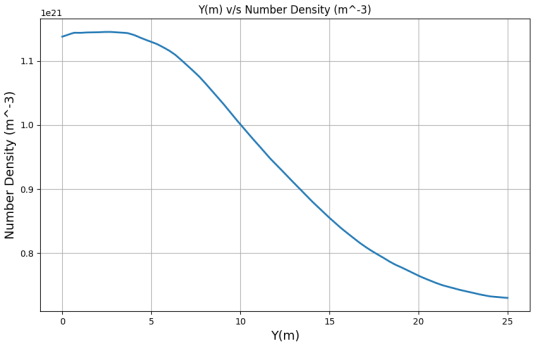

(b) Mean number density distribution for Case 3a

Figure A.4: Mean number density details for Case 3a

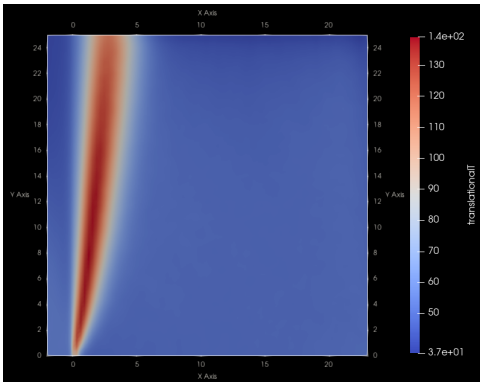

(a) Translational temperature contour for Case 3a

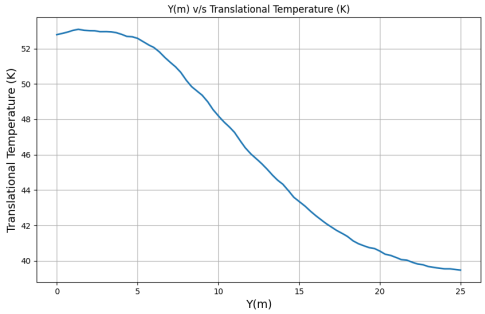

(b) Translational temperature distribution for Case 3a

Figure A.5: Translational temperature details for Case 3a

A.2. Case 3b

Table A.2: Initial conditions for Case 3b

Parameters	**Value**
Number densities	H_2O - 1.1417x10^{21} m^{-3}
Flow Temperature	53 K
Flow Velocity	(0 902 0) m/s
Collisional Model	Variable Hard Sphere Model
Number of Cells	11000 cells
Number of equivalent particles	4.4598x10^{16}
Time step (ΔT)	5.4258x10^{-6} seconds

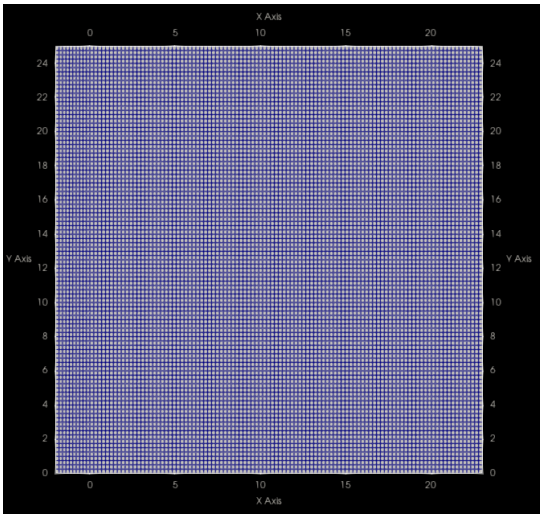

(a) Mesh resolution for Case 3b

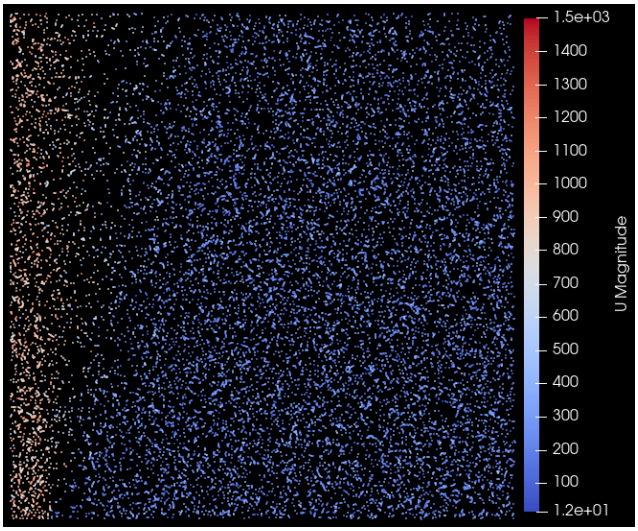

(b) Particle velocities for Case 3b

Figure A.6: Mesh and particle velocity details for Case 3b

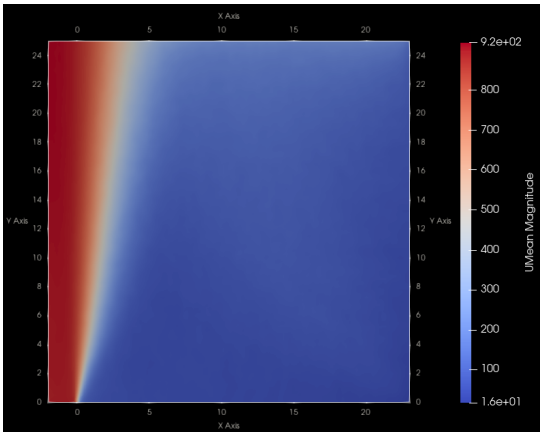

(a) Mean velocity contour for Case 3b

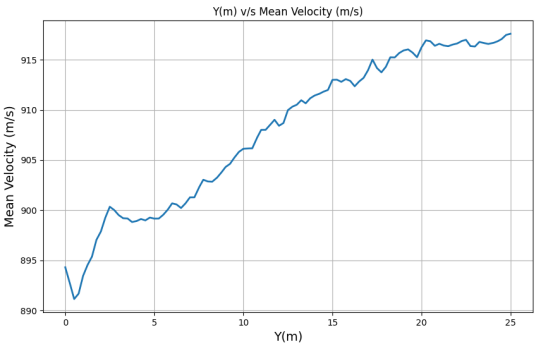

(b) Mean velocity distribution for Case 3b

Figure A.7: Mean velocity details for Case 3

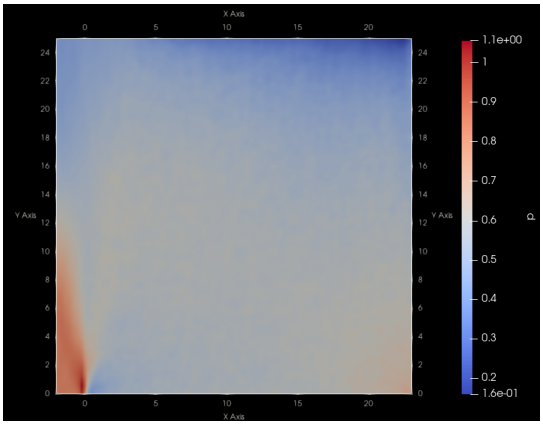

(a) Pressure contour for Case 3b

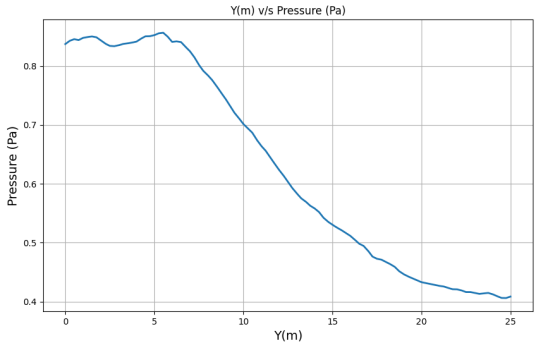

(b) Pressure distribution for Case 3b

Figure A.8: Pressure details for Case 3b

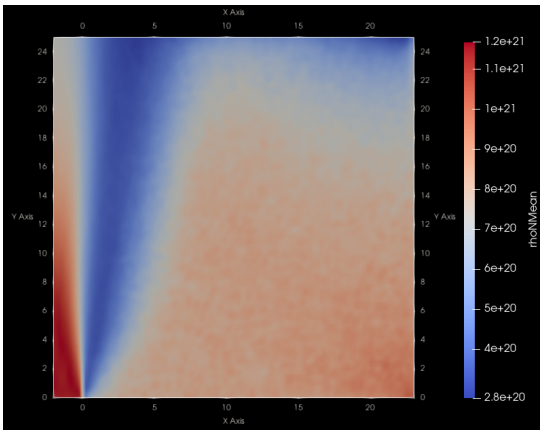

(a) Mean number density contour for Case 3b

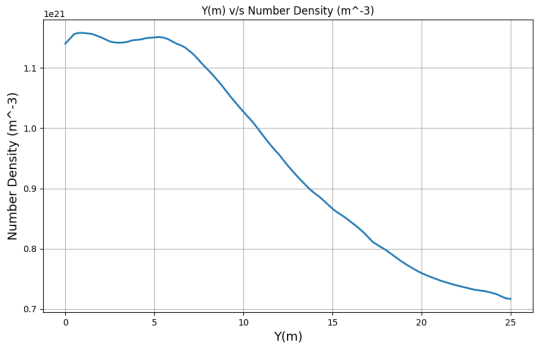

(b) Mean number density distribution for Case 3b

Figure A.9: Mean number density details for Case 3b

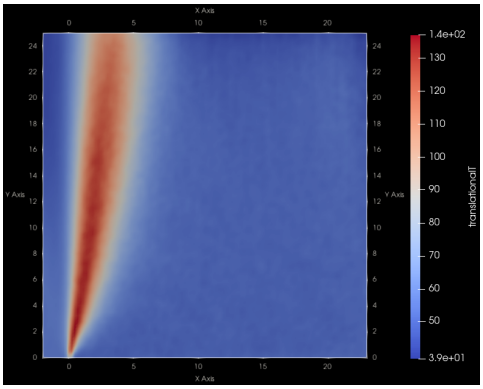

(a) Translational temperature contour for Case 3b

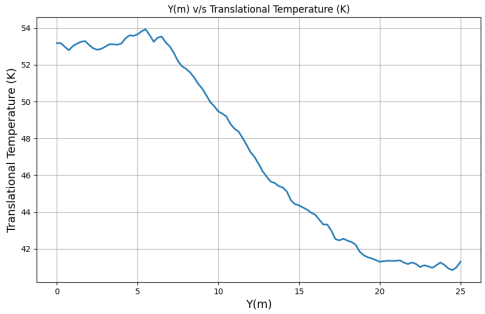

(b) Translational temperature distribution for Case 3b

Figure A.10: Translational temperature details for Case 3b

A.3. Case 3c

Table A.3: Initial conditions for Case 3c

Parameters	**Value**
Number densities	H_2O - 1.1417x10^{21} m^{-3}
Flow Temperature	53 K
Flow Velocity	(0 902 0) m/s
Collisional Model	Variable Hard Sphere Model
Number of Cells	44000 cells
Number of equivalent particles	4.4598x10^{16}
Time step (ΔT)	5.4258x10^{-6} seconds

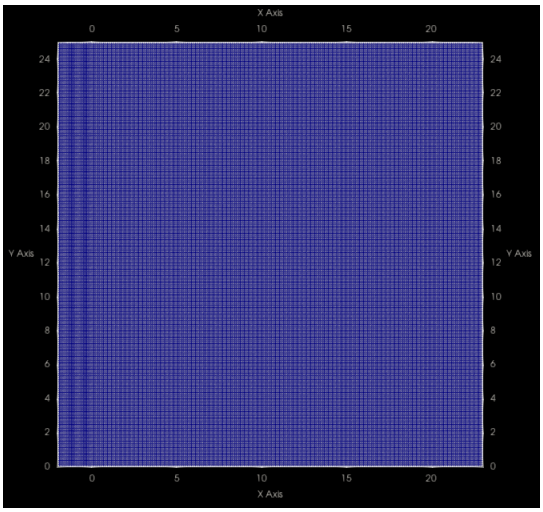

(a) Mesh resolution for Case 3c

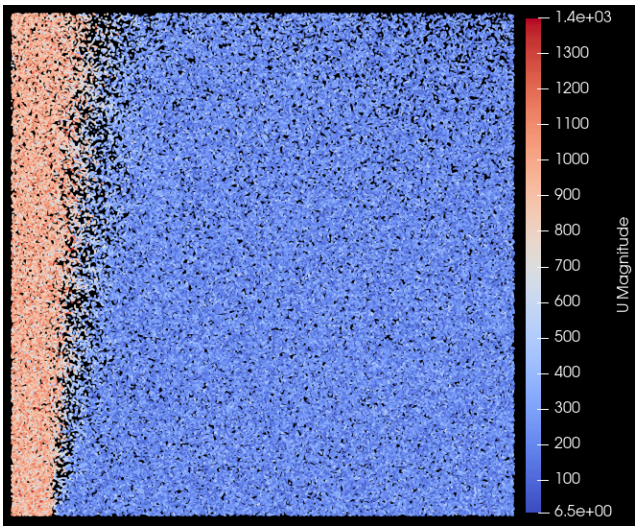

(b) Particle velocities for Case 3c

Figure A.11: Mesh and particle velocity details for Case 3c

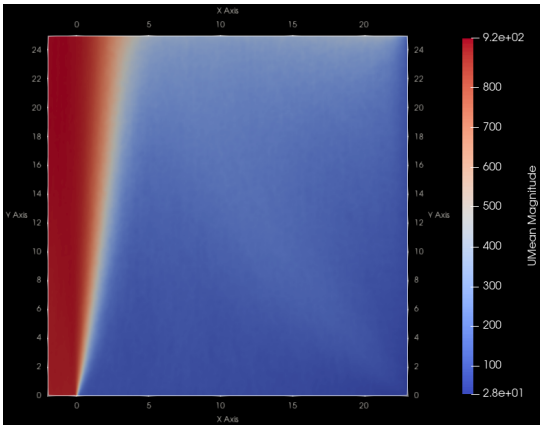

(a) Mean velocity contour for Case 3c

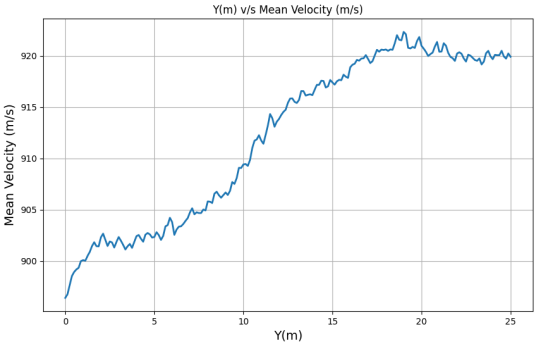

(b) Mean velocity distribution for Case 3c

Figure A.12: Mean velocity details for Case 3c

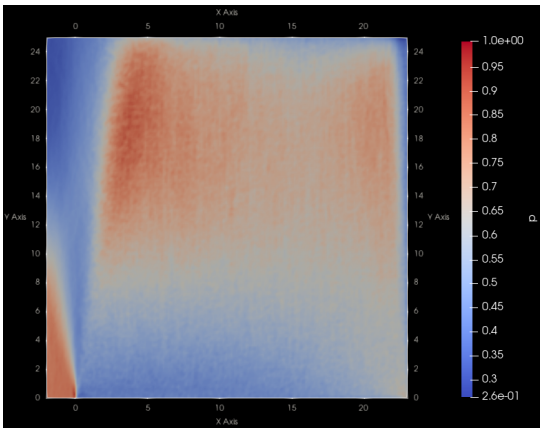

(a) Pressure contour for Case 3c

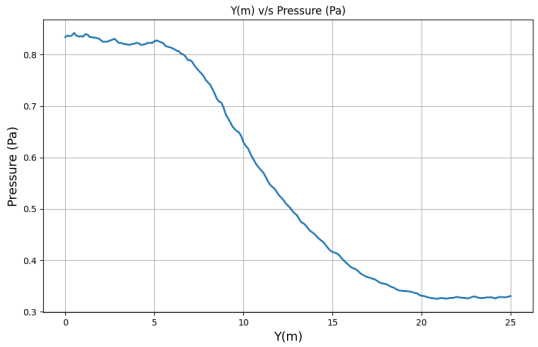

(b) Pressure distribution for Case 3c

Figure A.13: Pressure details for Case 3c

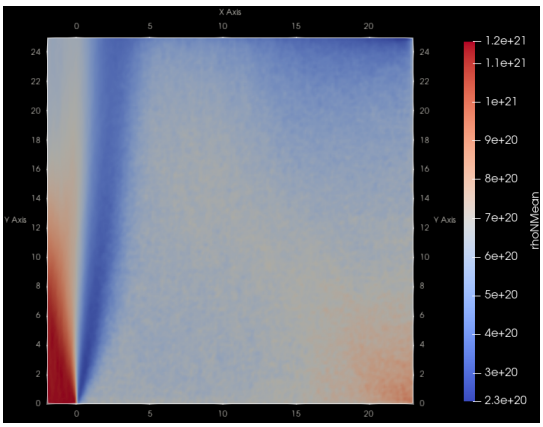

(a) Mean number density contour for Case 3c

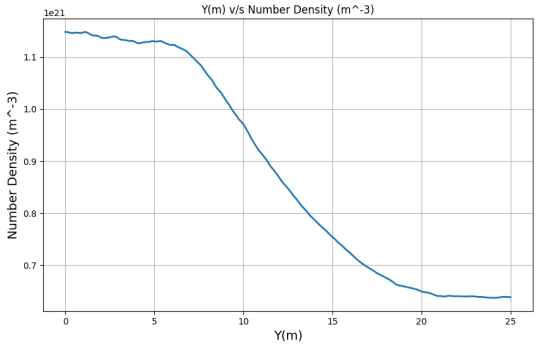

(b) Mean number density distribution for Case 3c

Figure A.14: Mean number density details for Case 3c

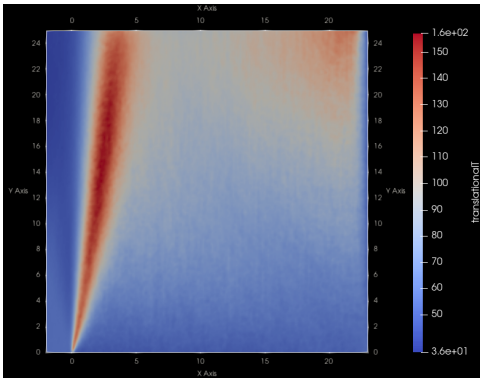

(a) Translational temperature contour for Case 3c

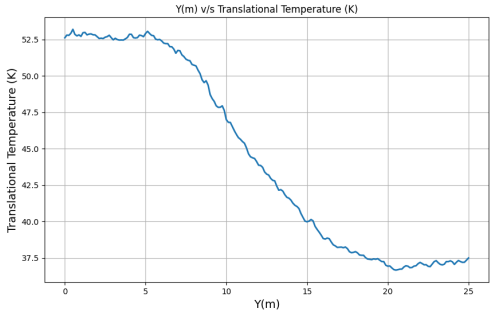

(b) Translational temperature distribution for Case 3c

Figure A.15: Translational temperature details for Case 3c

B

Far-Field Region Results (Case 7)

In this case, the computational domain size is increased to 60km x 60km. While the cell size is not less than the mean free path of particles and it may not optimally capture the physics it does provide a good preliminary results based on the mesh convergence analsis performed in section 6.3. This domain size covers some of the fly-bys made by the Cassini spacecraft allowing for a better analysis and comparison of the data obtained. The boundary and initial conditions of this case are illustrated in Figure B.1 and Table B.1.

Table B.1: Initial conditions for Case 7

Parameters	**Value**
Computational Domain Size	60km x 60km
Number densities	H_2O - 1.1417x10^{21}m^{-3}
Flow Temperature	53 K
Flow Velocity	(0 4000 0) m/s
Collisional Model	Variable Hard Sphere Model
Number of Cells	14000 cells
Number of equivalent particles	4.4598x10^{16}
Time step (ΔT)	5.4258x10^{-6}s

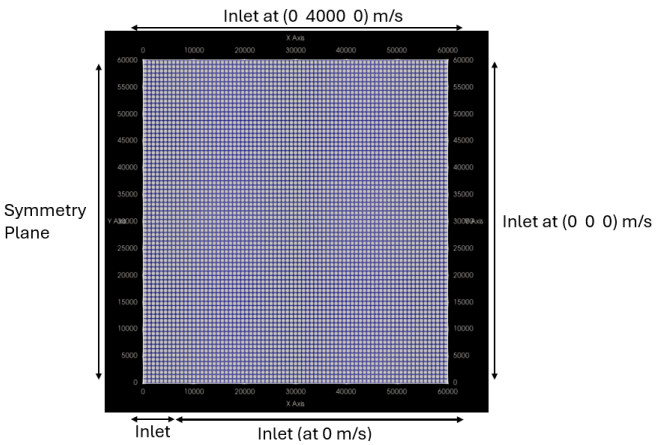

Figure B.1: Boundary conditions and mesh for Case 7

When looking at Figure B.2b, there is a significant difference in the inlet velocity defined at (0 4000 0)m/s in Table B.1 decreases to around 1000m/s. The size of the cell is very large =$600m$, which is four orders of magnitude larger than the mean free path of 0.01m. This leads to statistical noise and undersampling as creating a mesh with a cell size of 10m would require over 36 million cells and running the simulation over such a large domain would be impossible. However, considering the results obtained in this case, it is observed that mean velocity increases from the surface at 1000m/s to around 3500m/s at 35km before gradually decreasing to around 2500m/s at 60km altitude. This is a massive increase in the mean velocity and it may provide preliminary insights that the flow is accelerating. These insights are preliminary as the mesh will need to have smaller cell sizes to accurately capture the flow features.

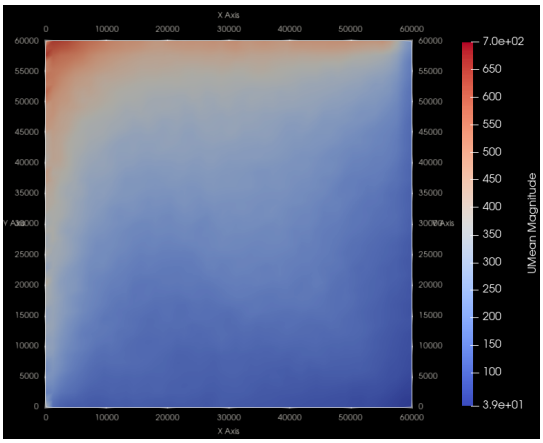

(a) Mean velocity contour for Case 7

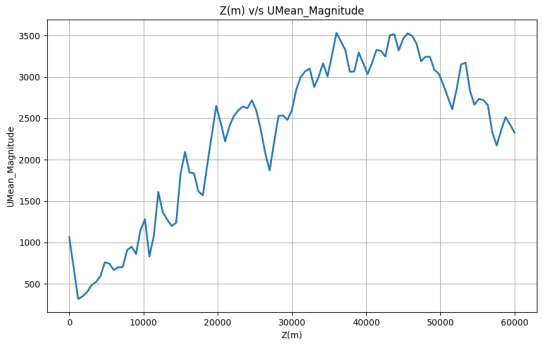

(b) Mean velocity distribution for Case 7

Figure B.2: Mean velocity details of Case 7

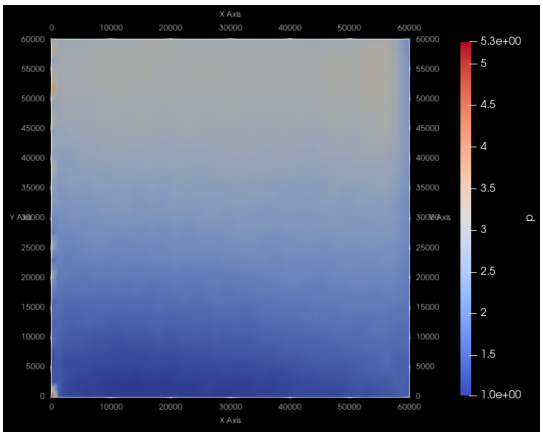

(a) Pressure contour for Case 7

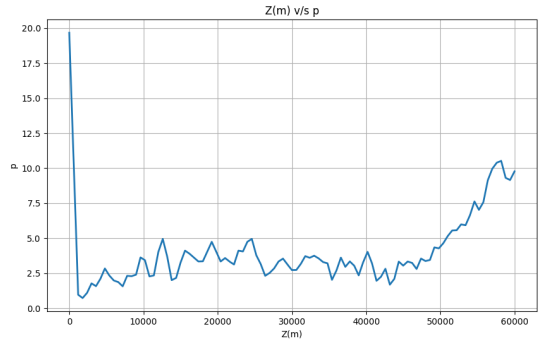

(b) Pressure distribution for Case 7

Figure B.3: Pressure details of Case 7

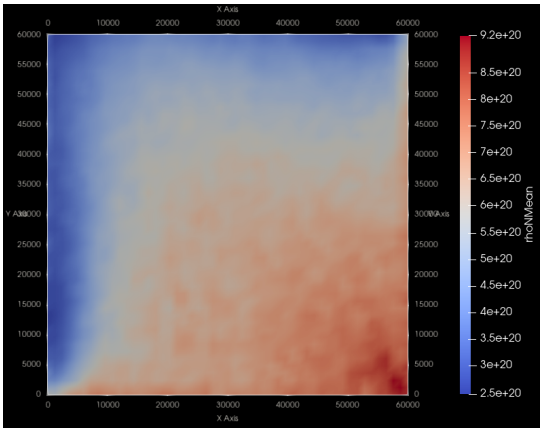

(a) Mean number density contour for Case 7

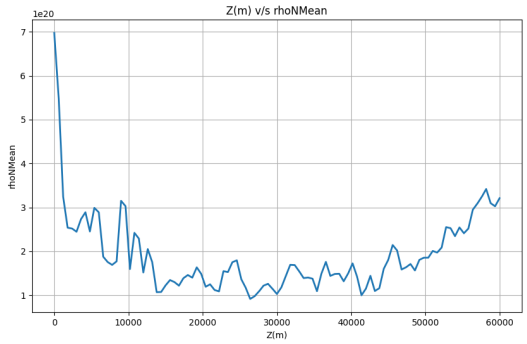

(b) Mean number density distribution for Case 7

Figure B.4: Mean number density details of Case 7

The pressure and number density profiles shown in Figure B.3 and Figure B.4 are the most definitive indicators of the structure of the plumes in the far-field region. It can be observed that both parameters illustrate a rapid initial drop from the high-pressure vent region as the plumes expand into near-vacuum conditions. After the drop, the values of both parameters stabilize but continue to show fluctuations due to statistical noise as it indicates that the collisions have started declining and the flow is transitioning to a free-molecular flow regime. When observing the mean number density profile it can be observed that while the flow remained in the continuum flow regime, it followed the pressure profile as according to Equation 6.1, pressure is directly proportional to the number density but this changes after the flow transitions into the free molecular flow regime the flow stabilizes in the range of 1x10^{20} - 2x10^{20} m^{-3} with slightly more statistical noise in the last 10km.

Like mean number density, the translational temperature profile, as observed in Figure B.5b, also follows Equation 6.1 in the continuum flow regime in the first few kilometers as pressure is also directly proportional to the temperature before increasing in the far-field region as the flow transitions to a free molecular flow regime. At the inlet, the temperature also rises rapidly to over 1000K due to the conversion of internal energy to kinetic energy due to the injection of particles into the flow. The increase in temperature after the initial drop stabilizes for temperatures int he range of 1500K - 2200K upto 30km where there remaining intermolecular collisions were occurring. As the flow develops downstream, there are still fluctuations as the particles have very less to no collisions taking place due to statistical error of the large cell sizes which leads to overestimation of the translational temperature values.

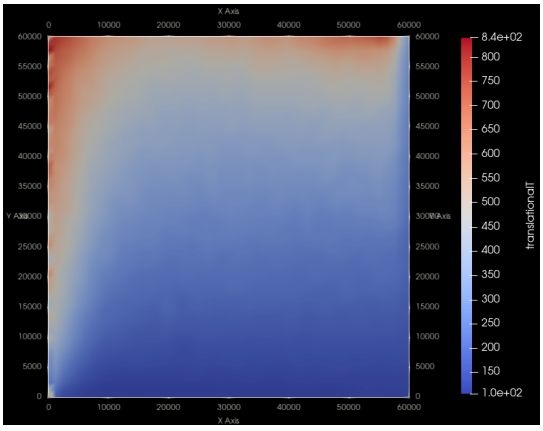

(a) Translational temperature contour for Case 7

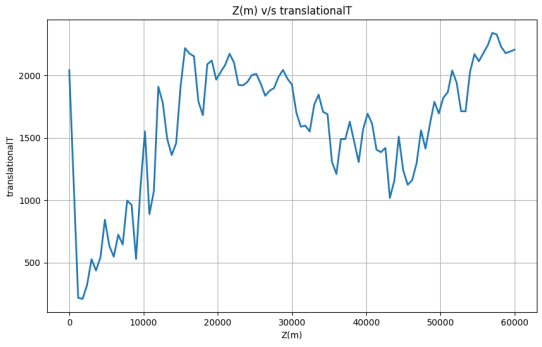

(b) Translational temperature distribution for Case 7

Figure B.5: Translational temperature details of Case 7

C

Growth of Ice Grain Particles

Ice grain growth for Case 4

For q = 0.35

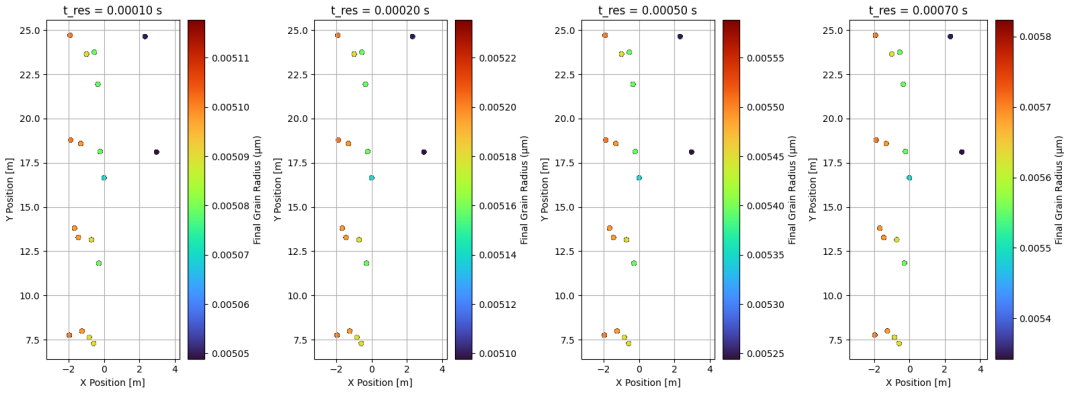

(a) t_{res} = 1x10^{-4} seconds **(b)** t_{res} = 2x10^{-4} seconds **(c)** t_{res} = 5x10^{-4} seconds **(d)** t_{res} = 7x10^{-4} seconds

Figure C.1: Growth of ice grain particles in Case 4 for q = 0.35 for different residence times

For q = 0.50

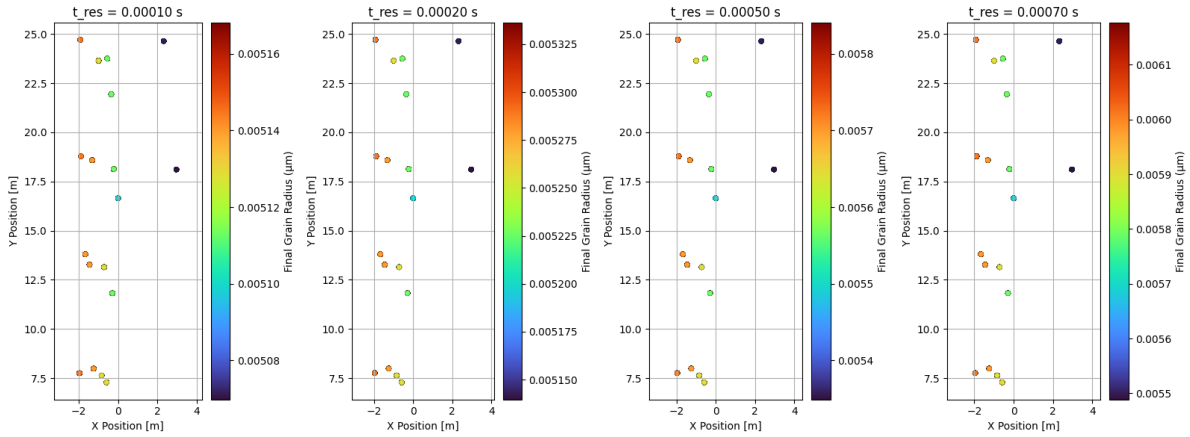

(a) t_{res} = 1x10^{-4} seconds **(b)** t_{res} = 2x10^{-4} seconds **(c)** t_{res} = 5x10^{-4} seconds **(d)** t_{res} = 7x10^{-4} seconds

Figure C.2: Growth of ice grain particles in Case 4 for q = 0.50 for different residence times

For q = 0.75

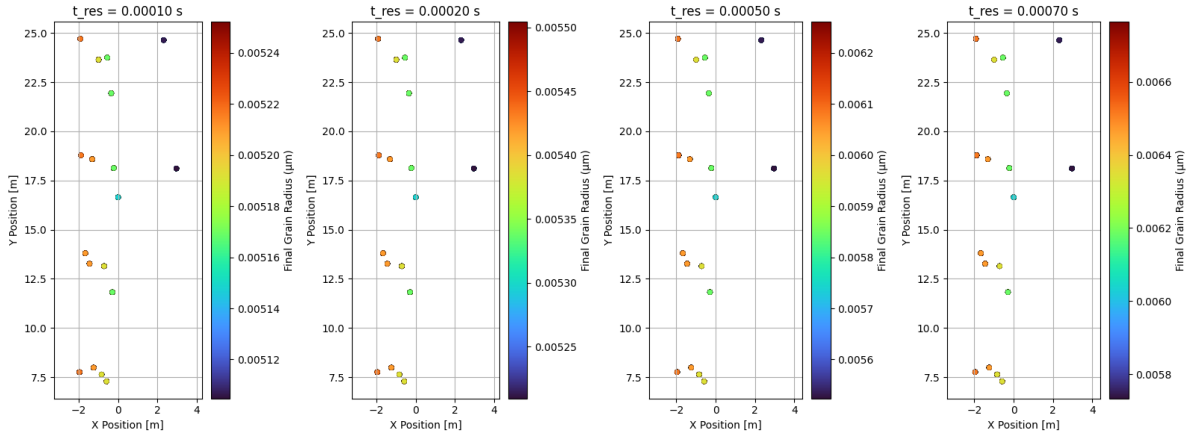

(a) t_{res} = 1x10^{-4} seconds **(b)** t_{res} = 2x10^{-4} seconds **(c)** t_{res} = 5x10^{-4} seconds **(d)** t_{res} = 7x10^{-4} seconds

Figure C.3: Growth of ice grain particles in Case 4 for q = 0.75 for different residence times

For q = 1.00

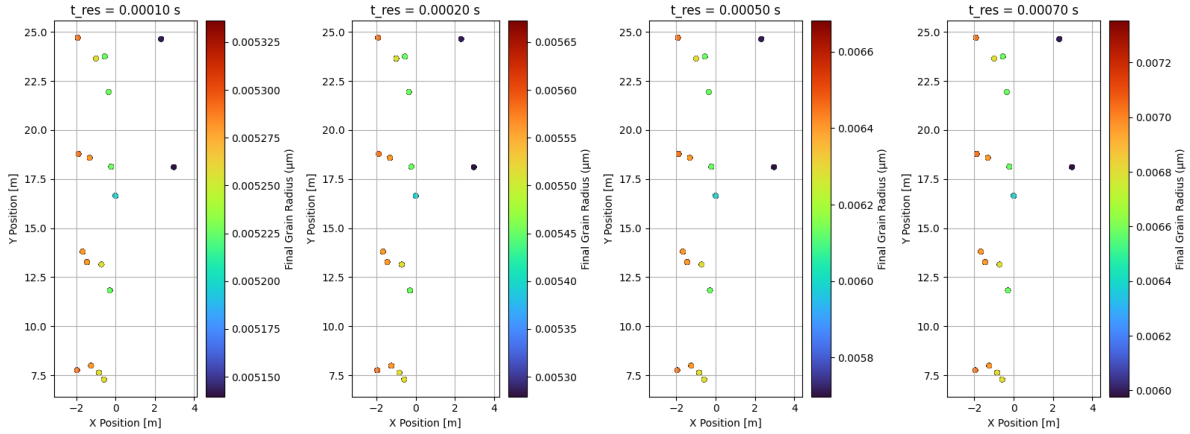

(a) t_{res} = 1x10^{-4} seconds **(b)** t_{res} = 2x10^{-4} seconds **(c)** t_{res} = 5x10^{-4} seconds **(d)** t_{res} = 7x10^{-4} seconds

Figure C.4: Growth of ice grain particles in Case 4 for q = 1.00 for different residence times

Ice grain growth for Case 6

For q = 0.35

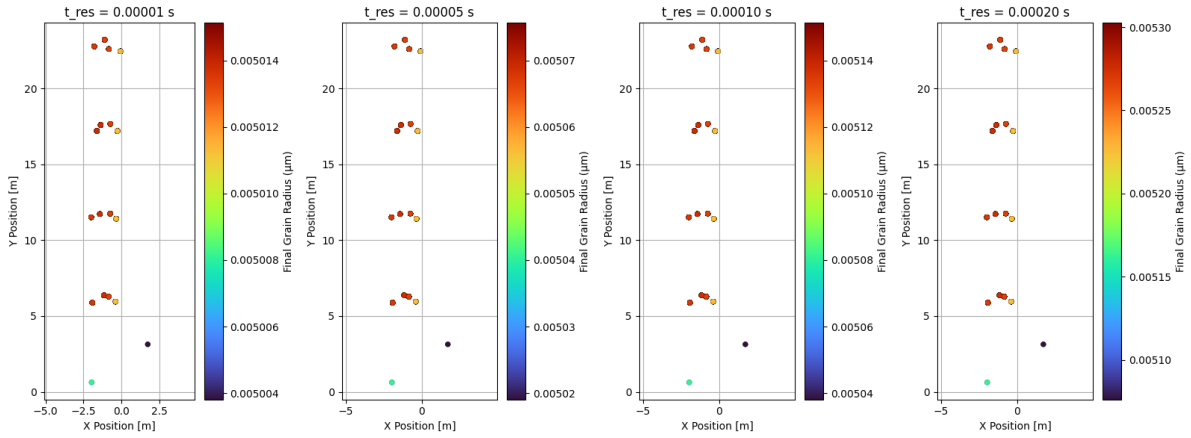

(a) t_{res} = 0.1x10^{-4} seconds **(b)** t_{res} = 0.5x10^{-4} seconds **(c)** t_{res} = 1x10^{-4} seconds **(d)** t_{res} = 2x10^{-4} seconds

Figure C.5: Growth of ice grain particles in Case 6 for q = 0.35 for different residence times

For q = 0.50

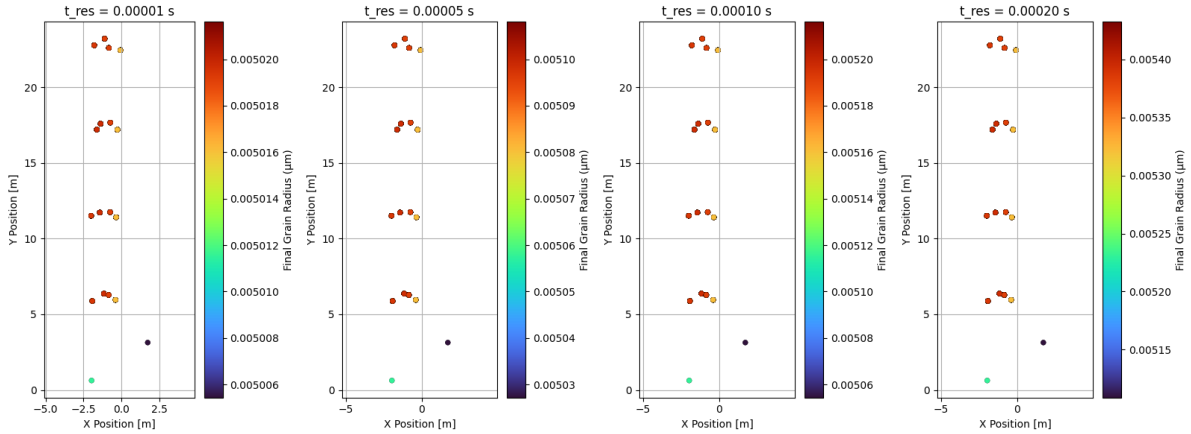

(a) t_{res} = 0.1x10^{-4} seconds **(b)** t_{res} = 0.5x10^{-4} seconds **(c)** t_{res} = 1x10^{-4} seconds **(d)** t_{res} = 2x10^{-4} seconds

Figure C.6: Growth of ice grain particles in Case 6 for q = 0.5 for different residence times

For q = 0.75

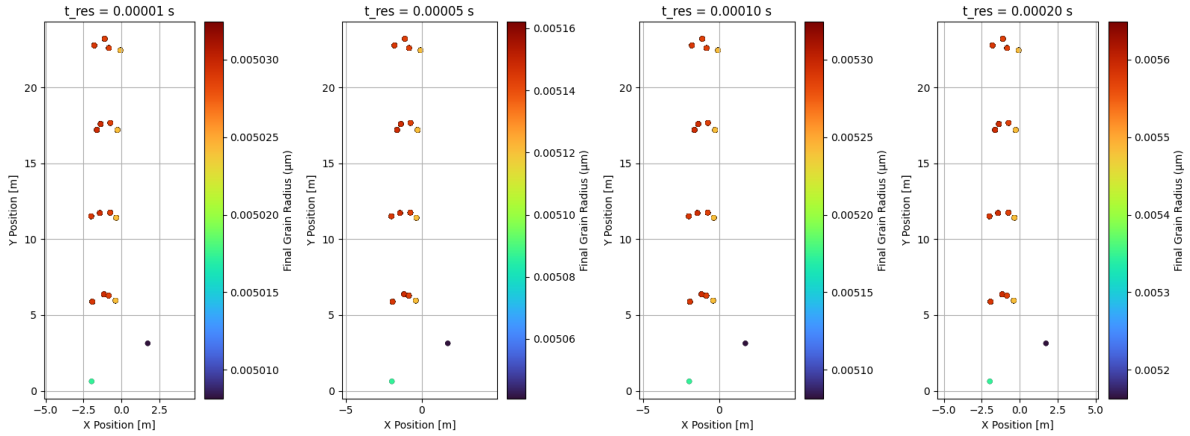

(a) t_{res} = 0.1x10^{-4} seconds **(b)** t_{res} = 0.5x10^{-4} seconds **(c)** t_{res} = 1x10^{-4} seconds **(d)** t_{res} = 2x10^{-4} seconds

Figure C.7: Growth of ice grain particles in Case 6 for q = 0.75 for different residence times

For q = 1.00

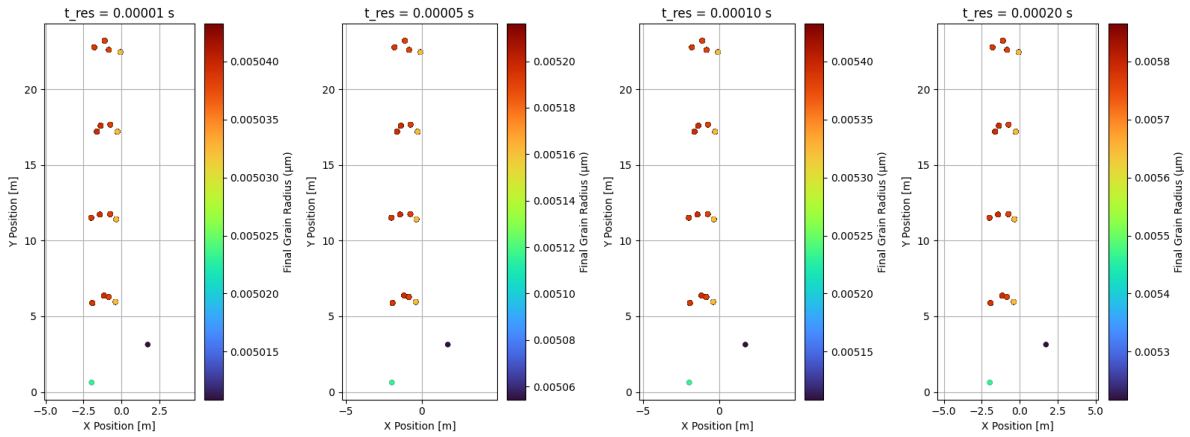

(a) t_{res} = 0.1x10^{-4} seconds **(b)** t_{res} = 0.5x10^{-4} seconds **(c)** t_{res} = 1x10^{-4} seconds **(d)** t_{res} = 2x10^{-4} seconds

Figure C.8: Growth of ice grain particles in Case 6 for q = 1.00 for different residence times